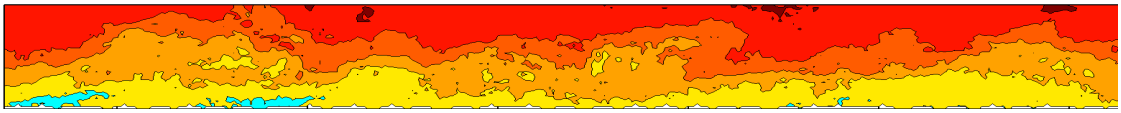

Turbulence structures affecting stone stability in backward-facing step flow

Experiments by means of Particle Image Velocimetry

Master of Science Thesis
November 2004
Author: Rohnen de Ruijter

Graduation committee:
Prof. dr. ir. J.A. Battjes
Drs. R. Booij
Ir. B. Hofland
Ir. H.J. Verhagen

TU Delft
Delft University of Technology

Faculty of Civil Engineering and Geosciences
Environmental Fluid Mechanics Section

Turbulence structures affecting stone stability in backward-facing step flow

Experiments by means of Particle Image Velocimetry

Faculty of Civil Engineering and Geosciences
Environmental Fluid Mechanics Section

Rohnen de Ruijter (9720115)
Delft, November 2004

With thanks to my parents

PREFACE

To complete my studies and to become a civil engineer, a Master of Science thesis had to be written. In my case this has resulted in this document, which is a report about the experiments I conducted in the Laboratory for Fluid Mechanics of the Faculty of Civil Engineering and Geosciences of Delft University of Technology and the accompanying analysis of the data obtained from these experiments.

Of the different possibilities (e.g. literature survey, numerical modelling, fieldwork), experiments in a laboratory appealed the most to me. The main reason to choose to conduct experiments was that it was most likely the last opportunity to do experiments myself. Also the combination of practical and theoretical aspects that came with the research contributed largely to this decision. The experiments were part of the research program "Stability of stones in the top layer of a granular filter" of Ph.D. candidate ir. B. Hofland.

I would like to express my thanks to ir. B. Hofland for being my advisor on more than a daily basis, for his confidence in a successful execution of the experiments, but most of all for his patience. Thanks are also due to the other members of my graduation committee for sharing part of their knowledge with me and for their useful remarks while writing this report. Finally, I would like to thank the staff members of the laboratory for their assistance while building the experimental set-up.

Delft, November 2004 Rohnen de Ruijter

ABSTRACT

Downstream of man-made hydraulic structures, bed protections made of granular material are often used to prevent erosion of the bottom. The stones in the top layer of such granular filters must be able to withstand the hydraulic forces. Probably the best-known formula that is used to determine the stability of granular bed material is the design criterion by Shields (1936). However, this criterion is only valid for uniform flows.

Little is known about the influence of turbulence on the stability of stones. In this thesis the influence of turbulence structures on the stability of stones in the top layer of a granular filter in one type of nonuniform flow that is often encountered near hydraulic structures, namely backward-facing step (BFS) flow, was investigated.

Flume experiments were conducted during which the flow field (streamwise, vertical plane) that caused movement of a stone in the reattachment region behind the step was recorded utilising Particle Image Velocimetry (PIV). To guarantee that stone movement occurred in the measuring area an artificial, naturally shaped stone with a low density was placed in the measuring area. This stone was attached to a hinge, so that after each movement (pivoting motion) it fell back to its original position and new recordings could be made. As low-mobility conditions were investigated, a sensor was used to detect the infrequent occurring movement of the stone. The signal from this sensor was used as a trigger to save the PIV recordings that were made before and after movement of the stone. Simultaneous to the PIV recordings, pressures were measured on stones surrounding the first stone.

Prior to the in-depth investigation of the flow around stone movement events, we divided the events in those during which the target stone made a real pivoting motion and those during which the stone merely rocked in its pocket. The conditionally averaged flow fields of both types of events (pivoting and rocking) were constructed. A classification procedure was used to get a first impression of the influence on the entrainment of stones of the so-called quasi-steady forces (QSF) and the turbulent wall pressures (TWP). To regard flow structures larger than the measuring area we created large-scale velocity maps by using a technique that is based on the Taylor hypothesis (frozen-turbulence approximation).

It turned out that the flow responsible for entrainment in the reattachment region can be classified as a Q1 event ($u'>0$, $v'>0$) or an outward interaction. This is in agreement with observations from other researchers. However, we found that the Q1 event is in fact a large-scale sweep (Q4 event: $u'>0$, $v'<0$) with a small-scale Q2 event ($u'<0$, $v'>0$) imbedded. The superposition of both flow structures results in the Q1 event.

The small-scale Q2 event is caused by a vortex that was present near the stone when it was entrained. This vortex originates from the shear layer that is always present in BFS flow and that divides the recirculation bubble behind the step from the high-momentum upper part of the flow. The bubble, in turn, is subject to a quasi-periodic enlargement-shrinkage cycle. It grows slowly in horizontal direction and subsequently retreats towards the step. We believe that entrainment in the reattachment region is related to this oscillation motion. When the bubble retreats it allows fluid with high longitudinal velocity from the upper part of the flow (the aforementioned sweep) to reach the bed. As this sweep advects vortices from the shear layer toward the bed, an ideal sequence of flow structures is established to dislodge a stone from its pocket: first a vortex lifts the stone slightly up, and subsequently the increased horizontal velocity together with the increased area of the stone that is exposed to this high momentum fluid, hauls the stone further away.

The pressure measurements showed that in addition to the contribution of quasi-steady drag and lift forces, the influence of turbulent wall pressures (which were shown to be mainly caused by the outer flow and not by the roughness of the bed) on the entrainment of stones in the reattachment zone, is significant.

From the results of identical experiments in uniform flow (Hofland & Booij, 2004), it is known that the same flow structures (large-scale sweep and small-scale vortices) were present at the time of stone entrainment. The origin of the structures, however, is completely different. In uniform flow the flow structures are related to wall turbulence (e.g. hairpin vortices), while in BFS flow the influence of the shear layer and the oscillation of the reattachment length is significant.

TABLE OF CONTENTS

1 INTRODUCTION

1.1 Background

Downstream of man-made hydraulic structures, bed protections made of granular material are often used to prevent erosion of the bottom and to avoid the development of scour holes in the vicinity of the construction. The stability of a hydraulic structure as a whole can be effectuated in this way. From this, the importance of the need of a well-functioning bed protection is directly clear: failure of the bed protection may lead to the collapse of the entire hydraulic structure.

The stones in the top layer of a granular filter, used as a bed protection, must be able to withstand the hydraulic forces, in other words: they have to remain in place. Whether they really do depends on the amount of attack on the bed and the resistance of the stones against it.

What does determine the hydraulic load on a bed protection? Obviously, high velocities of the water (e.g. resulting from a large water level difference over the hydraulic structure) are very important, but also turbulence plays a crucial role. It is for instance well-known that downstream of a separation point, in the proximity of the point where the flow reattaches to the bottom, the bed damage can be large while the mean longitudinal flow velocity can be low or even zero. This large damage (or only large attack if the bed protection is designed well) is attributed to the relatively high turbulence level around the reattachment point. An example of a hydraulic structure with a relatively high velocity and an increased turbulence level downstream of it, are the weirs of Figure 1.1.

FIGURE 1.1 *The weirs of the sluice and weir complex near Driel in the river Nederrijn (The Netherlands) are examples of a hydraulic structure with a considerably increased turbulence level downstream of it and hence an increased flow attack on the bottom in this region.*

Furthermore, some recent research indicates that the influence of fluid accelerations on the entrainment of stones from bed protections may be larger than was assumed at first. These accelerations can be caused by constrictions of the main flow by hydraulic structures, but locally they can also be induced by turbulence. Besides the accelerations it is assumed that turbulence influences the entrainment of stones in (many) other ways, however it is not exactly known in which manner. The determination of the influence of turbulence on the entrainment of stones from bed protections is the objective of the Ph.D.-study of which this present study is part. The Ph.D.-research is restricted to stationary (time-independent) flows, but does include nonuniform (variations in space) situations.

Such flows can exist for a certain period of time downstream of hydraulic structures. Often the nonuniformity then results from a sudden increase of the depth caused by an abrupt ending of a construction of some kind on the bottom of a watercourse. This vertical expansion in the flow direction is often referred to as a **backward-facing step** (**BFS**). BFS flow occurs near plenty of hydraulic structures (e.g. discharge sluices, weirs, culverts etc). The influence of turbulence on the stability of stones downstream of a BFS is the subject of this present MSc-thesis. The emphasis is on the influence of the turbulence structures, also known as coherent structures (CS), that occur in flows downstream of a BFS. The choice to investigate stone stability downstream of a BFS was also influenced by the fact that BFS flow has been subject of investigation for decades and that therefore there is quite some knowledge about this type of flow available.

On the other hand there is the question: Which factors determine the strength of a bed protection? Unmistakably, the weight of the stones is the main force that keeps the stones in place, but friction and contact forces between adjacent stones can act as resisting forces as well. So besides the size of the stones (weight) there are other aspects like the shape of the stones and the grading that are of importance. A lot of researchers investigated the stability of coarse bed material in flows. Probably the best-known formula that resulted from this and that is still commonly used, is the design criterion by Shields (1936) for stones in uniform flows. Although some knowledge about the factors that determine the strength of a granular bed and some insight in the existing design criteria are required, we shall mainly look at the dislodging of stones from a granular bed from a fluid mechanics point of view.

1.2 Problem description

The flow near almost every hydraulic structure is not uniform. The rapid changes in turbulence intensities in nonuniform flows make the design of the top-layer of a granular bed protection for such flows a rather complicated matter.

For relatively small structures and preliminary designs a formula for uniform flows, like the one given by Shields, is used with a correction for the increased turbulence level. In these design approaches the exact place where the flow attack occurs, or where the flow attack is larger than average, is oftentimes not specified, resulting in a large area of bed protection with the maximum stone diameter. Moreover, since the exact way in which turbulence influences stone stability is not known, the maximum stone diameter is perhaps not only used in too large an area, but even the diameter itself might be larger than necessary; or worst it might be too small. Insight in the phenomena that affect the incipient motion of stones may lead to design methods that yield cheaper bed protections.

For large hydraulic structures the design of the bed protection is (still) done by means of scale models. In the future it might be possible to design bed protections with the help of sophisticated computational models in which the turbulent velocities at each location in the flow can be calculated. To utilise such models, first it has to be known in detail how turbulence can lead to bed damage.

Instead of looking at the stability of a bed protection as a whole, the stability of each individual stone can be considered as well. A bed protection after all consists of loose stones, each one of which can start moving in one way or another. Also in this area a lot of research

has been carried out, varying from elementary test like determining drag and lift forces on a sphere in an infinite uniform flow, to studies in which the hydraulic forces on a stone in a bed consisting of coarse bed material was measured.

In general, heavier stones can withstand larger hydraulic forces than lighter ones. However, even in a bed consisting of stones with a narrow gradation and an, on average, equally distributed load, not all stones move simultaneously. Aspects like protrusion, exposure, orientation, shape, etc. of each single stone are crucial for its stability. For instance, a stone that is oriented in a way that a large area of the stone is exposed (large surface area perpendicular to the mean flow direction) will obviously experience larger forces than a stone that has its longest axis parallel to the mean flow direction. However, these aspects become less relevant once a bed has been exposed to a flow before. The stones protruding most have been washed away and have found a new, more shielded position in the bed; others have rotated until their most streamlined cross-section is in line with the flow. In general the stones have attained more stable positions. One refers to such a bed as a "water-worked" bed. Still, when a water-worked bed is exposed to a load again and the hydraulic forces increase, there will be a point at which some stones start to move. The cause of this must be searched within the load, i.e. the flow field around a stone at the moment it starts to move. Local movements of the water in the vicinity of a stone are important, but somewhat larger-scale turbulence structures may be of significance as well. But what exactly are the effects of local accelerations, coherent structures and turbulent velocity fluctuations on the initial movement of a stone? What are the influences of the changes in the turbulent structures as they occur downstream of a backward-facing step? In what way does the flow field around a stone positioned downstream of a BFS, differ from that in uniform flow? This is discussed in this report.

1.3 Objective

For the design of bed protections it is useful to gain insight in the relation between the type of flow considered here and the stability of stones in a bed protection and to arrive at a more fundamental, less empirical design criterion that is based on physical phenomena. However, this is too large a goal for this thesis. This research is restricted to

the determination of the influence of turbulence structures on the stability of stones in the top layer of a granular filter downstream of a backward-facing step.

The fulfilment of this goal is a small contribution to arrive at a more reliable and hopefully a more cost-effective way of designing bed protections in nonuniform flows.

1.4 Approach

To determine the influence of turbulence structures on the stability of stones downstream of a BFS, first the flow structures occurring near a stone that begins to move must be known or at least they must be made visible in one way or another. It would be convenient to simultaneously know some pressures on the stone that is about to move as well, as the occurring pressures lead to forces that cause movement. Subsequently it can be tried to find correlations between the structures and the pressures or search for conditions that have to be fulfilled (e.g. the presence of a certain kind of flow structure, or a peak in the longitudinal velocity) in order to dislodge a stone from its original position.

The most convenient way to determine these turbulence structures and pressures was to conduct experiments in a laboratory. For the abovementioned Ph.D.-study, a test facility had been built in the Laboratory for Fluid Mechanics of the Faculty of Civil Engineering and Geosciences of Delft University of Technology. We used this flume to conduct experiments.

Since we needed to be able to distinguish coherent structures (CS) in the flow, instantaneous velocities needed to be known over a relatively large (compared to most measurements techniques) area. To this end a relatively new technique called digital particle image velocimetry (PIV) was used. Instantaneous, two-dimensional (2-D) velocity fields of rather high spatial and, to a lesser extent, temporal resolution of a relatively large area could be obtained with the help of the PIV system we used. The main difference of this research compared to previous ones that deal with stability of stones is that the PIV technique enabled us to capture complete, instantaneous, 2-D flow fields, including CS, instead of time averaged flow fields or time-varying velocities in a fixed point as was usual in the past.

Still the question remained: how to capture flow fields and pressures around a stone that was about to move? One does not known beforehand where and when a stone in a bed starts to move and the measuring area covered only a small part of the flume (see Chapter 3). However, there had to be a stone, that was about to move, within the limits of the measuring area. Since we are interested in the cause of entrainment during (very) low-mobility transport of bed material, stone movements were rare and the chance of a moving stone within the measuring area was low. Conversely we needed several stone movements and their accompanying velocity fields in order to draw reliable conclusions. The low-mobility condition however implied that an increase of the flow attack to get more stone movements was out of the question. Moreover, the frequent moving of stones during a larger transport rate would have influenced the water motion.

To overcome these difficulties, we came up with some contrivances. An artificial stone, copied from a real stone from the granular bed that was used during the experiments, was placed in the measuring area. Since this so-called “target stone” was much lighter than the real ones, it was the first stone to move. Some other artificial stones that were glued to the bottom, surrounded the target stone and were equipped with built-in pressure transducers. Moreover, from the signal of a sensor that was positioned underneath the target stone and that indicated when this stone had moved, the interesting parts of the continuously measured pressure time series and velocity time series were known. Hence, the experimental set-up enabled us to measure velocity fields and pressures around a stone simultaneously and let us know when this stone had moved.

1.5 Demarcation of the research

The extent of the experiments obviously was restricted to the capacity of the test-facility and the availability of materials and measuring devices in the laboratory. Additionally we constrained the research to some specific conditions ourselves. Furthermore, since there was only a limited amount of time available for this research we tried to avoid a too extensive measuring program and tried to limit the analysis of the data obtained. These constraints are discussed in the following. Some of the symbols and terms that are used have not yet been introduced; they are explained in Chapter 2 and 3.

Restrictions

There were dozens of restrictions that had to be taken into account before and during the execution of the experiments, but only the most important and nontrivial ones are given here.

- Experiments had to be conducted in the aforementioned flume with accompanying flow control devices (see also §3.2).
- Working fluid: water. Changing the viscosity by controlling the temperature of the water to obtain different values of the Reynolds number was not an option.
- Measuring method: PIV double frame-single exposure method.
- The PIV measurements were restricted to 2-D measurements in the centre line of the flume.
- Stones for the granular bed had to be chosen from the ones stored in the laboratory.

Experimental conditions
The experimental conditions are self-imposed limitations that mainly resulted from trying to obtain conditions similar to conditions occurring in practice.

- $\mathrm{Re} = \frac{uh}{\nu} > 3000$ for sufficient development of turbulence in the flume.
- $\mathrm{Re} = \frac{u_* d}{\nu} > 200$ condition for the turbulence around the stones required for an influence of the friction between the fluid and the stones that resembles the influence present in practice.
- $\mathrm{Re}' = \frac{ud}{\nu} > 2500$ so drag and lift forces follow the well-known law for steady drag and lift force .
- Free water surface (no use of a rigid lid).
- $H / h \cong 0.345$ (step height / water depth), to make comparison with previous experiments possible.
- Froude numbers as low as possible to avoid influences of water surface gradients or waves on stone stability.
- $b / h > 3$ (width of flume / water depth) to minimise wall-effects.
- $h / d_{n50} > 5$ (water depth / average stone diameter).
- Hydraulic rough bottom.
- Flat bottom (no dunes or ripples).
- Low hydraulic forces; the aim of the research is to discover the cause of initial motion of stones.
- Use of only coarse, non-cohesive bed material that resembled the material that is generally used in bed protections could be used.
- Narrow grading of stones ($d_{n85} / d_{n15} \leq 1.5$).

Focus
In this thesis the emphasis is on the hydraulic forces caused by a flow (the load), rather than on aspects that determine the strength of a granular bed protection. The investigation of the fluid motions that cause entrainment of stones from a bed protection downstream of a BFS prevail above the aspects that determine the strength of a granular bed protection.

In spite of many researches (e.g. De Gunst, 1999) a lot more knowledge about the intensity of the flow attack as a function of the distance downstream of a BFS is required to arrive at a reliable design criterion for filters downstream of a BFS. The same is true for the influence of aspects like protrusion and exposure on the entrainment of stones. Nevertheless, we only briefly go into these aspects and focus on the area with the largest flow attack.

The emphasis clearly is on the analysis of the PIV measurements. The examination of the PIV measurements also outweighs the investigation of the measured pressures; mainly since time limitations did not allow investigating both the influence of turbulence structures on entrainment as well as all the other mentioned aspects, in depth. What is included in the present research is an overview of the time mean flow field at different distances downstream of a BFS. Furthermore, the causes of entrainment of stones in the reattachment region of BFS flow and that of stones in uniform flow are compared. The uniform flow experiments were previously analysed by Hofland & Booij (2004).

1.6 Structure of the report

The following chapter gives an up-to-date overview of the knowledge of BFS flow, the stability of coarse bed material in this type of flow, some relevant definitions used in turbulence theory and an explanation of the principles of the PIV technique. In the Chapter 3 a

detailed description is presented of the experimental set-up and the measuring appliances, including the accuracy of measurement of the different devices, are presented. Moreover this chapter contains an overview of the experiments conducted and the accompanying flow conditions. The methods and operations that were used to convert the raw data to a useful and orderly whole are given in Chapter 4. The results of the experiments are divided in two chapters. In Chapter 5 the mean flow and turbulence characteristics are presented and compared to experiments conducted by other researchers. Chapter 6 deals with the turbulence structures responsible for damage to bed protections (moving of the target stone) in the reattachment region. In this chapter the results of the experiments are compared to the results of tests conducted during uniform flow conditions as well. In Chapter 7, the last chapter, the conclusions that can be deduced from the data analysis are summarised. Besides, restrictions of the validity of the conclusions are presented and recommendations for further research in the form of experiments or additional data analysis are given. Finally, in the appendices of this report one can find, among other things, technical specifications of the measurement apparatus, characteristics of the stones used and the values of parameters used to calculate velocity vectors from the raw data.

Some large chapters end with a short summary or conclusion in order to keep the overview or to indicate at which stage of the fulfilment of the objective the research has arrived and to summarise what still has to be done.

2 THEORY

2.1 Introduction

In this chapter some background information on the topics associated with this research is presented. It consists mainly of an overview of some definitions and symbols used in turbulence theory used in the present research, the present knowledge of BFS flow, some conclusions of literature that deals with entrainment (stability) of particles in flow in general and in BFS flow specifically, a short introduction to the PIV measurement technique and some remarks about how to interpret PIV results.

Although a lot of research has been done in the fields of both BFS flow and stability of stones/sediment in flows, the combination of the two is a less explored area of interest. Only a few authors provide some information: De Gunst (1999); Xingkui & Fontijn (1993); Schiereck (2001, after DHL, 1985); Nelson *et al*. (1995) and Hofland *et al*. (subm.c). All of them conducted experiments and all of them emphasised different aspects (see later on in this chapter) of the combination of BFS flow and bed attack (or bed mobility). However, as far as we know, no literature is available that gives detailed information on the turbulence structure(s) in BFS flow that initiate(s) stone movement. Still this research may benefit from the results of the aforementioned works.

Several authors investigated the influence of BFS flow on the distributions of quantities like pressure, bottom shear stress, Reynolds stresses etc., on the bottom wall downstream of a BFS, without directly linking the results to stone stability. These quantities however, may be connected to initial motion of particles and therefore seem relevant for this research. Of these researches, the ones that involve pressure distributions (Lee & Sung, 2002; Hofland *et al*., subm.c) may be of the most use, as pressures can be directly linked to net forces and hence to movement.

More and more is known about BFS flow. No longer only statistics derived from point-measurements are available and 2-dimensional (2-D) phenomena are known, but rather detailed insight in the 3-dimensional (3-D) structure of this type of flow and the occurring mechanisms is available, both qualitatively (from flow visualisation techniques) as well as quantitatively (from computations and measurements). Several authors have conducted PIV measurements of a BFS flow (e.g. Scarano *et al*., 1999; Kostas *et al*., 2002). Most of the time the 2-D measurements took place in a vertical plane in the streamwise direction, but sometimes in a vertical plane in the spanwise direction as well (we did not encounter a 3D, stereoscopic, holographic PIV measurement so far), but it seems that none of the experiments was conducted with a rough bottom wall downstream of the BFS. Obviously, the combination of PIV measurements with a signal that indicates entrainment of stones, which provides an exquisite trigger for conditional averaging, is completely new.

It was tried to include the most up-to-date knowledge in all the mentioned fields of interest. The chapter ends with a summary in which the most important aspects and conclusions of this chapter are repeated.

2.2 Turbulence

The understanding and especially the prediction of the turbulent motion of fluids (water) are two of the most difficult aspects of modern fluid mechanics. A lot of research is going on nowadays, varying from experiments to Direct Numerical Simulations (DNS). Of course for this research only a few aspects of turbulence theory are important. Some basic definitions, which are inextricably associated with turbulence, are treated first. In this way the notation used in this report is defined. Next, the characteristic well-known flow phenomena associated

with backward-facing step flow are presented briefly. Finally, 3-D aspects, including coherent structures that occur in this type of flow, are clarified.

2.2.1 Definitions and notation

In this report the velocity components in the horizontal direction (*x*-direction) and the vertical direction (*y*-direction) are denoted by *u* and *v* respectively (see Figure 2.1).

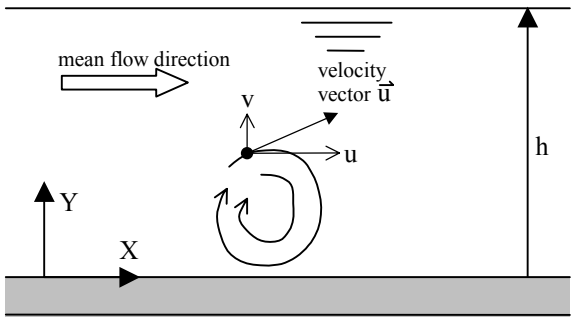

FIGURE 2.1 *Co-ordinate system and velocity components*

The velocity in the lateral direction (*z*-direction) is denoted by *w*. The positive *x*-, *y*- and *z*-directions are respectively from left to right, bottom up and in the plain of paper. The corresponding velocities *u*, *v* and *w* are positive if directed in the positive co-ordinate directions. In all the flow-related figures that are produced in this report, the mean flow direction is from left to right. For water depths the symbol *h* is used throughout this report. Time averaging is denoted with an overbar, e.g. $\bar{u}$. Brackets denote spatial averaging: $\langle u \rangle_x$. The subscript (*x*) represents the area over which the averaging takes place. A capital *U* always denotes a single, time mean and spatially averaged value for the horizontal velocity. Often this is the bulk velocity of a vector field (i.e. the bulk velocity in the measuring area, see Chapter 3). Sometimes it denotes the mean horizontal velocity of a cross-section of the flow.

Though well known, the definition of the Reynolds number is, for completeness sake, presented here too:

$$\mathrm{Re} = \frac{UL}{\nu} \tag{2.1}$$

In this expression ν denotes the kinematic viscosity of the fluid, which is temperature dependent and can be found in appendix A in the case the fluid is water. *L* represents a characteristic length over which a velocity difference *U* exists. Since the Reynolds number is the ratio of the destabilising and stabilising forces of a disturbance in a flow, high Reynolds numbers ($Re > 1000 - 2000$) correspond with chaotic (i.e. turbulent) flow. In BFS flow the step height, denoted by a capital *H*, is often chosen as the characteristic length and for the velocity the (free-stream) velocity upstream of the trailing edge is generally chosen.

Reynolds decomposition

As we are interested in the turbulent fluctuations of velocities, because of their influence on the entrainment of stones, it is useful to separate them from the mean motion. This procedure, known as Reynolds decomposition, is given here for the horizontal flow velocity only and reads:

$$u' = u - \bar{u} \tag{2.2}$$

in which u' is the fluctuating part of the velocity and u the instantaneous velocity.

Substituting the Reynolds decomposed velocities in the Navier-Stokes equation and ensemble averaging this equation yields the so-called Reynolds equation. The averaging of the non-linear terms in the Navier-Stokes equation results in terms known as the Reynolds-stresses. The

$$-\rho_w \overline{u'v'} \tag{2.3}$$

term of these stresses is of the most importance for this research, for they can be interpreted as turbulent shear stresses. The parameter ρ_w denotes the density of the water (in this report the fluid is always water).

Coherent Structures

As we shall use the term "coherent structures" frequently in this report, we need to clarify what coherent structures (CS) are. While the existence of coherent structures is clear from visual observations, their mathematical description is far from trivial. Several instantaneous physical quantities have been proposed and used to describe coherent structure, all yielding different answers. Therefore we restrict ourselves to a qualitative definition, namely: coherent structures are the similar, reproducible flow patterns that can be observed repeatedly in a turbulent flow.

They are present in nearly all turbulent flows. Often they are relatively large with respect to the total range of turbulence scales or they exist in a hierarchy of structures. In a 2-D observation plane they often tend to emerge as spiral patterns.

2.2.2 Statistics

For brevity, the formulae in this section are given for the x-direction only. They can easily be expanded into three dimensions in a way that is analogous to that for the x-direction.

In case the flow is stationary, as is the case during the current experiments, the time average velocity equals the ensemble-averaged value if the averaging period is long with respect to the characteristic time scale of the turbulent motions and is given by the following formula:

$$\overline{u} = \frac{1}{N}\sum_{n=1}^{N} u_n \tag{2.4}$$

In this formula N denotes the total number of realisations and u_n denotes the n^{th} realisation.

The intensities of the velocity fluctuations cannot directly be obtained from the averages of the fluctuations, since these are zero by definition. However, by its nature the fluctuating component of a property is characterised by its variance. For velocities the variance is a measure of the kinetic energy present in the turbulent fluctuations. The square root of the variance, called the standard deviation, yields the intensities of the velocity fluctuations:

$$\sigma_u \equiv \sqrt{\overline{u'^2}} \equiv \sigma_{u'} \tag{2.5}$$

Since $u - \overline{u} = u'$ and $\overline{u'} = 0$ by definition, the standard deviation of u is the same as the standard deviation of u' (= the root-mean-square value of u'). The following formula, that gives the same result as Eq. (2.5), was used in this research to calculate the intensities:

$$\sigma_u = \sqrt{\frac{1}{N}\sum_{n=1}^{N}(u_n - \overline{u})^2} \tag{2.6}$$

Again N denotes the total number of realisations and u_n a single realisation.

Higher order statistics can be useful to determine in what respect the turbulent fluctuations deviate from a Gaussian distribution. Close to a wall and in other regions with strong velocity gradients (downstream of a BFS) the skewness in the distribution of the velocity fluctuations can be significant.

Probability density distribution of $u|u|$

Since the drag force on an object is proportional to $u|u|$, it is important to know some characteristics of this quantity. If it is assumed that the near-bed velocity u_b defined somewhere in the vicinity of the object on a bottom wall is normally distributed, then the following distributions of $u_b|u_b|$ for different turbulence intensities are the result (Hofland, subm.b):

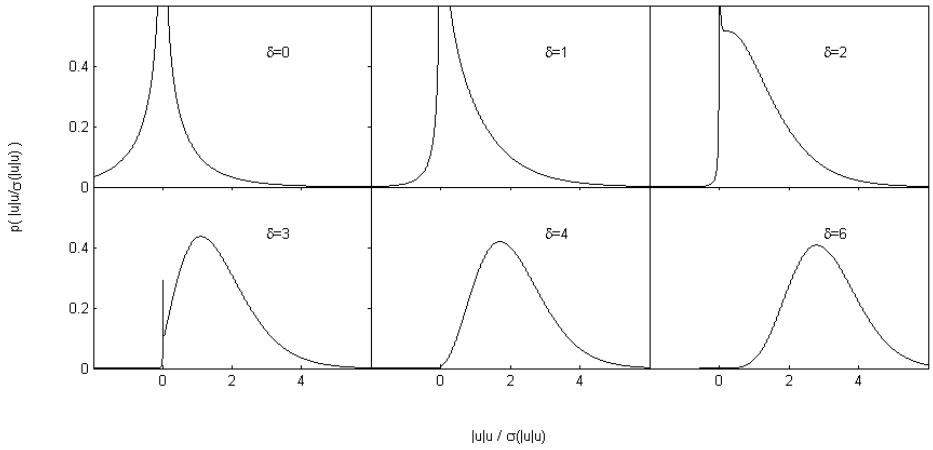

FIGURE 2.2 *Plot of $p(|u_b|u_b / \sigma(|u_b|u_b))$ as a function of $|u_b|u_b$ normalised by its standard deviation for different values of the non-centrality parameter δ.*

The non-centrality parameter δ in these graphs is defined as:

$$\delta = \frac{\overline{u}_b}{\sigma(u_b)} \tag{2.7}$$

and is small when the standard deviation of u_b is large with respect to the mean value of this velocity, thus indicating a relatively high near-bed turbulence intensity. As a matter of fact, the reciprocal value of the non-centrality parameter δ is the relative turbulence intensity r:

$$r = \frac{\sigma(u_b)}{\overline{u}} = \frac{1}{\delta} \tag{2.8}$$

Even if the assumption of a normally distributed near-bed u-velocity may not quite reflect reality, the influence of the deviation from the bell-shaped Gaussian distribution on the shape of the $u|u|$ distribution is often negligible, at least in uniform flows. The shape of the last-

mentioned distribution is highly influenced by the value of δ, as becomes clear from Figure 2.2. As the relative turbulence intensity drops in the streamwise direction downstream of the reattachment zone of a BFS, a larger value of δ may be interpreted as a larger distance downstream of the reattachment zone in a BFS flow. In case of high turbulence intensity (δ = 0, $r = \infty$), which is the case near the reattachment zone of a BFS flow, a distribution as shown in the upper left-hand corner of Figure 2.2 is the result. For the expressions that describe the distribution of $u_b|u_b|$, its mean and its standard deviation we refer to Hofland (subm.b).

Often the drag and lift force on a stone are estimated to be proportional to u^2, instead of $u|u|$, which yields the same magnitude of the force, but the wrong sign in cases of a negative u-velocity. When the quantity u^2 (or $u|u|$) is averaged in time, the rules for calculating with average and fluctuating parts of the velocity have to be satisfied, demonstrated here for u^2 only:

$$\overline{u^2} = \overline{\left(\overline{u} + u'\right)^2} = \overline{\overline{u}^2 + 2\overline{u}u' + u'^2} = \overline{u}^2 + \overline{u'^2} = \overline{u}^2 + \sigma_u^2 \tag{2.9}$$

The last term on the right-hand side of Eq. (2.9) is significant in highly turbulent flows like BFS flow. Determining the time averaged u-velocity of a set of samples first and use this value to calculate the mean drag and lift forces gives another result than using Eq. (2.9), because by definition the time averaged u-velocity has no fluctuating component.

2.2.3 Swirling strength

Several authors have proposed methods of extracting structure from velocity fields. These methods involve critical-point analysis of the local velocity gradient tensor ($\nabla\vec{u}$, $\vec{u}$ = (u, v, w) = total velocity) and its corresponding eigenvalues or the Hessian of pressure (Jeong & Hussain, 1995). The main results of these methods are summarised by Adrian *et al*. (2000a). The studies show that the imaginary part of the complex eigenvalues of the velocity gradient tensor, denoted by λ_{ci}, is a useful indicator to localise vortices in 2-D planes in 3-D flows. If the flow is a pure shear flow, particles would orbit infinitely-long ellipses and the orbit period (represented by $(\lambda_{ci})^{-1}$) would be infinite, corresponding to λ_{ci} = 0. Shorter, more circular ellipses (vortices) correspond to $\lambda_{ci} > 0$. The strength of any local swirling motion is quantified by the value of λ_{ci}.

However, since our PIV fields are two-dimensional the full local velocity gradient tensor can not be formed and therefore we used an equivalent two-dimensional form as proposed by Adrian *et al*. (2000a):

$$A^{2-D} = \begin{bmatrix} \dfrac{\partial u}{\partial x} & \dfrac{\partial u}{\partial y} \\ \dfrac{\partial v}{\partial x} & \dfrac{\partial v}{\partial y} \end{bmatrix} \tag{2.10}$$

This matrix has two distinct real eigenvalues if the discriminant of its characteristic equation is positive, two complex conjugate eigenvalues ($\lambda_{cr} \pm i\lambda_{ci}$) if the discriminant is negative and one real eigenvalue if the discriminant equals zero. The characteristic equation of $A^{2\text{-}D}$ reads:

$$\lambda^2 + \lambda\left(-\frac{\partial u}{\partial x} - \frac{\partial v}{\partial y}\right) + \frac{\partial u}{\partial x}\frac{\partial v}{\partial y} - \frac{\partial u}{\partial y}\frac{\partial v}{\partial x} = 0 \tag{2.11}$$

This is a 2nd degree equation of which the roots (= the eigenvalues of $A^{2\text{-}D}$) can be found by use of the quadratic formula. The discriminant D of Eq. (2.11) is:

$$D = \left(\frac{\partial u}{\partial x}\right)^2 + \left(\frac{\partial v}{\partial y}\right)^2 - 2\left(\frac{\partial u}{\partial x}\frac{\partial v}{\partial y}\right) + 4\left(\frac{\partial u}{\partial y}\frac{\partial v}{\partial x}\right) \tag{2.12}$$

If the discriminant D is negative ($D < 0$), complex eigenvalues exist. As stated before, only the imaginary portion of the complex eigenvalues is relevant when trying to pinpoint vortices. If $D < 0$ then this part is defined by $\lambda_{ci} = (-1/4D)^{0.5}$ and is always positive. In the other cases ($D > 0$, $D = 0$) there are no complex eigenvalues and consequently $\lambda_{ci} = 0$.

In literature, similar expressions as the one for λ_{ci} are used to distil vortices from flow fields, but often without the square root. Also Adrian *et al.* (2000a) do not give the resulting expression for λ_{ci}, they only present the way to derive it. Neither do they give any values or dimensions from which the final expression of λ_{ci} may be deduced; they merely show that their expression for λ_{ci} (with or without the square root) can be used as a qualitative indicator of vortex locations. We chose to use $(\lambda_{ci})^2$ to quantify the strength of a swirling motion and implemented all the above by using the following expression:

$$\lambda_{ci}^2 = \max(-\frac{1}{4}D, 0) \tag{2.13}$$

So $(\lambda_{ci})^2$ has a positive value if $D < 0$ and otherwise $(\lambda_{ci})^2$ is zero. The software used in the experiments (DaVis 6.2), also uses Eq. (2.13), but they call $(\lambda_{ci})^2$ the local swirling strength. A second reason to use $(\lambda_{ci})^2$ is that it distinguishes strong swirling motions better than λ_{ci} would. An additional advantage of using the expression of the squared swirling strength is that it has the same units (s^{-2}) as the Weiss function Q, which is defined as the second invariant of the local velocity gradient tensor and is also often encountered in literature dealing with coherent structures in turbulent flows. In 2-D flow the Weiss function reduces to:

$$Q = -\frac{1}{2}\left(\frac{\partial u}{\partial x}\right)^2 - \frac{\partial u}{\partial y}\frac{\partial v}{\partial x} - \frac{1}{2}\left(\frac{\partial v}{\partial y}\right)^2 \tag{2.14}$$

Although $(\lambda_{ci})^2$ and Q are not completely similar, they both contain the term $(\partial u/\partial y)(\partial v/\partial x)$ which is dominant in 2-D vortical flows (Scarano, 2000). Besides, if in a 2-D flow incompressibility of the flow is assumed ($\partial u/\partial x = -\partial v/\partial y$), both Q as well as $(\lambda_{ci})^2$ reduce to:

$$Q = \lambda_{ci}^2 = -\left(\frac{\partial u}{\partial x}\right)^2 - \frac{\partial u}{\partial y}\frac{\partial v}{\partial x} \tag{2.15}$$

Even if it is not very realistic to assume incompressibility of the flow for a 2-D measurement in a highly turbulent 3-D flow as BFS flow, it does serve to gain insight on the effect of a high local swirling strength on the occurring pressures. Since the Weiss function is directly linked to the distribution of pressure (p) in the flow field via the Poisson equation for pressure:

$$\nabla^2 p = 2\rho Q \tag{2.16}$$

the pressure dip caused by a vortex can be estimated. This underpressure may be an important factor in the entrainment of stones from a granular bed protection.

Physically Q can be interpreted as a combination of the local shear strain rate and local vorticity magnitude. An analogous physical interpretation of $(\lambda_{ci})^2$ is less evident, although it is clear that $(\lambda_{ci})^2$ also is a linear combination of the squares of the vorticity around the z-axis (ω_z, positive in counter-clockwise direction), the shear strain rate in the x-y-plane (γ_s) and the linear strain rate in the x-y-plane (γ_l), which are defined respectively by $\omega_z = \partial v/\partial x - \partial u/\partial y$, $\gamma_s = \partial v/\partial x + \partial u/\partial y$, $\gamma_l = \partial u/\partial x + \partial v/\partial y$. As a matter of fact: $4(\lambda_{ci})^2 = (\omega_z)^2 - (\gamma_s)^2 - (\partial u/\partial x - \partial v/\partial y)^2$.

2.3 Backward-facing step flow

The choice to study the cause of entrainment of stones behind a BFS originates from the fact that the flow in the vicinity of various hydraulic structures often resembles a BFS flow. Besides, BFS flow is a well-defined flow that has been subject of investigation of many foregoing experiments. Since it is a flow with relatively large turbulence intensities in comparison with uniform flow it allows us to investigate the influence of turbulence on the stability of coarse bed material. By comparing BFS flow with uniform flow it can be examined which turbulence structures cause the increased attack on the bed downstream of a BFS.

Turbulence is caused by a velocity gradient perpendicular to the main flow direction and depending on the cause of this velocity gradient, two types of turbulence can be distinguished: free turbulence and wall turbulence. Both types are encountered in a BFS flow. The free turbulence occurs directly downstream of the step and is caused by the fact that a mass of water with relative high velocity is forced to move along a mass of water with a relative low velocity (the water in the recirculation zone). The wall turbulence obviously occurs in the vicinity of the bottom wall.

2.3.1 Two-dimensional mean flow structure

Although the backward-facing step flow is the simplest reattaching flow, the flow field is still very complex. The main two-dimensional flow characteristics of a BFS flow are illustrated in Figure 2.3. The co-ordinate system has its origin in the step corner (i.e. the corner formed by the step and the bed) and the indices *1* and *2* refer to upstream and downstream of the step respectively. The index *0* refers to the free-stream velocity, which in cases were there is no free-stream velocity, because the boundary layer reaches to the water surface, is represented by the velocity near the water surface upstream of the step edge.

The upstream boundary layer detaches at the sharp corner and a mixing layer with intense shear stresses (free-shear layer) starts to develop between the fast flowing upper part of the flow and the low-momentum lower part of the flow. A recirculating flow, with negative horizontal velocities near the bottom, exists between the step and the reattachment point. A secondary recirculation region occurs at the step corner. The mean reattachment point occurs where the streamline originating at the step edge impinges on the bottom wall. The length from the step to this point is called the mean reattachment length and is denoted by X_R.

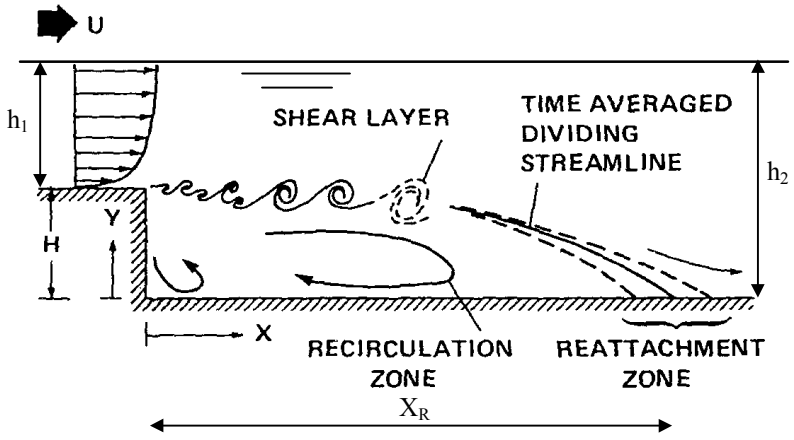

FIGURE 2.3 *Side view of a backward-facing step and its characteristic flow structure (Simpson, 1989).*

The shear layer deviates in the direction of the low-velocity zone slowly through the first half of the separated-flow region (Simpson, 1989) and appears to be much like an ordinary plane mixing layer. The dividing mean flow streamline is only slightly curved and the shear layer is thin enough that it is not affected by the presence of the wall (at least in our present configuration). However, the reattaching shear layer differs from the plane-mixing layer in one important aspect: the flow on the low-speed side of the shear layer is highly turbulent. The separated shear layer curves sharply downward in the reattachment zone and impinges on the wall (in theory the long-time-averaged streamline has to be perpendicular to the bottom wall, since the mean horizontal velocity is zero). Part of the shear-layer fluid is deflected upstream into the recirculating flow by a strong adverse pressure gradient. The maximum backflow velocity is usually over 20% of the free-stream velocity.

According to Simpson (1989) the mean reattachment length for turbulent flows with step height Reynolds numbers Re_H (based on the upstream free-stream velocity U_0 and the step height H) above 10^4, is mainly a function of the expansion ratio (h_2 / h_1). Nakagawa & Nezu (1987) compared some results from different authors with their own open-channel data and found that the mean reattachment length reaches a minimum value of about 5 step heights for large Reynolds numbers ($Re > 2 \cdot 10^4$, based on downstream bulk velocity and flow depth), they did not mention the accompanying expansion ratios. They also suggested that the influence of the Froude number Fr on the reattachment length may be significant, since the free water surface variations become larger with increasing Fr. Both De Gunst (1999) and Nakagawa & Nezu found mean reattachment lengths of about 6 à 7 step heights. Both conducted experiments with a ratio H / h_2 (= step height / downstream water depth) of 0.345, which implies $h_2 / h_1 = 1.53$ if it assumed that $h_1 = h_2 - H$ (horizontal water surface). De Gunst used a rigid lid, and the bottom wall downstream of the step consisted of granular material, while Nakagawa & Nezu conducted experiments with a free water surface and a smooth wall. In most of the other literature similar values for the mean reattachment length were found, but none of the consulted sources was based on an experiment with a rough wall downstream of the BFS together with a free water surface as in the present case. DNS and Large Eddy Simulation (LES) in general underestimate the reattachment length.

Downstream of the reattachment zone a new boundary layer starts to develop. Yet, the relaxation of the mean streamwise profiles towards an equilibrium turbulent boundary layer is slow. The influence of the step ranges as far as ca. 50 step heights downstream of the step. This is probably caused by the fact that large-scale structures are still present far downstream of the step (see section on three-dimensional instantaneous flow phenomena). The large deviation of the vertical distributions of flow-related quantities downstream of a BFS from their distributions in uniform flow can be seen in Figure 2.4.

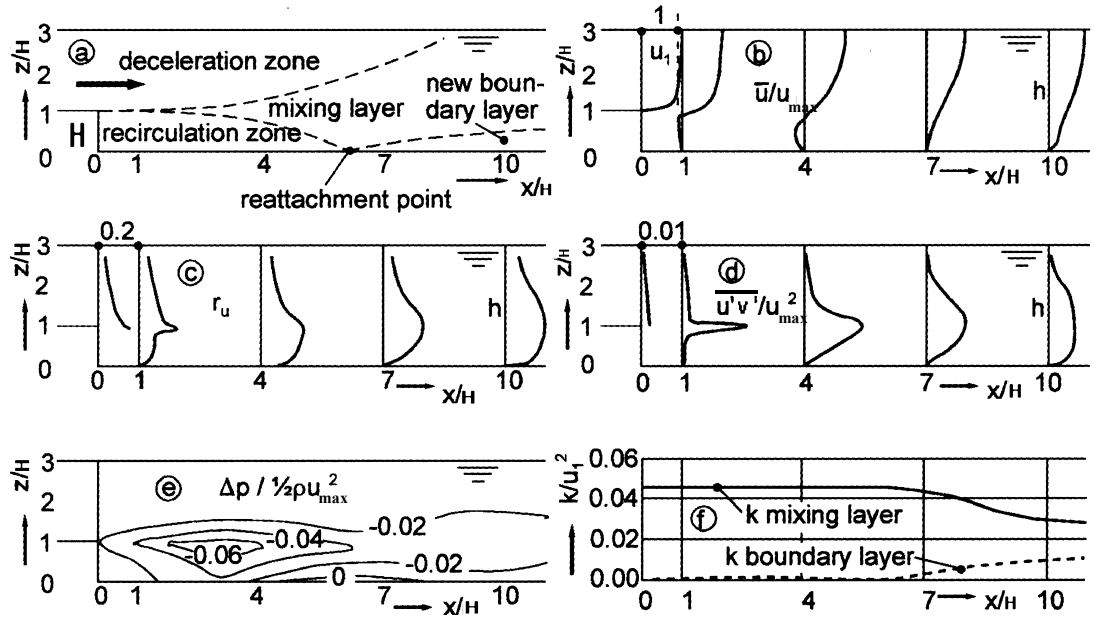

FIGURE 2.4 *Distribution of flow characteristics downstream of a backward-facing step (Schiereck, 2001)*

Figure 2.4a shows the main regions of BFS flow again, including the growth of the new boundary layer. In Figure 2.4b one can see the negative horizontal velocities in the recirculation bubble as well as the slow adaptation of the flow to the uniform state. Figure 2.4c gives an impression of the relative turbulence intensity (made dimensionless by the maximum time averaged velocity at the trailing edge of the step U_{max}, i.e. the mean velocity just below the water surface at $x = 0$). The dimensionless distribution of $\overline{u'v'}$ is visualised in Figure 2.4d and the deviation of the pressures from the hydrostatic pressure is illustrated in Figure 2.4e. These figures are taken from Schiereck (2001), based on the results of Nakagawa & Nezu (1987). A more extensive analysis of the vertical distributions of the mentioned and other quantities can be found therein. Figure 2.4f shows the transition of the turbulent kinetic energy k from the mixing layer to the new boundary layer. This figure is based on the results of Hoffmans (1993) who also proposed a formula to calculate the values of the relative depth-averaged turbulence intensity at locations downstream of the reattachment point of BFS flow (see section 2.4.5).

2.3.2 Three-dimensional instantaneous flow phenomena

When looking at the instantaneous flow phenomena downstream of a BFS from a three-dimensional point of view, the presence of coherent structures associated with turbulence with sizes up to $O(h)$ can be discerned. Vortical structures in the flow and their interactions are believed to play an important role in the generation of turbulent stresses, turbulent kinetic energy, shear layer entrainment and growth and mean flow development, which all may be linked in one way or another to stability of stones in a bed protection. In general, visualisations show a tendency of the vertical flow structures to reorientate from the spanwise direction into the streamwise direction. The largest structure in the flow originates from the roll-up and multiple pairing of spanwise vortices and is at least as large as the step height. The convective speed of these structures is about $0.6U_0$ (Simpson, 1989; Lee & Sung, 2002).
In the following, the terms *Λ-shaped*, *Ω-shaped (horseshoe)* and *hairpin* will be used. They refer to the shape of coherent structures that are more or less shaped like a hairpin (see e.g. Adrian *et al.*, 2000b), but some with specific deviations from the hairpin shape. Some are

somewhat more elongated, others nearly circular shaped, as indicated by their names. All do consist, however, of a head directed towards the high-momentum zone and two legs of which the sloping parts are called neck.

Delcayre and Lesieur (1997) identified three different regions in their LES of BFS flow at Re_H = 5100. Close to the step the flow is dominated by oscillating quasi two-dimensional Kelvin-Helmoltz rollers, which pair and increase the three-dimensionalisation of the flow. The topology of the flow is already completely changed at $x / H \approx 3$. Downstream of $x / H = 3$ the rollers undergo strong three-dimensional contortions and appear as Λ-shaped vortices. Further downstream (at about the reattachment location) they develop as intense hairpins (oriented with the head towards the high momentum region) as they impinge on the bottom wall and are convected downstream of reattachment. Figure 2.5 is a visualisation of this process.

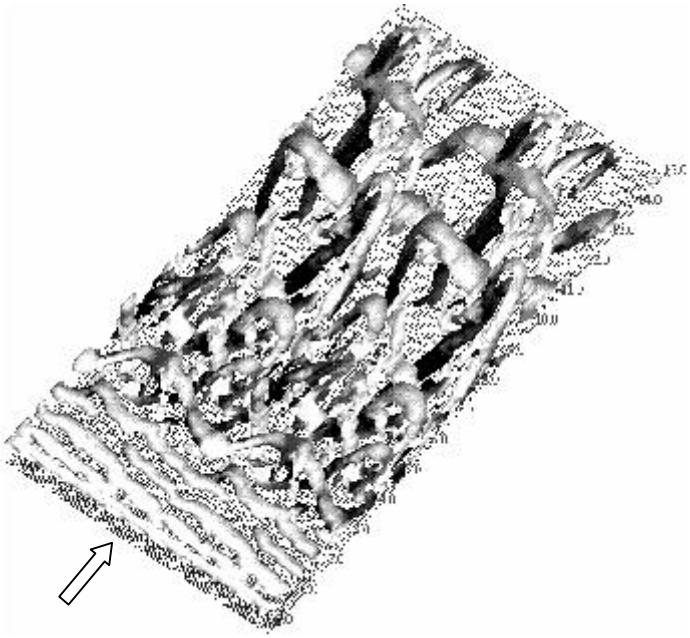

FIGURE 2.5 *Coherent structures downstream of a backward-facing step. LES by Delcayre & Lesieur (1997).*

Kostas *et al*. (2002) who conducted PIV measurements on BFS flow and visualised the flow by means of dye, encountered similar flow phenomena. They found that roll-up of the primary vortices (Kelvin-Helmoltz rollers) in the shear layer is most likely to occur somewhat downstream of the separation point ($x / H \approx 1.6$, $y / H \approx 1$) where a peak in turbulent kinetic energy production can be found. This region coincides with the more orderly type of vortex interactions, where small vortices are likely to undergo a first pairing. Further downstream, maxima in the Reynolds stresses occur, which are most likely associated with subsequent vortex pairing, vortex growth and transition of the vortices to the turbulent state, resulting in an enhanced mixing over the more planar-like interactions occurring closer to the step. Beyond reattachment relatively large-scale hairpin-like structures, as well as continuing vortex interactions can be encountered. These structures and interactions are responsible for the persistence of turbulent stresses in the redeveloping boundary layer region. They also contribute to the turbulent kinetic energy production downstream of reattachment, while small scales contribute to the intense Reynolds stresses in the vicinity of reattachment (Kostas *et al*., 2000).
According to Scarano *et al*. (1999) who conducted BFS flow experiments (also in the turbulent regime, Re_H = 5000) with an expansion ratio of 1.2, the separated shear layer is subjected to an oscillatory motion directly downstream of the step edge, where vortex roll-up

mostly occurs. Further downstream the interaction between the single vortices increases the flow pattern complexity. Nevertheless, they distinguished a large-scale pairing occurring intermittently and at different cross-sections ($2 < x / H < 4$). This pairing leads to high-amplitude fluctuations and therefore to an increased shear layer growth rate. Even further downstream the interaction between shear layer and vortical structures becomes weaker and the coherent structures seem to be advected with the surrounding flow velocity. Vortices are seen either to be ejected in the outer flow where they show a long permanence time, or they impinge onto the bottom wall at about the reattachment location, where presumably breakdown occurs.

They also deduced some statistical characteristics related to vortex occurrence and found that in general one can state that the larger the vortices, the less they seem to occur. Of the small vortices ($d / H = 0.12$, d = diameter of vortex = 2σ, σ = Gaussian damping factor used in expression that describes prototype vortex pattern) with the highest occurrence, the clockwise rotating vortices show a quasi-linear spreading from $x / H = 1$ to $x / H = 3.5$, were the bottom wall is reached. The counter-clockwise rotating vortices of this size are found in the step corner, but also occur with a significant population in the free shear layer downstream of $x / H = 4$. From the cross-sections $x / H = 4$ on, the vortex population is essentially advected in streamwise direction. The occurrence of vortices of a relative size $d / H = 0.28$ exhibits three main differences with respect to the smaller ones: (1) a larger occurrence of counter-clockwise rollers in the step corner; (2) counter rotating structures appear less frequent in the free shear layer; (3) a significant number of vortices occurs in the free stream. Vortices shed from the step edge with a relative size of $d / H = 0.44$ (or larger) were not distinguished, indicating that vortices of this extent are very seldom generated. The vortices of this size that were encountered were all supposed to already exist upstream of the trailing edge of the step. Christensen & Adrian (2002) showed that, at least for turbulent channel flow, the size of small-scale vortices changes slowly with the Reynolds number.

Scarano *et al*. (1999) believe that the counter-rotating structures, which are of opposite sign with respect to the background mean vorticity, are generated by a three-dimensional instability and breakdown of primary rollers. By averaging structures that were detected within the same domain subregion and centre-aligned to avoid smearing of the instantaneous patterns by the typical jitter in the structure location (as described in Scarano *et al*., 2000), they found that the presence of a counter-clockwise vortex is associated to one or more primary rollers appearing adjacent to it. Furthermore they conclude that the peak coherent vorticity of clockwise rotating vortices decays rapidly in the first three step units and that further downstream the process decays at a lower rate. For increasing diameters the peak vorticity decreases systematically. The small scale rollers ($d / H = 0.12$) showed peak values that are 1.2 to 1.5 times larger than the large ones ($d / H = 0.44$). The difference increased when moving downstream of the step. Counter-clockwise rotating vortices tended to gain in strength in the streamwise direction up to a strength that equals 50% of the corresponding primary rollers. Downstream the reattachment, increasing values of the vorticity indicated the rapid development of a wall boundary layer.

Perhaps a counter-clockwise rotating vortex is well capable of moving stones from a bed, as both the velocity it induces and the pressure gradient it generates can result in destabilising forces on a stone, acting simultaneously.

Frequency of quasi-periodic mechanisms

Flow around bluff bodies is often accompanied by the phenomenon of vortex shedding. The nondimensional frequency of these kind of oscillating flow mechanisms is defined by: the Strouhal number $S_r = fD / U$. In this formula f is the frequency of vortex shedding, D is a characteristic length scale and U is the velocity of the fluid.

When looking at instantaneous reattachment lengths it becomes clear that also BFS flow is highly unsteady since the short-time-averaged reattachment location can deviate from the

long-time-averaged reattachment location by as much as ± 2 step heights (Simpson, 1989). Often the mean reattachment length or step height is chosen as the characteristic length scale to acquire the Strouhal number. Besides this mechanism several other quasi-periodic mechanisms can be discerned. Several authors (e.g. Delcayre & Lesieur, 1997; Lee & Sung, 2002) have investigated the periodicity of the mechanisms and distinguished the accompanying frequencies. The mechanisms that may be relevant when it comes to the (location of) entrainment of stones downstream of a BFS are the oscillation of the reattachment length and the vertical or "flapping" motion of the shear layer (and perhaps vortex pairing).

The frequency f of the oscillation of the reattachment location is $0.6\text{-}0.8U_0 / X_R$ (Simspon, 1989), in which U_0 is the free-stream velocity upstream of the step. According to Nelson *et al.* (1995) this frequency is associated with vortex shedding from the separation point (Kelvin-Helmoltz instability). However, Lee & Sung (2002) state that the frequency of *large-scale* vortex shedding is $f = 0.065U_0 / H$, based on results from pressure measurements at $Re_H = 33000$. As they found that $X_R = 7.4H$ the frequency expressed in the mean reattachment length is $f = 0.48U_0 / X_R$. It is not clear whether this large-scale vortex shedding is the same quasi-periodic mechanism as the one Nelson *et al.* mentioned. The frequencies only coincide if $X_R = 10.77H$.

According to Simpson (1989), the frequency associated with the flapping motion does not exceed $0.1U_0 / X_R$. This agrees well with Lee & Sung who found that $f = 0.0136U_0 / H$, which together with $X_R = 7.4H$ gives $f = 0.1U_0 / X_R$. In general one can state that the frequency of the flapping motion is 6 to 8 times smaller than that associated with vortex shedding.

The streamlines of a flow field at various times in a flapping sequence show that the amplitude of flapping is less than 20% of the shear-layer thickness and that the flapping correlates with strong flow reversals in the vicinity of reattachment. A reduction in the reverse-flow rate with abnormally short instantaneous reattachment lengths can sometimes be found (Simpson, 1989). A more or less sawtooth shaped reattachment length time history was found by Lee & Sung (2002), which is believed to be caused by a constant downstream movement of the reattachment position along with the growth of a large-scale structure followed by a sudden retreat of the reattachment position when the vortical structure detaches from the shear layer. In more detail the cause of the growth-decay cycle of the recirculation bubble is ascribed to the inflation of the bubble caused by a temporary decrease of entrainment of fluid from the bubble by the shear layer, followed by a sudden release of fluid. The decrease of entrainment from the bubble by the shear layer, in turn, originates from a short-term breakdown in the spanwise coherence of the shear layer. However, slightly other explanations can be found as well. In Simpson (1989) it is suggested that the flapping is produced when a high-momentum structure reattaches far downstream, causing a somewhat greater pressure gradient and therefore a greater backflow. The flapping motion produces negligible contributions to the Reynolds shear stresses.

In addition to what is written in the section about three-dimensional instantaneous flow phenomena, a description of the quasi-periodic shedding of large-scale structures will be sketched. According to Lee & Sung (2002) a global intense oscillation appears first with the contraction of the separation bubble. As the bubble enlarges, the shear layer receives positive momentum in the streamwise direction. After a while a large-scale structure emerges and is then accelerated to form an orderly structure downstream of the bubble. After these periodic vortices are convected downstream, they decelerate and the next global oscillation develops.

2.4 Stability of coarse bed material

The flow around and the forces on particles have been the subject of many studies for many years, varying from fundamental research like determining the drag force on a falling sphere to the influence of turbulence on stone stability. Most of these studies are empirical. Our main interest obviously lies within the field of civil engineering, in particular in the stability of stones in the top layer of granular filters used as bed protections downstream of a BFS

(hydraulic structure). Still it is necessary to know first which forces act on a single stone and when they can make it move. Under low-mobility conditions bed particles are displaced intermittently with large periods of repose between movements, meaning that the mean destabilising forces alone are not large enough to displace a particle, otherwise the particles would move constantly. So, at the moment of movement of a bed particle the destabilising forces on the particle must be larger than average, indicating that turbulent fluctuations of the destabilising forces play an important role in the entrainment of particles from a granular bed. This is discussed first, discriminating between two main possible causes of entrainment as first distinguished by Hofland & Booij (2004), namely quasi-steady forces and turbulent wall pressures (TWP). On the other hand the position of a stone in a granular bed plays a key role in the stability of stones since it determines the exposed area, the protrusion into the mean flow, interlocking etc. It determines the flow around a stone and therefore the forces on it. The consequences of the position of a stone are enumerated only, for they are rather trivial. Since the present knowledge of the stability of stones (or sediment) in BFS flow is linked to the knowledge of the stability of coarse bed material in uniform flow and since existing design formulae for bed protections downstream of a BFS are based on design formula for uniform flow, the knowledge of the stability of coarse bed material in uniform flow is summarised before an overview of the knowledge of the stability in BFS flow can be given.

2.4.1 Quasi-steady forces

We do know, that it is always pressure gradients that cause stone movement, whatever the cause of the pressures may be. However, for the sake of simplicity, one often considers forces instead of pressures. Often the destabilising forces on a stone are thought to be a function of the velocities in the proximity of the stone only, following the law for the steady drag and lift force for large Reynolds numbers. Assuming this, low-frequency fluctuations of the velocities near the stone cause the forces to fluctuate as well. For this reason we refer to them as quasi-steady forces (QSF). The quasi-steady forces are mainly caused by an obstruction of the flow by the stone itself. We use this term to enable discrimination between these forces and another cause of entrainment, the turbulent wall pressures (TWP) that are described later on.

Equilibrium of forces

When of all active forces only the quasi-steady ones are considered, then four significant forces (shear force caused by skin friction is negligible) on a stone on the bottom under a flow can be distinguished, as is depicted in Figure 2.6. The active forces are the drag force F_d and the lift force F_l and are caused by the horizontal pressure gradient over the stone (stagnation pressure) and the streamline contraction (Bernoulli lift) respectively. Both are proportional to the squared horizontal flow velocity in the vicinity of the stone. According to the quasi-steady forces approach, a local increase of u-velocity near the stone is the only cause of entrainment.

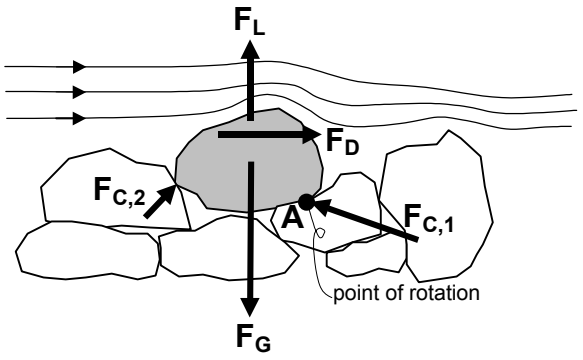

FIGURE 2.6 *Forces acting on a stone in a granular bed in a mean horizontal flow. The active forces F_d and F_l are thought to depend on the near-bed velocity only.*

The picture shows a 2-D flow that is only likely to cause movement of the stone in the mean streamwise direction. In BFS-flow it might well be possible that the instantaneous pressures are such that lateral movement of stones or even movement of stones in the direction opposite to the mean flow direction can occur.

The forces that keep the stone in place are the gravitational force F_g (= submerged weight = $(\rho_s-\rho_w)gV$, with V = volume of stone and ρ_s = density of stone material) and the contact forces $F_{c,i}$, with i the number of contact points with adjacent stones.

Of the active forces, the drag and lift force, we assume that the drag force acts upon the stone somewhat below the top of the stone and that the lift force acts in the same line of action as the gravitational force.

At the moment in time at which movement of the stone starts, there is either no equilibrium of forces (translation) or no equilibrium of moments around the point of rotation A (i.e. $F_{c,2} = 0$ in Figure 2.6). Several investigators found that incipient motion of coarse bed material is likely to be pivoting. However, sometimes also sliding of stones, before pivoting, was encountered.

Drag force & lift force

Since drag and lift forces are important for stone stability, they will be considered in somewhat greater detail in this section. Both drag and lift force on an object (e.g. a stone) in flowing water are usually given by:

$$F_d = \tfrac{1}{2} C_d \rho_w u^2 A \tag{2.17a}$$

$$F_l = \tfrac{1}{2} C_l \rho_w u^2 A \tag{2.17b}$$

In these widely used laws, the area A is not the same. For the drag force the (largest possible) vertical cross-section perpendicular to the approaching flow of the part of the stone that protrudes into the flow, would be the proper choice for A. For the lift force it would be more or less the area of the stone that would be seen if viewed from above (provided that the flow is horizontal). However, for simplicity, in both Eq. (2.17a) and Eq. (2.17b) the squared value of the nominal diameter d_n is often chosen for A. In highly turbulent flows the fluctuating part of the horizontal velocity is significant and consequently the use of the mean horizontal velocity for u in Eq.(2.17) does not seem to be a proper choice. Instead, one should use $\bar{u}^2 + (\sigma_u)^2$, see Eq. (2.9).

Formally the directions of the drag force and the lift force are in line with, and normal to the flow direction respectively. Only for mean horizontal uniform flow conditions do these directions coincide with the horizontal and vertical directions. Nevertheless, one often refers to the horizontal force component as drag, and to the vertical force component as lift, presumably originating from the fact that most research on drag and lift forces has been done under the mentioned flow conditions. For the sake of convenience we will go along with this terminology.

The coefficients C_d and C_l are called the drag coefficient and the lift coefficient respectively. They depend on the shape and orientation of the object in the flow. Since every stone is different there is no such thing as a universal drag or lift coefficient for stones. Most experiments that were conducted to determine drag and lift coefficients of particles on a wall involved spheres or hemispheres in uniform flow and resulted in values varying from 0.26 to 0.35 for C_d and values of 0.15 to 0.22 for C_l (e.g. Einstein & El-Samni, 1949), provided that the velocity was measured at $0.15d_n$ above the particle. The height $0.15d_n$ is the height for which the largest correlation between the instantaneous velocity and the drag force was found. If the shear velocity is used in Eq.(2.17), which is defined as $u_* \equiv (\tau_b / \rho_w)^{1/2}$ (where τ_b is the bottom shear stress), then much larger values for C_d are found.

Provided that the u-velocity is determined at a fixed relative position from the stone then the values for C_d and C_l are generally constants that only depend on the shape of the stone and

not on the flow conditions. However, Xingkui & Fontijn (1993), who conducted BFS flow experiments with $H / h_2 = 0.42$ and $Fr_1 = 0.67$, found an increase of C_d for growing distances from the step. Perhaps that was caused by the fact that not all horizontal forces that were measured by their dynamometer are covered by Eq. (2.17a). Some horizontal forces may have been caused by TWP originating from turbulent structures that did not affect the velocities in the vicinity of the dynamometer. Besides they deduced the drag coefficient from Eq. (2.17a) using the mean of the measured drag forces and the mean of the measured horizontal velocities. As mentioned before in BFS flow the use of the mean horizontal velocity does not seem to be a proper choice. If one instead substitutes $\bar{u}^2 + (\sigma_u)^2$, see Eq. (2.9), for the parameter u in Eq. (2.17a) to obtain C_d, then the following relationship is valid for this C_d and the drag coefficient as determined by Xingkui & Fontijn (hereinafter denoted by C_{dxf}): $C_{dxf} = C_d(1 + r^2)$. If it is assumed that C_d is indeed a constant then the observed increase of C_{dxf} with the distance from the step is not in line with the decrease of the relative turbulence intensity r in the streamwise direction downstream of the reattachment point. This may also indicate that other forces than the QSF have a large influence on the incipient motion of stones downstream of a BFS.

As the fluctuating parts of the drag and lift forces are crucial for the entrainment of stones we now focus on the fluctuating parts of these forces ($F' = F - \overline{F}$). With $u = \bar{u} + u'$ we find:

$$F_d' \propto 1/2\,\rho_w (u^2)' \approx \rho_w \bar{u} u' + 1/2\,\rho_w \left(u'^2 - \overline{u'^2}\right) \tag{2.18}$$

If no negative u-velocities occur Eq.(2.18) reduces to: $F_d' = \frac{1}{2}\rho_w(u|u|)'$.

For bed particles that are shielded by other particles, the drag force may also be dependent on the vertical velocity, as the main flow is able to reach a larger part of the particle if a downward flow component is present. For the fluctuating part of the lift force the following expression can be used (Hofland, subm.b):

$$F_l' \propto a\bar{u}u' + b\bar{u}v' \tag{2.19}$$

in which a and b are coefficients. Now only the linear term that results from the decomposing in mean and fluctuating parts of the u-velocity is included (first term on the right-hand side). The second term on the right-hand side accounts for what is stated before, namely that the vertical velocity may cause vertical forces.

To conclude this section about drag and lift forces, one final but rather important remark: Xingkui & Fontijn (1993) found that the normalised standard deviations of the drag force and the lift force are $\sigma_d / \overline{F}_d = 0.7$ and $\sigma_l / \overline{F}_l = 1.0$ respectively and that the distribution of the lift force is Gaussian except for the largest deviations from the mean. The latter deviations occurred more often than they would have done in the case of a completely Gaussian distribution. This is important because these peak values of the lift force may influence the entrainment significantly.

Origin of quasi-steady forces

Obviously the mean flow causes a permanent drag and lift force. This mean flow does not necessarily need to be horizontal. Near the reattachment zone for instance the mean flow is far from horizontal. The causes of the fluctuating part of the quasi-steady forces are plenty. In fact, each flow phenomenon that brings on fluctuations of the velocity in the vicinity of the stone, is a cause. One convenient way to discriminate between the origin of forces, is to divide the plane of possible (u', v')-combinations in four quadrants and investigate in which quadrant the measured near-bed velocities at times of stone movement (or a little earlier) are likely to fall. Four quadrants can be distinguished:

- The Q1 quadrant: $u' > 0,\ v' > 0$
- The Q2 quadrant: $u' < 0,\ v' > 0$
- The Q3 quadrant: $u' < 0,\ v' < 0$
- The Q4 quadrant: $u' > 0,\ v' < 0$

Since the quadrant analysis dates back to the days when only point measurements could be made (LDA), the different events (Q1 through Q4) are sometimes given wrong names. For instance: although sweep events are characterised by $u' > 0$ and $v' < 0$, not all Q4 events are sweeps. A sweep is a relatively large (height and length $O(h)$) zone with $u' > 0$ and $v' < 0$. So a small-scale event in which $u' > 0$ and $v' < 0$, as can be produced by a vortex, should not be referred to as a sweep. The other events are often named after coherent structures too: *ejection* (Q2), *inward interaction* (Q3) and *outward interaction* (Q1). From instantaneous flow fields one can deduce with a somewhat greater certainty if indeed such a structure is present. Only if that is the case we shall use these names, otherwise we use, for example, the term Q1-event. Of the four categories only the Q2 and Q4 events contribute positively to the mean (bed) shear stress. The quadrant analysis method will be encountered in the overview of the present knowledge of the stability of coarse bed material downstream of a BFS

2.4.2 Turbulent wall pressures

Besides quasi-steady forces we also distinguish turbulent wall pressures (TWP) as a possible cause of entrainment. As the name already unveils, TWP are pressures on a wall caused by the turbulence in a flow. Turbulence structures give rise to pressure fluctuations on the bed. The pressure that occurs somewhere in a flow (near the wall) is a weighted sum of every contribution of the whole flow field (Poisson equation). For this reason structures that are located slightly away from the wall may still contribute significantly to the TWP. Even in flows with a smooth wall TWP exist and they have nothing to do with e.g. the form drag of bed particles. One would expect that the TWP in a flow with a rough wall differ from those in a flow with a smooth wall, because the wall roughness influences the turbulence level (i.e. the types and frequency of occurrence of CS) and hence the TWP. However, Hofland *et al.* (subm.c) showed that his measurements of pressures around a bed particle in a coarse bed downstream of a BFS, are in accordance with the pressure distribution on a smooth wall downstream of a BFS as measured by Lee & Sung (2002), indicating that the influence of the wall roughness on the TWP may be neglected in that case and that the TWP were mainly a result of the overall flow configuration.

General formula to quantify forces generated by accelerations

In principal the Poisson equation can be used to quantify the wall pressure gradients on a bed. However, to get a notion of how fluid motions create TWP, i.e. forces others than the quasi-steady ones, we distinguish two consequences of accelerations and decelerations. First, the change of fluid motion involves ambient pressure gradients as expressed by the Euler equation for dynamic pressures. Secondly, whenever an object is present in an accelerating or decelerating flow another force, known as the added mass force, is generated, which can be expressed by the same parameters as the ambient pressure gradient. The interpretation of added mass is an additional local pressure gradient, which exists in order to accelerate the neighbouring fluid around the object (in our case a bed particle or stone). The resultant force generated by both the ambient pressure gradient and the added mass force is given by:

$$\vec{F} = \rho V \frac{D\vec{u}}{Dt} + \rho V C_m \left(\frac{D\vec{u}}{Dt} - \frac{d\vec{v}_p}{dt} \right) \tag{2.20}$$

in which C_m is the added mass coefficient and $\bar{v}_p$ the velocity of the particle. The first term on the right-hand side denotes the force due to the ambient pressure gradient and the second one the added mass force. As we did not include in this report mechanisms that occur after a particle is dislodged from the bed, the velocity of the particle equals zero. Tromp (2004) estimated C_m to range from 1.7 to 2.75 for natural shaped stones in a bed and with about the same size and shape as the ones used in the present experiments. This value is much larger than was first expected (for comparison: $C_m = 0.5$ for a sphere).

From Eq.(2.20) it is known that TWP are associated with accelerations in the flow. They fluctuate relatively quickly, while QSF result from velocities and change relatively slowly. Both the accelerations and the velocities need to occur in the vicinity of the bed in order to generate forces upon the stones in the bed. The causes of accelerations and velocities near a bed are numerous (e.g. sweeps). Obviously also CS can cause them. For one of these coherent structures, a vortex, this is explained below.

Vortex-induced TWP

A horizontal migration of a simple 2-D point vortex in uniform potential flow at a fixed distance from a wall was used by Hofland *et al.* (subm.c) to gain insight on the pressure distribution on the bottom and the accompanying net resulting force on a bed particle. The wall was modelled by means of a mirrored vortex with the same strength (rotation) κ as the original one. In the following figure the result of this analysis is depicted:

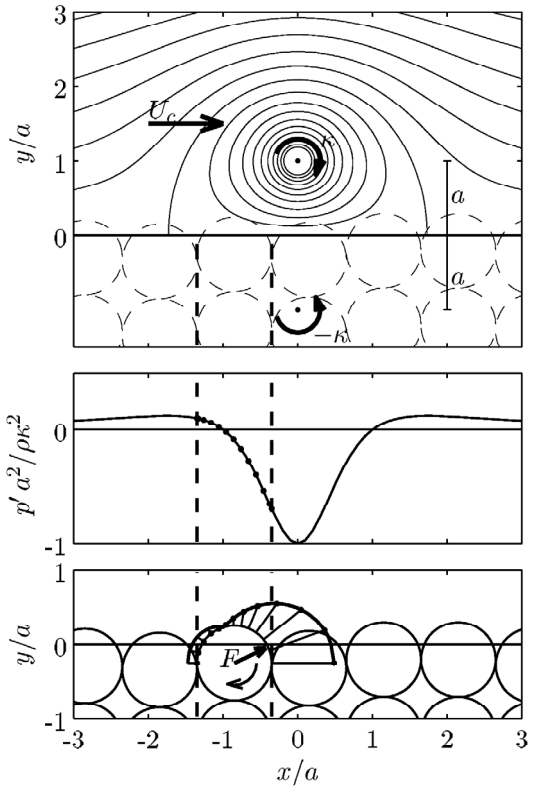

FIGURE 2.7 *A model-vortex (upper plot) and its accompanying pressure distribution on a wall (middle plot). The resulting pressure field around the particle between the dashed lines and the resulting net force are depicted in the bottom plot.*

In Figure 2.7 the pressure is denoted by p' to indicate that it is only the pressure caused by the vortex that is plotted and x represents the distance along the wall. The velocity induced by the vortex at a distance r from it, is κ / r. The convection rate of the vortex itself (U_c) is the sum of the mean flow velocity U_0 and the translation speed of the vortex brought about by the mirrored vortex: $U_c = U_0 - \kappa / 2a$, where a is the distance from the vortex to the wall.

It can be seen that at a position of the vortex as depicted in Figure 2.7, a negative horizontal pressure gradient over the stone occurs, resulting in a drag force and an added mass term. At the moment that the vortex is located exactly above the stone, a negative vertical pressure gradient occurs, resulting in a positive lift force. Large pressure gradients are created by vortices close to the bed, as the pressure gradient is proportional to a^{-3}. If a vortex is closer to a stone in the bed than half of the diameter d of the stone, the pressure dip becomes too small to be effective. The frequency of the forces originating from near-bed vortices is high as they pass quickly. Since the convection velocity of a vortex decreases as its strength increases, a strong vortex not only creates large, but also relatively long lasting forces. Because of the inertia of a stone, the relatively long presence of a destabilising force is required to dislodge a stone from its pocket. Strong forces that only briefly exist may not be capable of moving a stone. In general lower frequency TWP are caused by larger scale fluctuations further away from the wall.

From the above we can conclude that the influence of CS on forces on stones in a granular bed can be twofold: on one hand they may alter the near-bed velocity and hence the quasi-steady forces, on the other hand they can cause TWP. However, a coherent structure does not necessarily influence both the TWP as well as the QSF. The structure can be present for too short a period of time to be of influence on the QSF. An example: a structure passing a stone in a bed can cause the velocity in the vicinity of the stone to increase and change back again to its former value in a very short period of time (large accelerations, and hence large forces (TWP) on the stone), but at the same time it can pass too fast to be of influence on the QSF. To change the drag force, for instance, also the flow field behind the stone must have time to adapt to the new situation, because this influences the horizontal pressure gradient over the stone and hence the drag force.

Sometimes a coherent structure may contribute to the entrainment of a stone via both force generating mechanisms, like a counter-clockwise rotating eddy that both enlarges the drag force and creates a pressure distribution on the stone that is favourable for making it move. Addition of these two mechanisms is widely known as the Morison approach.

One final fact that has not been mentioned before, but is definitely noteworthy, is that in a porous granular bed a pressure gradient is able to penetrate further into the bed than the longitudinal velocity. Pressures gradients will therefore probably become more important for entrainment as a particle is more shielded by surrounding particles, which may be expected to be the case for the smaller grains of the bed.

2.4.3 Position and size of a stone

Position

An overview of the influence of the positions of particles on entrainment can be found in Hofland *et al.* (subm.a). The position of a stone can, among others, be described by it protrusion Π and its exposure e, which are defined as the height of the top of a stone above a defined mean bed level and the height of the top of a stone related to local, upstream mean bed level respectively. The most important consequences of altering the relative protrusion Π / d are: (1) the exposure changes, which causes an alteration of the (mean) drag force; (2) a large relative protrusion in general goes hand in hand with a pivoting angle of the stone that is such that a drag force gives a large moment around the point of rotation and (3) in cases of a small relative protrusion, only a lift force can create large moments.

About (1) a few aspects important for the present research can be concluded from experiments conducted by Hofland *et al.* (subm.a). His tests showed that for the most exposed particles the fluctuating drag force is dependent on u only. For less exposed particles the drag force was found to be dependent on both u and v and for the least exposed particles the drag force was almost totally dependent on the vertical velocity only. The possible explanation that was given, stated that when a stone is shielded by upstream stones, a downward flow is necessary to let the flow reach the stone. From this, one can gather that for a semi-shielded stone the net effect of a negative (downward) vertical velocity together with a positive longitudinal velocity is not directly clear. The longitudinal velocity produces a drag force (destabilising), while at the other hand the negative vertical velocity creates a negative lift force (stabilising).

According to Fenton & Abbot (1977) a value of $\Pi / d \approx 0.46$ is equivalent to $\Psi_c \approx 0.03$, where Ψ_c is the critical Shields parameter based on the bed averaged shear velocity u_* (see next paragraph). Since $\Psi_c \approx 0.03$ corresponds to low-mobility transport of bed material, $\Pi / d \approx 0.46$ seems a reasonable value to choose if one is interested in the failure of bed protections.

Size

The influence of the size of a stone on its stability is manifold. It affects the weight of a stone, the exposed area, the protrusion, the added mass force, its inertia, etc. How these aspects influence the stability of a stone can to a large extent be derived from the previous sections. One convenient fact that has not been mentioned before is that the nominal diameter d_n (= $V^{1/3}$) is the best characteristic size to use when dealing with stability of grains, because different materials with differently shaped grains have a more or less equal Ψ_c-value if their d_n-values are the same.

2.4.4 Stability of coarse bed material in uniform flow

In one of the previous sections, the forces on the individual stones of a coarse filter were described. However, in practice a coarse filter used as a bed protection is not designed or made stone by stone. Instead the engineering approach is a more integral approach that is aimed at designing a bed protection that is stable as a whole. It is also not the intention to make a model that predicts the stability of each individual stone in a bed protection. What is desired, is to have a model from which can be deduced what the average size of stones in a bed protection must be to withstand certain flow conditions with a certain amount of allowed transport (damage). The overall final aim is to arrive at a more fundamental, less empirical design criterion for bed protections that is based on the underlying physical phenomena that are the cause of the transport of stones.

We mention the engineering approaches that are most used today. In these approaches, the designs of bed protections under nonuniform flow conditions are oftentimes based on criteria for uniform flow conditions with a correction for the increased turbulence level. Therefore we start with the stability of coarse bed material under uniform flow conditions. However, since stability under uniform flow is not the main concern of this research, we will restrict this section to the most used design criterion, namely the one by Shields (1936).

Shields

Most design approaches for uniform flow are based on the well-known criterion that was introduced by Shields (1936), who conducted experiments on the stability of coarse bed material in uniform flow. This formula is based on the dimensionless ratio between load and strength that can be derived from considering the horizontal, vertical or moment equilibrium of the forces on a stone as depicted in Figure 2.6 and reads:

$$\Psi = \frac{u_*^2}{\Delta g d} = \frac{\tau_b}{(\rho_s - \rho_w) g d} \tag{2.21}$$

in which $\Delta = (\rho_s / \rho_w - 1)$ and Ψ is a stability parameter. Shields used $\tau_b d^2$ as the active force, which together with the definition of the shear velocity u_* results in Eq. (2.21). For d most of the times the d_{n50}-value (see appendix B for the definition) of the stones in the top layer of a granular bed is chosen.

Shields considered continuous movement of grains at each location in the bed to be the threshold of motion. The parameters that are deduced from the flow that accomplished this continuous movement, are called critical parameters and are indicated by the subscript c. The parameter Ψ_c, which is called the critical Shields parameter and is based on the critical shear velocity u_{*c}, turned out to be a function of the particle Reynolds number Re_* defined as:

$$\mathrm{Re}_* = \frac{u_* d}{\nu} \tag{2.22}$$

However, for $Re_* > 500$ the critical Shields parameter becomes constant ($\Psi_c = 0.055$). This is always the case for real-life bed protections, but also during our experiments Re_* exceeded this value.

For nonuniform flow conditions, the Shields design criterion no longer holds. For an adequate prediction of the stability of coarse bed material in nonuniform flows like BFS flow, the increased turbulence intensities and fluid accelerations have to be taken into consideration.

2.4.5 Stability of coarse bed material in backward-facing step flow

For the design of the experimental set-up, for comparing the results of our tests with other experiments and to try to come to somewhat adapted (improved) or even new insights in the stability of stones downstream of a BFS, an overview of the present knowledge of the stability of coarse material downstream of a BFS is essential. From such an overview it may be evident that regions can be distinguished that have to bear a more severe bed attack than average. Several authors have observed this in their experiments, but despite this, bed protections generally are designed and build as if the whole protection has to be able to withstand the maximum flow attack.

Engineering approach

As stated before, the present-day design methods for granular filters in nonuniform flow are based on uniform flow conditions with a correction for the increased turbulence intensity. From the previous sections it is clear that it is, among others, the extreme values in the velocity that are important when it comes to incipient motion. Since the peak velocities can be related to the turbulence intensity r, the altered turbulence level is often taken into account by using a factor for the velocity (K_v) which is based on the turbulence intensity r. If it is assumed that the peak velocities deviate from the mean velocity by three standard deviations ($\bar{u} + 3\sigma_u = (1+3r)\bar{u}$) and if K_v is defined as the ratio of the time and vertically-averaged critical velocity in uniform flow ($<\bar{u}>_{h,c,u}$) to the time- and vertically-averaged critical velocity in BFS-flow ($<\bar{u}>_{h,c,BFS}$), this yields:

$$K_v = \frac{<\bar{u}>_{h,c,u}}{<\bar{u}>_{h,c,BFS}} \approx \frac{1+3r_u}{1+3r_{BFS}} \tag{2.23}$$

The parameter K_v can be obtained either by measuring velocities and computing the turbulence intensity in the BFS flow r_{BFS} (for uniform wall flow the turbulence intensity is r_u

≈ 0.1) or, as a first estimation, the depth-averaged turbulence level can be used at the point where the maximum flow attack can be expected (this point is not specified in this design approach; if it is not known at all a large area of bed protection will have to be dimensioned with the maximum stone diameter). The depth-averaged turbulence intensity downstream of a BFS can be calculated by a formula that can be found in a guideline used by the Dutch Ministry of Transport, Public Works and Water Management, see Franken *et al.* (1995), and that was first proposed by Hoffmans (1993):

$$r(x) = \sqrt{0.5k_0\left[1-\frac{H}{h}\right]^{-2}\left[\frac{x}{\lambda}+1\right]^{-1.08} + 1.45c_f} \tag{2.24}$$

in which λ is a relaxation length (≈ 6.67h), k_0 is the relative turbulent energy in the mixing layer (≈ 0.045), h the water depth downstream of the BFS and x is the distance downstream of the reattachment point!

The fact that a depth averaged value for r is used, seems to be based on practical reason rather than on physical considerations. In cases that $h_2 / H >> 1$ the depth averaged turbulence intensity is low, while the turbulence intensities near the bed can be high.

For a lot of flow configurations K_v has been determined experimentally by means of scale models by examining the stability in both uniform flow and at the place of interest in the desired flow configuration. For a BFS this has been done by De Gunst (1999) and for a sill by Schiereck (2001, after DHL, 1985). (In the next section more details about these experiments are given.) Once K_v is known it can be used in stability relations as a factor for the velocity. In case the Shields formula (Eq. (2.21)) is used this yields (Schiereck, 2001):

$$d = \frac{c_f\left(K_v < \bar{u} >_{h,c,u}\right)^2}{\Delta g \Psi_c} \tag{2.25}$$

In this formula $c_f \equiv (u_* / <\bar{u}>_h)^2$. There are other design approaches for nonuniform flow, like the one recently proposed by Jongeling *et al.* (2004). This approach links the outcome of a k-ε model to a stability parameter similar to the Shields parameter. It includes the influence of turbulence on entrainment in a much more sophisticated way than was usual in the existing design approaches:

$$\Psi_{WL} = \frac{<(\bar{u}+\alpha k)^2>_{h_m}}{\Delta g d_{n50}} \tag{2.26}$$

Herein α = 6 and both $\bar{u}$ and k result from a k-ε model and are averaged over a height above the bed given by $h_m = 5d_{n50} + 0.2h$. The critical value of the stability parameter Ψ_{WL} was found to be $\Psi_{WL,c}$ = 8. Although the influence of turbulence is included and as a result different required stone sizes can be calculated for different locations in the flow, it does not distinguish causes of entrainment.

Results from foregoing experiments

Even when the mean horizontal flow is zero in the reattachment zone and the bottom shear stress τ_b cannot be properly defined in this region, the damage or attack on the bed in this area is large (De Gunst, 1999; Xingkui & Fontijn, 1993; Schiereck, 2001). Due to the overall loss of kinetic energy in decelerating flows like BFS-flow, the turbulence level is much higher than in uniform flow, which is held responsible for the aforementioned damage. The mean

flow velocity that is required to move stones downstream of a BFS is approximately 15% less than in uniform flow, in case step height/downstream water depth (H/h_2) ≈ 0.345 (De Gunst, 1999). For another ratio of step height and downstream water depth, the relationship that is depicted in the following figure can be used (Schiereck, 2001 after DHL, 1985):

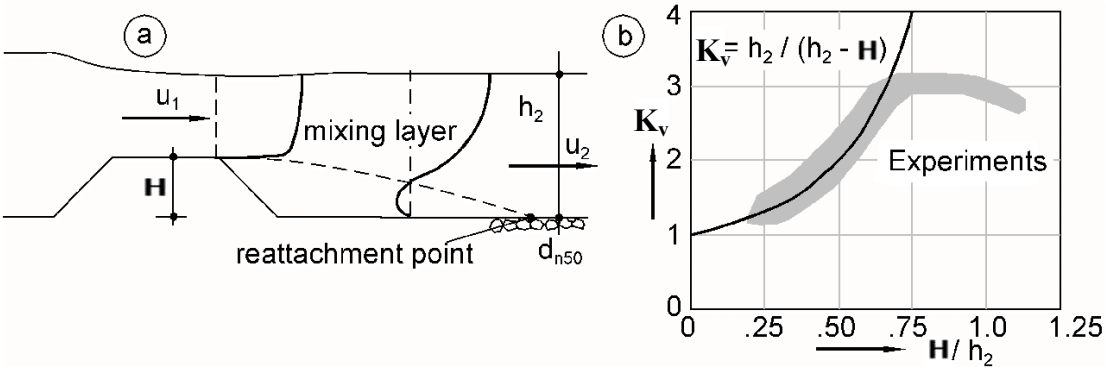

FIGURE 2.8 *Stability of stones near reattachment point downstream of a sill. K_v is a factor that indicates how many times the velocity, averaged over the depth and in time, at the reattachment point can be lower than the same defined velocity in uniform flow and still causes the same amount of bed damage (Schiereck, 2001, after DHL, 1985).*

Note that the relationship in Figure 2.8 is only valid in the vicinity of the reattachment point and that this relationship is actually for a sill and not for a BFS. The required depth averaged, mean uniform flow velocity divided by K_v yields the required depth averaged, mean flow velocity downstream of the sill near the reattachment point (see the engineering approach section for a definition of K_v). If it assumed that the water surface is horizontal ($h_2 = h_1 + H$), then from conservation of mass it can be deduced that: $u_1 = h_2 / (h_2 - H)\, u_2$. If it is also assumed that the total energy of the flow from the top of the sill remains constant up to the reattachment point and that the stability there can be described by the velocity on top of the sill, then this relation can also be written as $u_1 = K_v\, u_2$, with $K_v = h_2 / (h_2 - H)$. The results of experiments (grey area) justify this approach for sills with a height up to 65% of the water depth. So Figure 2.8 actually states that if the mean depth-averaged flow velocity on top of the sill is equal to the mean depth-averaged uniform flow velocity, the damage to the bed near the reattachment point is the same as that in uniform flow. The mean flow velocity needed to move the target stone in case of uniform flow conditions was known (from our uniform flow experiments).

According to Figure 2.8 $K_v = 1.5$ for $H / h_2 = 0.34$, while De Gunst (1999) found from experiments that $K_v \approx 1.2$ for a BFS with the same ratio H / h_2 and the use of a rigid lid. She used two ways to determine K_v, namely (1) to interpret it as the ratio of critical velocity in uniform wall flow to the critical velocity in BFS flow and (2) by measuring turbulence intensities. Both approaches yielded this value. In a third method (3) she used a simplified version of Eq. (2.24) and found $K_v = 1.3$.

Actually K_v is a function of x: for each cross-section a different local depth-averaged velocity is needed to get the same amount of damage (a same value for Ψ_c). This results from the fact that the relative turbulence intensity changes with x. Hence one has to bear in mind for which location K_v is valid. De Gunst did not specify which location she used for (1)* and (3); for (2) it was at $x = 8.1H$ (the mean reattachment point was located at $x = 6.5H$). She did however determine at which locations the highest damage occurred by counting the number

* De Gunst also used method (1) once with a location specified, namely the reattachment zone. This yielded $K_v = 0.93$. Hence $\langle \bar{u} \rangle_h$ in the reattachment zone downstream of the BFS had to be larger than $\langle \bar{u} \rangle_h$ in a uniform flow with the same water depth in order to cause the same damage.

of stones that had moved. From the reattachment point to 2.5H downstream of it, the damage was the most severe. In this area a scour hole developed with its centre located at 8H. In the area a bit upstream of the reattachment point stones had moved in the negative x-direction. In the whole area that spans from the reattachment point to 18H downstream of the step, the transport of stones was relatively large.

As mentioned before, Xingkui & Fontijn (1993) also conducted experiments on a BFS flow. Their experiments were conducted under the following conditions: $H / h_2 = 0.42$, Re = $5.03 \cdot 10^4$ (based on U_1 and h_1) and the Froude number upstream of the step edge (Fr_1) was 0.67. The latter is quite high; certainly there must have been significant undulations in the free water surface. Downstream of the step the bottom was covered with closely packed natural shaped roughness elements (rubble-stones) of which one of them was attached to a dynamometer and acted as a measuring stone. Their results that have already been mentioned in the previous sections are not repeated here.

They used fixed increments to change the position of the trailing edge of their step with respect to the dynamometer and conducted measurements at six different distances downstream of the BFS. The mean drag force and the mean longitudinal flow velocity squared $\bar{u}^2$ ($\neq$ mean of u^2) showed a mainly linear relationship for each measuring location, provided that the velocity was measured at 0.15d above the stone. For the lift force this only held for a distance of 18 step heights or more downstream of the step edge. Although they stated that the mean reattachment location was about 8 step heights downstream of the step, results in the form of graphs are only given for absolute values of the horizontal co-ordinate. Inside the recirculation zone the forces on the measuring stone were slightly larger than outside. The lift force stayed positive, while the drag force attained large negative values. At 14 and more step heights downstream of the step, the standard deviation of the forces had at least the same order of magnitude as their accompanying mean values. A heavy attack on the cover layer occurred at 10 to 20 step heights downstream of the step edge. For locations relatively far downstream there was a probability of 16% that the instantaneous force exceeded the mean force by a factor two.

Nelson *et al*. (1995) were mainly interested in the cause of sediment transport downstream of a BFS and therefore conducted experiments in a duct with $H / h_2 = 0.2$ and sand with a mean diameter of 0.9 mm on the bottom wall. By filming the movement of the sediment and simultaneously measuring fluid velocities by means of a LDA, they could determine if, and how much, each of the categories Q1 through Q4 (see section about the origin of forces) contributed to the sediment transport. They found that Q4 events ($u' > 0$, $v' < 0$), which contribute positively to the mean bed shear stress, collectively moved the majority of the sediment, primarily because they were the most common. Q1 events ($u' > 0$, $v' > 0$), which contribute negatively to the bed shear stress, individually moved as much sediment as Q4 events of comparable magnitude and duration but were relatively rare. Both events transported much more sediment than Q2 and Q3 events. From this it can be concluded that, although the bed shear stress can be used to estimate the bed load transport for flows with well-developed boundary layers, it is not accurate for flows with developing boundary layers, like BFS flow, of which the turbulent fluctuations even close to the bed do not necessarily scale with the local bed shear stress. Significant spatial variations in the magnitudes and durations of the different events produce significant peaks in the bed load transport.

Furthermore, relatively low frequency fluctuations in the measured velocity time series were visible, caused by the vortex shedding and wake flapping mechanisms that have been described before. In fact a velocity time series, measured at 25 step heights downstream of the step edge, looked more like one measured at 10 step heights from the step than one measured without the presence of a BFS. The presence of these low-frequency, large-scale motions significantly affected the sediment transport. Fluctuations with high magnitude and low frequencies were important in the entrainment and movement of sediment, but not to the degree that those with higher frequencies could be neglected. In the case of stones the latter

might be of lesser importance, because of the difference in size and inertia of stones and sediment.

A significant positive correlation was apparent between streamwise velocity and sediment flux, while a weakly negative correlation between vertical velocity and sediment flux meant that transport tended to be higher when the vertical velocity was directed towards the bed. A strongly upward velocity also increased the transport of sediment. During sweeps, downward flow enhanced transport by advecting flow with higher streamwise velocity toward the bed and during outward interactions upward flow tended to move particles away from the bed into regions with high streamwise velocity, thereby increasing their speed and hence the transport rate. However if the effect of outward interactions on sediment transport is indeed mainly caused by this last mentioned process, then the role of outward interactions on low-mobility transport of stones can be completely different. During flow conditions that cause low-mobility transport of stones, advecting stones into the higher momentum zone is out of the question. Besides we restrict our analysis to the cause of entrainment; what happens to a particle once it has been dislodged is beyond the scope of our research.

The tendency for the most effective events to be Q1 events near the step and to shift to Q4 events with increasing distance downstream, as was observed by Nelson *et al*, was explained by the decreasing magnitude of the Q1 events as the large, low-frequency eddies associated with flapping of the free shear layer and vortex shedding from the separation point dissipated.

As identical (u, v) pairs yielded different transport rates, the turbulence structure that causes u and v as well as the duration of the event seemed to play an important role. Obviously, the turbulent structures could not be unveiled with the use of a LDA. In fact, they suggested using temporal and spatial techniques like PIV to uncover the CS.

A major consequence of the results of the experiments by Nelson *et al*. is that for nonuniform flow the variation of magnitude and frequency of turbulence structures near the bed can contribute dramatically to the transport of sediment without changing the bottom shear stress, making the latter useless for the prediction of the stability of bed material in these kinds of flows.

2.5 Particle Image Velocimetry (PIV)

2.5.1 Introduction to particle image velocimetry

In the following the basic features of the PIV measurement technique will be described briefly. The experimental set-up of a PIV system typically consists of several sub-systems. In most applications tracer particles (seeding) have to be added to the flow, as is the case in this experiment. These particles have to be illuminated in a plane of the flow at least twice within a short time interval. The light scattered by the particles has to be recorded either on a single frame or on a sequence of frames. The PIV method that was used is the so-called double frame/single exposure method, in which the particles are illuminated twice and each image is recorded at a different frame (Raffel *et al*., 1998). The displacement of the particle images between the light pulses has to be determined through evaluation of the PIV recordings. Each pair of frames finally results in one vector field. In order to be able to handle the great amount of data that can be collected employing the PIV technique, sophisticated post-processing is required.

Interrogation Windows

For evaluation the digital PIV recording is divided in small subareas called “interrogation windows”. The local displacement vector of the tracer particles of the first and second illumination is determined for each interrogation area by means of cross-correlation. It is assumed that all particles within one interrogation area have moved homogeneously between two illuminations. The local flow velocity of the fluid in the light sheet corresponding to an interrogation area, can be calculated if the time delay between the two illuminations and the

magnification at imaging is taken into account. The process of interrogation is repeated for all interrogation windows of the PIV recording, as schematised in Figure 2.9.

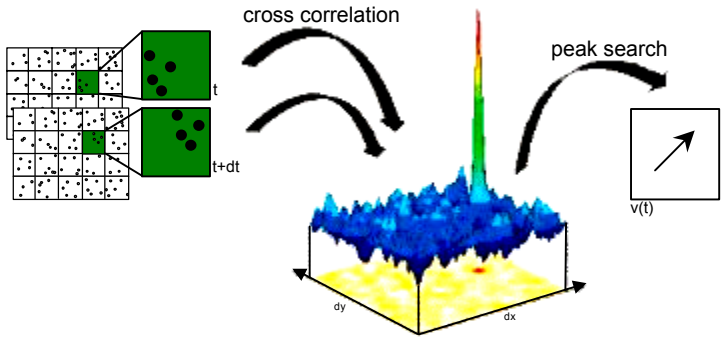

FIGURE 2.9 *Illustration of how the average velocity of the seeding particles in one interrogation window is obtained (taken from the website of LaVision: www.piv.de).*

The number of interrogation windows and hence the number of velocity vectors depend on the number of pixels of the camera and the size of the interrogation windows. The size of the interrogation area must be small enough for velocity gradients to have no significant influence on the results. We used a multi-pass method, which started with relatively large interrogation windows to roughly calculate the displacement vector, followed by a second pass in which the interrogation window sizes were decreased and the displacement obtained from the first pass was taken into account by shifting the interrogation window of the second frame according to this displacement vector. In this way the chance that the tracer particles in the first frame were the same ones as those in the second frame was enlarged, so the reliability of the calculated cross-correlation and hence of the resulting velocity vector was increased. Furthermore, most of the time the final interrogation windows overlapped to enlarge the spatial resolution of the velocity map.

Seeding particles and illumination

The tracer particles must be small enough to avoid discrepancies between the velocity of the fluid and the velocity of the particles. On the other hand they have to be large enough to reflect enough light of the light source towards the camera. As a result of turbulence, locally large accelerations of the water can be expected. Since the velocity lag of a spherical particle in a continuously accelerating fluid is proportional to the diameter of the particle, the seeding particles have to be relatively small. In order for these particles to scatter enough light to expose the CCD chip of the camera in a way that recordings of sufficient contrast can be obtained, a powerful light source is required. That is why generally a laser is used.

Advantages of PIV

The PIV technique has some advantages compared with formerly used techniques. It is based on the direct determination of the two fundamental dimensions of the velocity: length and time. On the other hand, the technique measures indirectly as the velocities of the tracer particles are measured. Since it is an optical velocity measurement technique it is nonintrusive. But the main advantage of PIV is that it is a whole-field technique, albeit two-dimensional in the set-up we used, which allowed us to instantaneously capture relatively large parts of the flow field. Until recently it was not possible to quantify turbulence in a two-dimensional area. It was possible to make coherent turbulence structures visible by means of dye injection techniques or smoke, but this resulted in qualitative visualisations only. It was

also possible to measure velocities with high sample rates, so high frequent, turbulent velocity fluctuations were included, but only at one or, at most, a few locations simultaneously. By repeating the measurements at many different locations, it was possible to obtain a whole velocity field, but obviously only time or conditionally averaged velocity fields could result from these point measurements. It was not possible to measure an instantaneous velocity field at once.

2.5.2 Interpretation of vector fields obtained by Particle Image Velocimetry

Once the velocity fields are obtained, one can start with the analysis of the vector fields. In our case the objective is to unveil whether coherent turbulent structures exist that induce entrainment of stones. One can start by just looking at the vector fields and try to detect some kind of structure around the time the stone starts to move. Notwithstanding that PIV is a excellent flow visualisation tool, by merely looking at the vector fields without using additional visualisation techniques, a lot of information will remain unnoticed. Therefore some visualisation techniques will be discussed in this paragraph. Nonetheless, one should not forget to try to take advantage of the quantitative nature of the data. After all by using the PIV technique velocities are measured with rather great accuracy in both the spatial as well as the temporal domain.

Definition of a vortex

Since most of the times PIV measuring areas are two dimensional and coherent structures (CS) are three dimensional, only cross-sections of the CS are captured resulting in so-called footprints or signatures of the CS. Often a CS has a rotating part, referred to as *vortex*. Most visualisation techniques therefore attempt to reveal vortices from PIV fields. A widely used definition of a vortex is the one that can be found among others in Adrian *et al.* (2000a) and reads:

”*A vortex exists when instantaneous streamlines mapped onto a plane normal to the core exhibit a roughly circular or spiral pattern, when viewed in a reference frame moving with the center of the vortex core”*[*].

Galilean decomposition

A key condition in the above-formulated definition of a vortex is that the velocity field must be viewed in a frame that moves at the same velocity as the core of the vortex. If a turbulent field consists of large-scale motion with many small-scale vortices embedded within it, it will only be possible to recognise a vortex if the velocity at the centre of the vortex is removed. One way of doing this, is to subtract one constant convection velocity from the whole velocity field. This decomposition of the velocity field is known as *Galilean decomposition*. It is evident that one must consider a range of convection velocities in order to identify the majority of the turbulent eddies. In PIV, the measured vector field is often averaged over the entire field of view and this value, often called the bulk velocity U_B, is then subtracted from the total field. If other convection velocities are subtracted, then they are often expressed as a fraction of U_B. To detect a vortex and pinpoint its location it is not necessary to subtract the exact convection velocity, for a vortex is still recognisable in a frame of reference that does not follow exactly the eddy’s core. However, the velocity vector pattern is not completely circular in those cases (Adrian *et al.,* 2000a). The same holds for vortices of which the core is not exactly perpendicular to the measuring plane. An advantageous attribute of Galilean decomposition is that it does not affect velocity gradients, for at all positions in the flow the

[*] In fact this is not a definition of a vortex, but a characteristic of a vortex. The vortex itself exists also outside the measurement plane. As a result, a rotating motion in a 2-D velocity field that is often called a vortex, is actually not a vortex but only a part of it.

same velocity is subtracted. As a result the local swirling strength, as defined in section 2.2.3, and the pressure sources remain unaltered.

Reynolds decomposition
Subtracting the time-averaged velocity at each location in the flow from the corresponding instantaneous velocity is called *Reynolds decomposition* and is the traditional method of decomposing a turbulent velocity field. It does a fair job of revealing the small-scale vortices and tends to unveil more vortices than any single Galilean decomposition, because the vortices frequently move at velocities close to the local mean velocity. A drawback of Reynolds decomposition is that it removes large-scale features that are associated with the mean flow such as large regions of relatively uniform momentum. Additionally, Reynolds decomposition obscures Q2 events associated with clockwise rotating vortices close to a bottom wall in uniform flow (Adrian *et al.*, 2002).

It is worth mentioning that if a flow is not characterised by a dominant flow direction, decomposition has to be performed in two perpendicular directions of the PIV field. In the present measurements, though obtained from a highly 3-D flow, vertical decomposition hardly changed the vector fields appearance and will therefore not be employed.

Vortex identification by means of the local swirling strength λ_{ci}
A very useful parameter to detect vortices from PIV velocity fields, is the swirling strength λ_{ci} or the squared value of it, as defined in §2.2.3. For simplicity we now speak of λ_{ci}, but the following is also valid for $(\lambda_{ci})^2$. A relatively high value of λ_{ci} indicates the presence of a swirling motion. Unlike vorticity, the swirling strength identifies vortex cores only and not any shearing motion present in the flow. If only values of λ_{ci} larger than a chosen threshold value are plotted (peak values) and if it is assumed that the velocities that are used to calculate λ_{ci} are reliable, then λ_{ci} is truly an unambiguous indicator of swirling motion. In fact, according to Christensen & Adrian (2002), λ_{ci} yields patterns that are very similar to the widely-used Hessian of pressure as defined by Jeong & Hussain (1995).

Vortex identification based on swirling strength is frame independent, meaning that an a priori choice of a correct reference frame is not necessary (Adrian *et al*., 2000a). It can be used to pinpoint the core of a vortex of both clockwise as well as counter-clockwise rotating eddies, and subsequently a local Galilean decomposition can be used to verify the vortex existence and visualise the rotating motion. In this way one does not have to subtract a range of convection velocities to reveal the vortices and still be uncertain whether all vortices were detected.

Since λ_{ci} is highly sensitive to deviant vectors, the local Galilean decomposition can be used to check whether the large value of λ_{ci} was really caused by a strong swirling motion or perhaps by the presence of a spurious vector. Another way to decrease the influence of spurious vectors is to first smooth the vectors by means of a two-dimensional Gaussian filter before calculating λ_{ci}. As a final remark about λ_{ci} it is emphasised that whenever Reynolds decomposition is used, λ_{ci} has to be calculated before the decomposition is carried out, for Reynolds decomposition changes the existing velocity gradients and hence λ_{ci}.

*Some interesting features of 2-D velocity vector field*s.
Besides the rotating motions, some other distinctive areas can often be distinguished in the vector fields. Sweeps, for instance, can obviously be recognised as a large area of more or less uniform momentum seen as a zone of downward and streamwise oriented vectors in the non-decomposed velocity fields. In turbulent uniform wall flow one often encounters hairpin vortices and hairpin vortex packets. Although the present flow configuration is far from

uniform, the development of these hairpin vortices and vortex packets may be found downstream of the reattachment point. A hairpin vortex signature (HVS) on a 2-D PIV field consists of rotational clockwise rotating motion (head of the hairpin) and a Q2 event just upstream and closer to the wall of it (caused by ejection of fluid from the area between the steep part of the legs, called neck, of the vortex). Slightly upstream and above the Q2 event a Q4 event can be found, separated from the former by a stagnation point (Adrian *et al*., 2000b). Hairpin vortex packets can be recognised by a sequence of HVSs of which the distance from the wall of each HVS increases with the streamwise direction. All hairpin vortices in a packet move with the same convection velocity, so all the heads of the HVSs show a rotational motion when they are viewed in the same frame of reference. In Adrian *et al*. (2001) a mechanism is shown that may account for the origin of counter-rotating hairpins (i.e. the head rotates counter-clockwise if mean flow is from left to right) in wall flow. They state that two Ω-shaped vortices that are located parallel (next to each other) in the flow connect and that the adjacent legs (the inner legs) form one new counter-rotating hairpin vortex and the outer legs form a larger regular rotating vortex. In these cases a Q4 event can be expected near the counter-rotating vortex, where normally the Q2 event is located.

Some preliminary results of Tromp (2004) indicate a large influence of accelerations in the water on the initial motions of stones in granular bed protections. To determine the influence of accelerations on entrainment in our measurements, it must be known first how accelerations are reflected in a PIV field. Therefore one has to distinguish between temporal and spatial derivatives of the velocities. The accelerations in space can be seen within one vector field, as it is possible to determine whether or not the fluid accelerated in space by looking at the spatial evolution of the vectors. A way to calculate instantaneous time-derivative fields is proposed by Christensen & Adrian (2002), namely to use a first-order, forward differencing scheme that is here given for the x-direction only: $\partial u(x, t)/\partial t \approx (u(x, t + \tau) - u(x, t)) / \tau$. In the present measurements, the time between two successive image pairs τ is probably too large to acquire satisfactory results. Nevertheless, Christensen & Adrian showed that a conditionally averaged velocity time-derivative field, given the presence of a vortex core, displays a strong wall-normal acceleration away from the wall. This acceleration may well be a cause of entrainment of stones from a granular bed. They additionally found a typical mushroom-like pattern in the vicinity of the vortex centre.

2.6 Summary

Since a lot of information was provided in this chapter, it seems useful to summarise it briefly.

First some symbols and a co-ordinate system were introduced, together with some definitions used in turbulence theory. Most of these symbols and expressions are rather common.

Subsequently the swirling strength λ_{ci} was introduced, which is the imaginary part of the complex eigenvalues of the local velocity gradient tensor. The swirling strength can be used to localise vortices in a flow field and resembles the Weiss function, which in turn can be linked to pressures via the Poisson equation for pressures.

In the section that dealt with BFS flow, the main flow mechanisms that occur downstream of a BFS were described in detail. The most eye-catching, two-dimensional flow properties are the presence of a large recirculation bubble between the step and the reattachment point, which is located at 6 a 8 step heights downstream of the step, with a clockwise rotating flow in it and a secondary smaller bubble, occurring in the corner of the step and the bottom, with mean streamlines that show a counter-clockwise pattern. In the shear layer between the main bubble and the upper part of the flow (the free flow), high turbulence intensities are found. The relaxation in the streamwise direction of a flow downstream of a BFS to a uniform equilibrium flow is slow and relatively large turbulence intensities can still be encountered far downstream of the step.

From three-dimensional, instantaneous flow fields it can be seen that the main bubble is subject to an oscillating motion and that the frequency of the oscillation of the reattachment location is 0.6-0.8U_0 / X_R. Also a flapping motion of the shear layer exists which frequency is: $f < 0.1 U_0 / X_R$. Both mechanisms may play a role when it comes to initial motion of stones. Furthermore, several coherent structures with sizes up to the water depth can be discerned from instantaneous flow fields. In general, visualisations show a tendency of the flow to reorientate from a spanwise vorticity field into streamwise vorticity. Upstream of the reattachment point the flow is often already completely three-dimensional. Around the reattachment point CS often impinge on the bottom and either break down or are convected further downstream.

Subsequently the forces on a single stone were described. Of the active forces, the drag and lift force, following the law for the steady drag and lift forces, are the most important ones, while the weight is the main resisting force. For an angular, natural shaped stone, results from a previous experiment showed a drag coefficient of ca. 0.36 and a lift coefficient of about 0.15, provided that the velocity measured at 0.15 d was used. Fluctuations of the velocities near a stone cause the forces on the stone to fluctuate as well and we therefore refer to these forces as quasi-steady forces. These fluctuations play a key role during low-mobility conditions when stones move intermittently with long periods of repose between movements.

Forces on stones in granular beds can also be caused by TWP. These are the result of accelerations of the fluid, which are created, among others, by CS. The CS may be located relatively far away from the bottom wall in order to have effect on the stability of stones. In case the CS is a counter-clockwise rotating vortex, the pressure distribution caused by the vortex and the velocity induced by it can both be such that they contribute positively to the entrainment of stones from bed protections.

Bed protection design methods are generally based on experiments in which the stability (i.e. transport) of coarse bed material under different, uniform flow conditions was determined, like the experiments by Shields (1936). The design approaches for nonuniform flows are commonly based on such uniform design criteria with a correction for the difference in turbulence intensities. Oftentimes this is done by applying a multiplication factor to the longitudinal velocity to account for the peaks in this velocity caused by turbulence. The factor is either estimated or determined by experiments.

A foregoing experiment showed that this correction factor K_v is around 1.25 for a BFS with $H / h_2 \approx 0.345$; in this experiment the K_v-value was probably based on the area where the largest flow attack on the bed could be found. This as well as other experiments also showed that the largest transport of bed material can be expected from slightly downstream of the reattachment point up to 18–20 step heights downstream of the trailing edge of the step. Inside the recirculation bubble negative drag forces were measured and upstream-directed transport of stones was encountered. However, the lift forces (including turbulent fluctuations) remained positive. From yet another experiment it was concluded that downstream of a BFS both Q1 events and Q4 events individually move the same amount of sediment, but that Q4 events collectively move the majority of sediment, because they are very common. Q1 events are effective for the transport of sediment since they tend to move particles up, into the regions with high streamwise velocity. For this reason it might well be that for the transport of stones instead of sediment, they are not effective at all. The same research showed that the most effective sediment transport events shift from Q1 events near the step to Q4 events further downstream. This was explained by the decrease of magnitude of Q1 events by the shrinkage of the influence of the flapping and vortex shedding mechanisms in this direction.

Finally the PIV technique was described, in which the determination of the fluid velocity is based on the measurement of velocities of tracer particles in the flow by illuminating them twice, within a short time interval, by means of a laser sheet and by recording both illuminations with a camera. The velocity vector fields that result from this measurement

technique can be decomposed by means of Galilean or Reynolds decomposition in order to detect underlying structures. Furthermore, vortices can be identified by the use of the local swirling strength λ_{ci}.

The knowledge presented in this chapter enabled us to design an experimental set-up and to decide at which locations in the flow measurements had to take place. The outcome is described in the next chapter.

3 EXPERIMENTAL SET-UP AND PROCEDURE

3.1 Introduction

In this chapter the experimental set-up and procedure are described. The experimental set-up was rather complex, as there were quite some different measuring devices needed. The description of the test facility, the devices involved and the measuring program is rather detailed in order that the reader exactly knows how the experiments were conducted, to avoid misapprehensions or obscurities and so that it is unambiguously known which part of the data analysis concerns which part of the flow. Moreover the high level of detail enables interested persons to reproduce the experiments or to perform additional data analysis.
After a description of the open-channel flume in which the experiments were conducted and the different measuring devices involved, a separate paragraph is dedicated to the section of the flume in which the measurements actually took place. Subsequently, the set-up of the optical devices used to conduct the PIV measurements, viz. the laser, mirrors, lenses and the camera, together with some other tools that were needed to fine tune the PIV recordings, are discussed in the PIV apparatus paragraph. After this, the structure that was used to create a backward-facing step is described, followed by the way in which the data from the several measuring devices was handled and stored. Next, the placement of the granular bed in the flume is explained in detail and the characteristics of the stones that were used to create this bed are given. In the last paragraph an overview can be found of the different locations downstream of the BFS at which measurements were conducted. The accompanying flow conditions are listed as well.

3.2 Open-channel flume and flow control devices

The experiments were conducted in an open-channel flume, which was especially adapted for the PIV-experiments. First the general design of the experimental set-up is described to give a notion of the different parts involved. Next a detailed description of these components is presented.

3.2.1 General features of flume

The flume had a length of a little more than 24 m, a width b of 0.495 m and the sides were ca. 0.54 m high. It was basically a steel frame with sides of glass and a bottom that consisted of a concrete slab, ca. 0.95 m above the floor. In- and outflow structures were present at both ends of the flume. Water was pumped from a basin* at the beginning of the flume through pipes and via a diffuser into the bottom part of the inflow and hence through a streamlined transition into the flume. This made the water enter the flume very calmly. Furthermore a flexible joint between the inflow structure and the flume prevented vibrations from the pump to be transmitted to the flume.

At the end of the flume near the outlet structure there was a sharp-crested, free-discharge, adjustable weir. The water could return in the basin via three pipes leading from the outlet structure back to the basin near the entrance side of the flume. Each pipe could be closed by means of a valve. Flow depths and discharges could be controlled by means of adjustable devices: two valves near the pump, and the above-mentioned weir positioned at the end of the flume. A schematic drawing of the flume and its appurtenances is depicted in Figure 3.1.

The measuring section was located at approximately 14.25 m downstream of the channel entrance and about 9.75 m upstream of the end of the flume. The backward-facing step was

* It was indispensable to have a separated water storage possibility (the basin), in which the water returned after it had been flowing through the flume. If the main water supply system of the laboratory would have been used, the required tracer particles in the water would have disappeared in this large system and new expensive seeding would have to be added to the flow constantly.

created by a wooden structure that was placed directly on the concrete slab, upstream of the measuring area. The bottom area of the flume downstream of it was covered by coarse bed material (stones) to resemble the top layer of a granular bed protection. This area stretched 8.27 m in streamwise direction, beginning directly downstream of the BFS. Since the measuring area could not easily be moved, the wooden structure had to be moved each time a different distance from the BFS to the measuring area was desired. The length of the area covered by stones was kept constant by adding or removing stones at the downstream side of this area each time the position of the step was moved. Two of the three water level meters with which the flume was equipped were also moved each time the position of the step was changed in order to keep their horizontal distances to the step constant. The other water level meter had a fixed position in the flume. An ElectroMagnetic Flow meter (EMF) was used to check if no significant changes in the mean horizontal velocities occurred during an experiment and if no large-scale deviations of the mean flow were present at the times that the target stone moved.

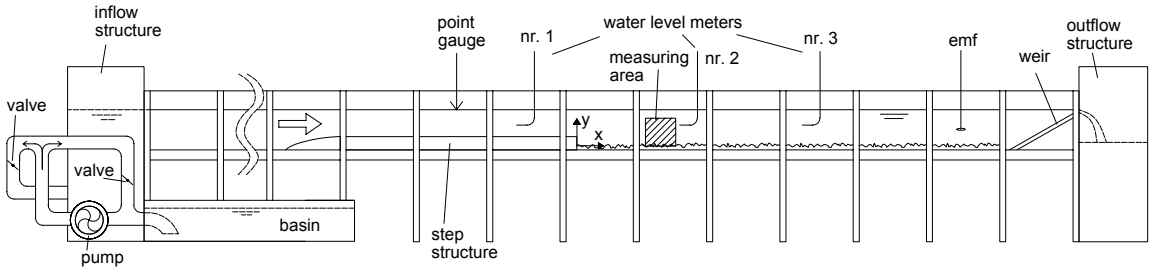

FIGURE 3.1 *Side view of the test facility and flow control devices. For clarity the PIV apparatus and the return pipework are not included in the drawing.*

As stated before and depicted in Figure 3.1 again, the origin of the co-ordinate system that is used throughout this report, is located in the lower step corner. So if the position of the step was moved the co-ordinate system moved along. As a result all reported horizontal positions are always with respect to the location of the BFS.

3.2.2 Control of flow conditions

Pump and weir

The number of revolutions per time of the pump was not adjustable, but the discharge through the channel could be controlled by means of two valves and a shunt: a pipework in which the water could circulate. One valve was located in a pipe that went from the pressure side of the pump back to the suction side of it, another one in a pipe that originated from the first pipe and lead directly to the inlet structure. Both valves could be used to control the discharge in the flume.

The shunt was required to avoid cavitation near the valve that leads towards the inlet structure in case this valve was almost closed or even completely closed. This made small discharges through the flume possible, as was often desired. Moreover, it made fine-tuning of the discharge through the flume possible.

The discharge in the flume not only depended on how the valves were operated, but also on the water depth in the flume (i.e. in the inflow structure). The weir obviously controlled this depth, but it also altered slightly when the position of the step was changed. If the water depth on top of the step structure was kept constant and if it was assumed that the slope of the water surface remained the same, then a change of the position of the step resulted in a change of the water level in the inflow structure. The assumption of a non-changing slope was a

rather legitimate one, as the roughness of the bottom and the roughness of the sides of the flume, which did not change, were the main aspects that affected the slope.

Manometers

To obtain an estimate of the quantity of water that was running through the open-channel flume during the experiments, the discharge through each pipe of the return pipework was determined. Since only stationary flow conditions were examined, the discharge through the closed-conduits was the same as in the flume. Manometers were used that displayed the pressure head difference over each of the return pipes.

Each manometer consisted of two piezometer tubes that were each connected to one of the two apertures that were present in each return pipe. The apertures were 11.01 m apart and located at the bottom of the pipes to avoid air getting into the hoses that connected the piezometer tubes to the pipes. The pressure drop could be read from a water level gauge next to the piezometer tubes. From this difference together with some assumptions (e.g. the roughness of the interior of the pipes, since calibration of the pipes was impossible), the discharge through a pipe could be calculated, see appendix C. The accuracy of the piezometer tubes was a little more than half a centimetre, as the fluctuations of the water levels in the tubes made it impossible to determine these levels more precisely. So the accuracy of a manometer was about 1 cm, as one manometer consisted of two piezometer tubes. The accuracy with respect to the discharge was not known beforehand, as the relationship between the pressure head difference and the discharge was a nonlinear one. Clearly a larger head difference resulted in a smaller read-out percentage. Furthermore, for larger head differences the discharge through a pipe is less susceptible to alterations of the head difference as the graph in appendix C shows. Therefore it was always tried to use a minimum number of return pipes. In spite of this, an uncertainty of about 2 l/s per pipe had to be reckoned with.

Water level meters

Only the length from the trailing edge of the step to the measuring area was allowed to change (by moving the step) during the experiments. All other parameters had to remain constant. In other words: the upstream flow conditions, i.e. depth and discharge, were not allowed to change. Therefore it was very important to know the water depth on top of the step with great accuracy. For this reason a water level meter (nr.1, see Figure 3.1) was placed 50 cm upstream of the trailing edge of the step and was moved along each time the step was moved. The subscript *1*, that was used heretofore to merely indicate that a variable refered to a location somewhere upstream of the BFS, hereinafter indicates that the value belonged to the location exactly 50 cm upstream of the BFS.

As stated before, moving the step also implied a small change in discharge, if the valves near the pump and the weir were in the same position as before the step was moved. So the valves and the weir had to be adjusted until the same upstream depth and discharge were established again. The manometers, however, were not that accurate, so another water level meter (nr. 3, see Figure 3.1) was used at a fixed relative position downstream of the step. If this meter yielded an identical value before and after the displacement of the step too, it was assumed that the flow conditions before and after the shift were equal. The position of this instrument was 5.00 m downstream of the BFS and is from now on indicated by the subscript *3*.

Yet another water level meter (nr. 2, see Figure 3.1) was located at a fixed position, namely 23.2 cm downstream of the centre of the target stone, which in turn had a fixed position in the measuring area. Since this water level meter had a fixed position in the flume, its position with respect to the step altered each time the step was moved, resulting in the variation of the water level as well as the depth as a function of the distance downstream of the BFS. The subscript *2* is used for the location of this water level meter.

The water level meters that have been used were so-called static tubes. The working of a static tube is based on the principle of communicating vessels. Actually the water level in a vertical pipe with a free water surface, which was attached to the side of the flume, was measured (see Figure 3.2). The water level in the pipe was the same as in the flume, due to the fact that the pipe was in communication with the water in the flume by means of a Pitot tube, which penetrated the water in the flume. The apertures in the Pitot tube were located on the top and bottom side of the horizontal part of it to avoid pressures caused by the velocity of the water. A hose connected the tube and the pipe. Since the aperture in the Pitot tube (A_1 in Figure 3.2) was small (diameter of ca. 1 mm), high-frequency fluctuations in the water level that made it hard to determine the water level in the flume by means of a point gauge, did not occur in the pipe. This made the use of such a simple, but rather accurate apparatus as a point gauge possible.

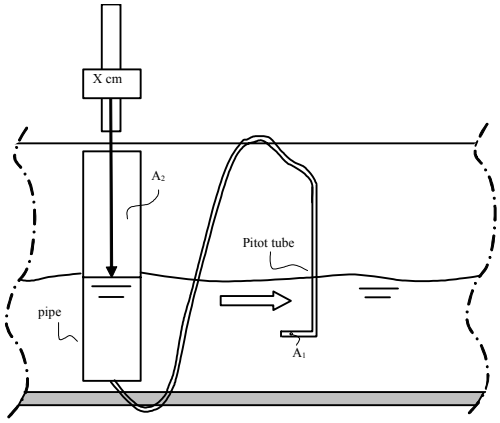

FIGURE 3.2 *Side view of part of flume with water level meter.*

The water level readings from the point gauges needed to be translated into a local water depth in the flume. As the point gauges were all mounted differently and were moved often, no common datum was available, so the depth could not be obtained directly from the readings. For this reason a fourth point gauge, located in the flume itself, was used to determine the water level in the flume when the water was motionless and completely horizontal. At the same time the water levels in the pipes were assessed. For the fourth point gauge, a datum was determined beforehand by taking a reading of a still, horizontal water surface on precisely the same level as lift sensor nr.1 (see section about the measuring area §3.4). Because the water surface was absolutely horizontal, the water levels from the three meters could now be transformed into local water depths with lift sensor nr. 1 as a reference level.

These offset measurements had to be performed every time a new experiment was conducted, so not only if the static tubes were moved. The reason for this being the fact that the pipes, in which the water levels were assessed, were not fastened to the flume really tightly, hence they could move quite easily if someone bumped into them accidentally.

The accuracy of the scale on the point gauges was 0.1 mm. However, this did not necessarily mean that depths could be known with the same accuracy. Although the apertures of the Pitot tube were located on the top and bottom side of the horizontal part of it to avoid pressures caused by the velocity of the water, the curvature of streamlines caused by the BFS resulted in velocity components perpendicular to the apertures. Moreover, undulations that occurred during experiments with Froude numbers above ca. 0.6, created local variations of the water depth. Even if this could result in an inaccurate measurement of the depth, it was not necessarily a problem. As long as the apertures were always at the same spot in the flow, the error was constant too.

For the two water level meters that moved along with the step this could be achieved by letting the Pitot tubes always penetrate the water to the same extent (provided that the flow conditions were equal). For the one that had a fixed position however, this was not possible since its position with respect to the step differed during the course of the experiments. The streamlines near the water surface though, were almost horizontal, even close to the BFS. So by inserting the last-mentioned Pitot tube only a little bit in the water, the error caused by the curvature of the streamlines was limited to a minimum.

The negative influence of undulations on the accuracy could only be overcome by avoiding them. However, to make the target stone move, flow conditions with somewhat higher Froude numbers (> 0.6) were required sometimes. The errors caused by streamline curvature were estimated to be in the order of millimetres. The local variations in water depth as a result of the undulations amounted several centimetres, but only occurred in the vicinity of the step and hence only the readings from water level meter nr.2 were influenced by it.

3.3 PIV apparatus

In this section the components of the test facility that were used to record the velocity fields are described. An explanation of the PIV technique is already given in the second chapter of this report. For a more extensive description we refer to Raffel *et al*. (1998). In this section, merely the optical components of the set-up are specified.

Outline of PIV set-up

The system used (laser and accompanying computer with software to control the laser) was a rather standard system (by LaVision, see appendix D), but to get the desired configuration several components had to be added and adaptations had to be made, resulting in the overall outline of the PIV apparatus as illustrated in Figure 3.3.

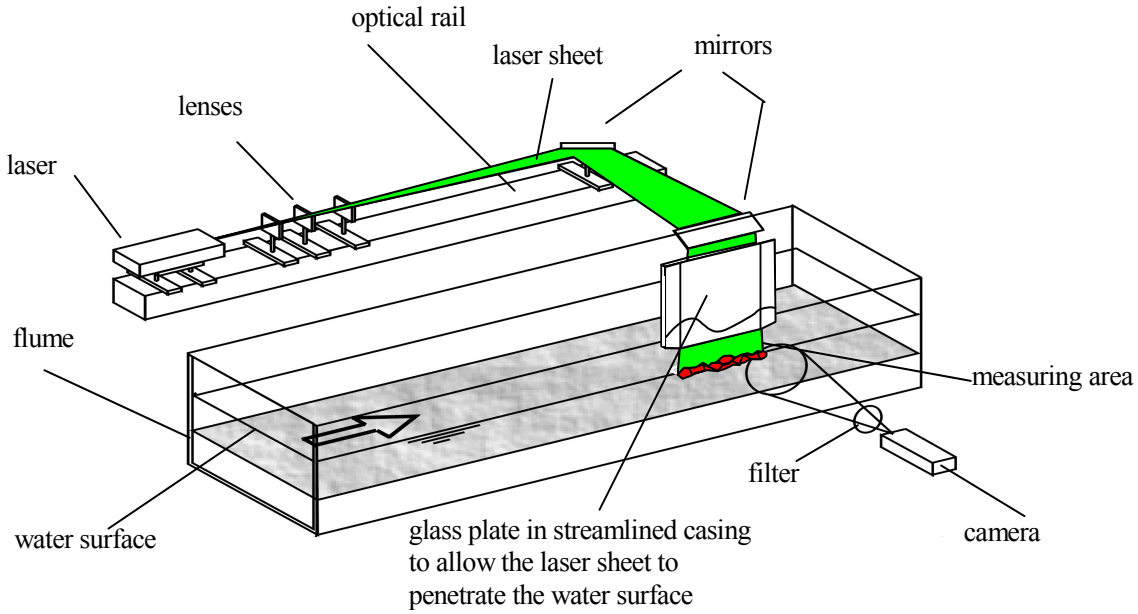

FIGURE 3.3 *Schematic overview of the optical parts of the PIV apparatus.*

After the laser beam had left the housing of the laser, three lenses converted it into a horizontal light sheet of an almost constant thickness of several millimetres. Two mirrors were used to reflect the light sheet towards the centre line of the flume. The light sheet penetrated the water in the flume via a glass plate in a streamlined casing. The glass plate was required to prevent refraction of the light sheet by the unsteady water surface. The stones on the part of the bottom that was illuminated by the laser light were painted red. A filter in front of the camera, capable of reducing the intensity of the large amount of red reflected light, while allowing the green light scattered by the tracer particles to pass, avoided overexposure of the CCD sensor of the digital camera. The measuring area was the area of the water that was illuminated by the laser sheet and in which fluid velocities actually could be measured. This area covered the region of the fluid in the centre line of the flume from the bottom of the flume to the bottom side of the glass plate. It spanned 15 cm x 15 cm and usually covered almost the entire water depth.

By moving the mirrors and the lenses the light sheet could be positioned very accurately. Before each experiment we positioned the light sheet vertically and always at the same spot in the flume. To reduce the thickness of the light sheet to the desired value, a board with a slit (of which the width was adjustable) was placed between the second mirror and the glass plate (not drawn in Figure 3.3, for clarity). The reduction of the width was desired since using too thick a sheet would have decreased the resolution. However, the use of a very thin light sheet would have resulted in much out-of-plane motion of the seeding particles, which is also not desired. Moreover, the slit had to be wide enough to let a sufficient amount of light pass in order to illuminate enough seeding particles. We used a sheet with a thickness of 1.5 mm.

Calibration of camera

Since the main form of data analysis consisted of the inspection of the velocity vector maps, the fidelity of the vectors in the maps had to be high. Therefore a proper calibration of the camera was, among other things, required. The calibration served three purposes, namely: (1) to correct for image distortion caused by the position of the camera not being completely horizontal and perpendicular to the flume and caused by irregularities in the glass side wall, filter and lens; (2) to know the magnification factor from image to reality (which varied within one image), so that the displacements of tracer particles in the images could be translated to real displacements and, together with the known time interval between the two frames of one image, velocities could be calculated; and (3) to specify a point in the image of which both the horizontal and vertical position in the flume were exactly known, so that for each calculated vector the horizontal distance to the BFS and the height above a reference level could be established.

The calibration consisted of taking a picture of a rectangular grid with the camera in the same position as during the experiment and the grid in the centre line of the flume just above the artificial stones. The grid was placed in the water vertically and parallel to the sides of the flume, covering the measuring area. We adjusted until it the horizontal lines of the grid were parallel to the surface of the stagnant water in the flume. Obviously this procedure had to be repeated each time the camera had moved.

Specifications of equipment

Since two powerful, short light pulses were needed within a very brief time interval, a class 4 Nd:YAG laser was used. In fact the laser consisted of two laser rods in one housing and was capable of producing two pulses with a maximum energy of 50 mJ within several microseconds. The maximum repetition frequency of these double pulses was 15 Hz.

We used a digital camera that was able to transfer the raw image data from the CCD sensor (1008 x 1008 pixels) to a second CCD chip behind the first within a few microseconds after the image was recorded. This enabled to use the first CCD sensor for a second recording very briefly after the first one. Only after the data of both images were stored in the camera,

the read-out procedure of the camera took place. The camera enabled to grab double-framed images, required to calculate velocity vectors, with a frequency up to 15 Hz.
The seeding particles had to be small to avoid discrepancies between the fluid motion and the motion of the particles, but had to be large enough to scatter a sufficient amount of laser light. The particles that were used were hollow glass spheres with an average diameter of ca. 11 μm and a density of 1100 kg/m^3 and hence they were more or less in suspension. It took several hours before they had all sunk to the bottom. These tracer particles are commonly used in similar experiments and we assumed that they followed the flow well. The amount of scattered laser light was sufficient to make recordings with a high contrast. More specifications of the measuring devices and the seeding can be found in appendix D.

3.4 Measuring section

The part of the flume in which fluid velocities could be obtained by means of the PIV technique is called the measuring area. As described in the PIV apparatus paragraph, this area covered about 15 cm x 15 cm directly above the target stone in the centre line of the flume. In the first chapter we already mentioned some contrivances we came up with to enable to measure pressures and 2-D velocity fields around a stone that was about to move. In this section these contrivances are described in more detail, as is the related measuring equipment.

First, to fix the position of first stone movement in the bed, we used an artificial stone that was lighter than the real stones that were used to form the granular bed. In fact, we had several of these target stones at our disposal that could be used. Geometrically, the artificial stones were copies of some of the real stones of the granular bed, made with the help of moulds and an epoxy resin. We could vary the density of the epoxy resin by changing the amount of an additive, so the relative submerged density defined as $\Delta = (\rho_s - \rho_w) / \rho_w$, where ρ_s is the density of the mixture of epoxy resin and additive, could be varied as well. The target stone we used the most had a value of Δ of ca. 0.3, a nominal diameter that was more or less the same as the d_{n50} value of the real stones and its Curry shape factor was similar to that of the average value of the real stones (see appendix B).

The natural-shaped, artificial stones were not only used as target stones, but in fact all the stones on the bottom of the flume in the vicinity of the target stone were made of the aforementioned synthetic material. This enabled us to mount pressure transducers in the stones surrounding the target stone.

FIGURE 3.4 *Left: part of flume with the artificial stones (coloured differently) clearly visible. Right: close-up of artificial stones with target stone removed so that the inductive sensor is visible.*

The artificial stones (except the target stone) were glued to a rectangular board (and to each other) in a natural pattern, so that they resembled the configuration of the real stones in the bed, see §3.7. The board, which was about 20 cm by 10 cm (streamwise direction x spanwise direction), could be placed as a whole on a cavity cut away in the bottom of the flume, see Figure 3.4 in which the differently coloured stones are the artificial ones. The cavity was located in the centre line of the flume and underneath it a siphon prevented the water to flow out of the flume. The wires and tubes of the pressure transducers and of the movement sensor went through the hole in the bottom and through the siphon and as a result they did not disturb the flow in any way.

To detect movement of the target stone, an inductive sensor was installed underneath the stone (see Figure 3.4 and Figure 3.5). As the contact between the sensor and the little piece of metal that was glued to the bottom of the target stone was broken for more than 1/500 s, the voltage of the output signal of the sensor changed. From this signal we knew when the target stone had moved and which part of the continuously measured pressure-time-series and which velocity fields were relevant. Besides, the signal of the movement sensor could be used to analyse the statistics of stone movement.

We did not put a loose target stone in the bed, but instead used a small hinge to attach the target stone to a stone downstream of it in order to prevent that the target stone was truly advected by the flow (see Figure 3.5). Instead it could only make a pivoting motion[*] in the streamwise direction until it reached a small rod, designated to limit the pivoting motion to a little less than 90 degrees. After whatever-it-was-that-happened-in-the-flow-that-made-the-stone-move had passed, it fell back to its original position and again the output voltage of the inductive sensor changed. Since after each movement the target stone fell back to the same position, the influence of variations in the shape, exposure and protrusion on the initial motion of the target stone was eliminated (using different target stones enabled to investigate their influences) and the load (the water motion) was the only remaining variable. Besides, the hinge and the rod made it possible to record the flow fields and accompanying pressures of multiple stone movement events without having to replace the target stone manually. In fact, once an experiment had started, recordings were made continuously without any (human) interference until a predetermined number of events was reached and only the relevant parts of the recordings were saved.

[*] Several investigations, including some pilot tests of our own, showed that most of the time the initial motion of coarse bed material is a pivoting one, although sometimes a sliding motion before pivoting is observed.

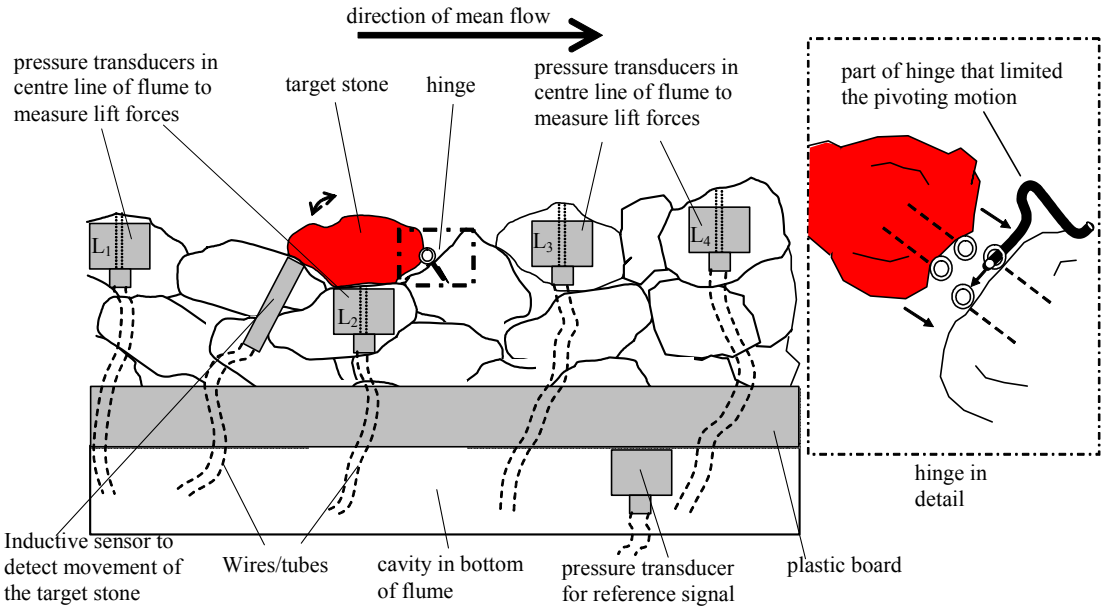

Figure 3.5 *Schematic sketch of the measuring area (longitudinal cross-section) and detailed drawing of hinge. Only the pressure transducers in the centre line of the flume used to measure lift forces ($L_1 - L_4$) are depicted.*

Figure 3.5 is meant to clarify the written text and is not an exact reproduction to scale of the reality (a drawing to scale of the bed profile of the measuring area is depicted in Figure 3.7). It shows that there were four pressure sensors in the centre line of the flume that were used to measure lift forces. One transducer was placed in the stagnant water in the cavity under the board with the artificial stones. The signal from this sensor was used as a reference for the signals from the other ones. Two more sensors were present that were used to measure drag forces. They were not located in the centre line of the flume and are not depicted in Figure 3.5. One of these sensors was located next to the target stone and one a little downstream of it as can be seen in Figure 3.6 (D_1 and D_2 respectively).

FIGURE 3.6 *Close-up of the artificial stones and the visible parts of the built-in measuring devices.*

The sample frequency of the pressures was 500 Hz. The pressure transducers had to be calibrated before or after each experiment. This was done by determining the output voltage of the transducers at two different water levels in the flume and divide the water level difference by the difference in voltage. During both times that the output voltage was registered, the water in the flume had to be completely still. As the relationship between both quantities was linear, a difference in voltage could be converted to a pressure difference. Details about the pressure transducers can be found in appendix D.

Since it was important to know exactly at which positions in the flow the pressures were measured, the bed profile in the centre line of the flume and a profile just off-centre were measured by means of a point gauge. The results are depicted in Figure 3.7.

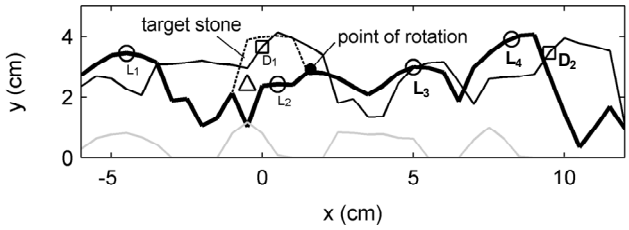

FIGURE 3.7 *Measured longitudinal sections of the granular bed near the target stone indicating positions of pressure sensors (○: upward/lift, □: forward/drag, off-centre) and motion sensor (Δ). Dashed line: target stone. All solid lines represent profiles of the fixed artificial stones. Thick line: centre of flume, thin line: 40 mm off-centre, grey line: board with artificial stones cut in half glued on top of it, y = 0 indicates the top of the board. In this picture the co-ordinate system differs from the one used in the rest of the report.*

3.5 Backward-facing step

The structure used to create a backward-facing step had a length of 5 m, a height of 12.0 cm and the same width as the flume (i.e. 49.5 cm). The required height was estimated using the graph of Figure 2.8 and by using the results of De Gunst (1999). As the structure was placed directly on the concrete bottom of the flume, the height of the stones downstream of it had to be reckoned with. As a structure made out of one piece was not an option, as it had to be moved by hand every time experiments at a new distance downstream of the BFS were desired, the structure was composed of four equally long wooden segments. At the upstream side of the structure, a curved ramp was situated to create a smooth transition from the bottom of the flume to the step (see Figure 3.1). This ramp was also about 1.25 m long. The joints between two adjacent segments (which were max. 2 mm wide) were filled with clay, to make the top as smooth as possible. Between the glass sides of the flume and the segments, a foamy tape was used to fill the gaps that were otherwise there.

The most downstream segment, the one that formed the trailing edge, was fabricated with an overhang. This made it possible to position the step over the plate with cement-bound stones that surrounded the board with artificial stones (see §3.7) and that could not be removed and hence to conduct experiments directly downstream of the BFS. To enable measurements upstream of the BFS, i.e. on top of the wooden structure, the step had to be placed in the laser sheet as depicted in Figure 3.8. Therefore a recess in the trailing edge of the structure was required so that the structure could be placed over the fixed artificial stones. The latter measurements were required, as it was desired to know the velocity distribution of the approaching flow. Foam rubber was used to fill the gap between the overhang and the plate with the cement-bound stones underneath it.

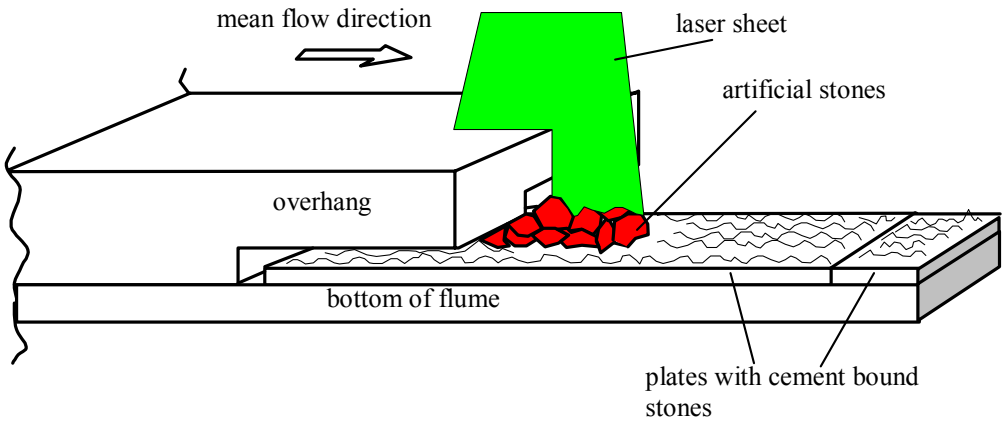

FIGURE 3.8 *Three-dimensional sketch of the BFS whilst placed over the artificial stones. For clarity the genuine stones and the material used to fill the space between the overhang and the plates are omitted. With the wooden structure in this position it was possible to measure the velocities of the approaching flow on top of the step structure.*

The height of the BFS relative to the stones downstream of it, depended on the thickness of the layer of stones and on what was considered to be "the bottom level" of such a granular bed. As a first guess the height of the step with respect these stones, was estimated to be 6 cm (see §3.7.2). It was desired to have an estimation of the step height, for the positions of relevant flow phenomena downstream of a BFS are generally expressed in a number of step heights.

3.6 Data acquisition

During each experiment a lot of data had to be collected, of which some simultaneously. A distinction can be made between the devices of which the gathered data was stored automatically with the use of PCs and the equipment of which the readings had to be done manually. The pressure transducers, the EMF, PIV apparatus and the movement sensor were part of the first category, while the manometers, water level meters and the point gauge in the flume belonged to the second group.

Electrical equipment

The data from the first category were stored at two different computers. To operate the PIV system and for the storage of the data obtained by this system, a PC with a dual Pentium III processor, 1 GB of RAM and a hard disc with a storage capacity of ca. 75 Gb, was used. Moreover, this PC was equipped with a special timing unit to control and synchronise the laser and the digital camera. The software package that was used for this and for the postprocessing of the raw images, was DaVis 6.2.2 (by LaVision).

A standard PC and an in-house program (DASYLab) were used for the other electrical measuring equipment. A multi-channel device enabled us to connect the different measuring devices to this computer. Alltogether there were eight recording channels of which four were used for the pressure transducers (including one for the reference signal)[*], two for the horizontal components of the flow velocities measured by the EMF, one for the inductive

[*] Although alltogether there were six built-in pressure transducers (four lift and two drag sensors), only three of them could be used simultaneously. This was due to the fact that there were only four amplifiers available, of which one was permanently in use for the reference sensor.

sensor, and the last channel was used for a signal from the PIV computer that indicated the status of this latter PC. A self-made flow chart in DASYLab organised the different input signals, ensured that the data were synchronised before storage and assured that only the relevant parts of the data (i.e. around the points of stone movement) were saved by using the signal of the sensor that indicated movement of the target stone as a trigger.

Despite the sensor that indicated movement of the target stone, a continuous recording of velocities and pressures was required. As we were interested in the water motion and accompanying pressures that caused movement of the target stone, the signal from the sensor arrived too late to act as a trigger for the beginning of the recordings, for by then the largest part of the phenomena responsible for movement had already passed. However, since there was only a limited storage capacity that was fast enough to save the digital images of the camera (RAM of PIV computer), a continuous saving of these recordings was not possible. Instead the RAM was used to temporarily store the images in a ring buffer of a limited capacity (see Figure 3.9). If this buffer was full the latest recording replaced the oldest one until the target stone moved. When the inductive sensor indicated stone movement, the recordings continued for a few more seconds, so that the flow structures that were upstream of the target stone when it moved were also recorded, and then the images in the buffer were saved to the hard disc of the PC. So the signal from the movement sensor was used as a trigger to start saving the temporarily stored recordings to the hard disc and not as a trigger to start recording images.

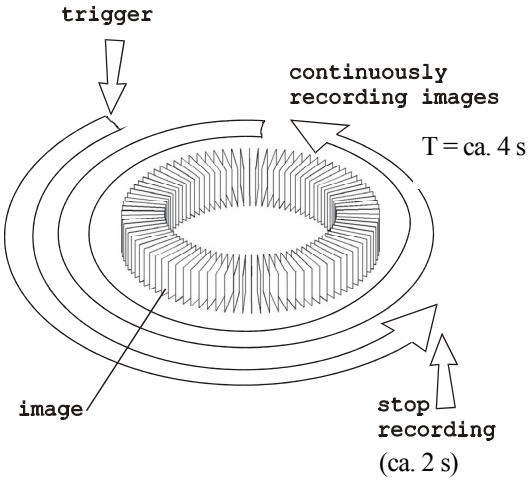

FIGURE 3.9 *Visualisation of temporarily storage of images in RAM.*

A script written in the command language of Davis allowed us to set the total number of images that had to be saved each time the target stone moved. The capacity of the RAM used for the temporary storage of the images restricted the maximum number of double-frame images to 300. The script enabled us to set how many recordings preceding the first movement of the target stone should be saved and how many following this movement. Since the sample frequency of the recording of the images was known for each experiment, the recorded time span (both before and after stone movement) was known as well.

Before the output signals of the pressure transducers were saved, they were amplified and subsequently filtered. Of the pressure time series also only the time spans around stone movements were saved. To save only these relevant parts, an option available in DASYLab could be used. Of all signals only the ones from the inductive sensor and the EMF were saved continuously.

Manually operated equipment
The readings from the devices that had to be operated by hand were registered in writing in pre-printed tables. These readings were all related to flow conditions (water depths and discharges). Since identical flow conditions were oftentimes desired for different experiments, offset readings had to be made in advance. Besides, the settings of the flow control equipment (the height of the weir and the position of valves) had to be jotted down as well to enable to re-establish the same flow conditions. Moreover, the horizontal distances between the equipment and the step structure and the distance from the target stone to the BFS had to be measured and either adjusted or registered.

3.7 Granular bed

Only the top layer of a granular filter was placed in the flume. If the stones that were used to create such a layer were placed directly on the bottom of the flume, an abrupt change in porosity would occur. Since the bottom of the flume was made of concrete (flat) and the shapes of the stones were irregular, there would be little contact between the stones and the bottom, resulting in a nearly hundred percent porosity near the bottom while in reality their would be a second filter layer or, if none, the sandy bottom of e.g. a river would allow the stones to penetrate this bottom to some extent. To avoid the abrupt change in porosity, plates were placed on the bottom of the flume, made of reinforced cement, in which stones had been placed in a regular pattern in a way that the stones covered 60% of the cement surface and their summits protruded above the cement. These plates were present from the step structure to somewhat more than 8 m downstream of it. The percentage of 60% was chosen since the percentage of voids in the bed material we used was approximately 40%. (In appendix E the way in which the plates with the cement-bound stones were fabricated is explained, in appendix B one can find how the porosity was obtained.) On top of the plates the top layer of loose stones was placed. Before the experiments, this layer was exposed to hydraulic loads to obtain a water-worked bed.

3.7.1 Stones

More information of the characteristics of the stones that were used during the experiments can be found in appendix B. Only the main characteristics are listed here.

TABLE 3.1 *Characteristics of the stones used in the experiments based on a sample of 240 stones*.

d_{n50} (cm)	d_{n85} / d_{n15}	Mean curry shape factor S_f	Mean relative submerged density Δ
1.78	1.27	0.56	1.70

The stones of which the characteristics are given in Table 3.1 were used for both the cement plates and the top layer of loose stones and were chosen because they were large enough to mount pressure transducers inside them and sufficiently small to fulfil the dimension related requirements from the first chapter (e.g. to be smaller than 1/5 of the water depth). Besides, they were rather angular (broken stones) and their shape resembled the shape of stones that are generally used for bed protections. Moreover, a rather large number of them were in stock in the laboratory.

3.7.2 Top layer

To resemble reality, a layer of loose stones was placed on top of the plates with the cement-bound stones. After it was exposed to hydraulic loads the total thickness of the loose stones

and plates together was determined. By thickness we mean the distance from 0.2 times d_{n50} below the highest peaks of the loose stones, to the plate with cement-bound stones underneath them. For densely packed spheres 0.2 times d_{n50} below the highest peaks, is considered to be "the bed level".

Before and after exposure two longitudinal bed profiles were measured at the half-width of the flume; one upstream and one downstream of the measuring area. This was done to see if the bed was really water-worked and to know how the artificial stones in the measuring area had to be placed to resemble the real layer of stones and to have the same average protrusion.

Placing the top layer

In literature dealing with experiments on the stability of stones in a granular bed, one often finds a thickness of the bed of around two times d_{n50}. In this experiment a constant thickness of the layer was considered to be of more importance then the thickness itself. For this reason it was made sure that the same weight of stones, namely 21.68 kg, was placed per metre of the flume. These values seemed to yield a satisfactory layer thickness (i.e. ca. two times d_{n50}), as judged by eye.

A wooden frame was set in the flume on top of the plates with the cement-bound stones and a bucket with the correct number of stones was emptied into the frame. After the bed was smoothened by hand, based on visual inspection, the frame was moved to the adjacent part of the flume. This procedure was repeated until a layer of loose stones covered all the plates.

Exposing the bed to hydraulic loads

Subsequently the granular bed was exposed to a flow which was just strong enough to move some stones. In this way the bed was altered a little, because stones that were oriented or positioned in a highly unlikely way, that would not occur in a water-worked bed, were moved. The most protruding stones moved to locations where they were more sheltered; pockets were filled by the formerly exposed stones. A too severe attack was not desired because this would really damage the bed.

As the required flow velocity to accomplish the intermittently shifting and rotating of stones was rather high, it could not be done by simply starting the pump and run water through the flume. Moreover, then the attack on the bottom would not be the same throughout the flume, for the bottom friction would cause a slope in the free water surface, resulting in a decrease of the water depth in the flow direction. Therefore a wooden frame was suspended in the flume. Underneath the frame perpendicular to the flow direction, a pipe with a diameter of circa 16 cm was attached over the full width of the flume so as to form a vertical constriction. The water was now forced to flow under the pipe. The flow contraction with its higher velocities, and also the extra turbulence behind the pipe, increased the attack on the bottom under and just behind the pipe. The distance between the bottom and the lowest part of the pipe was adjustable, so that it was possible to create the desired flow: a flow that caused the stones to move every now and then. The pipe was kept in the same position for 20 seconds and then it was moved horizontally in the flow direction over a distance of 3 cm and kept there for 20 seconds again. This was repeated over the entire length of the granular bed.

Thickness

At two sections, each about one meter in length, one upstream (section 1) and one downstream (section 2) of the measuring area, the vertical positions of the stones in the centre of the flume, before and after they were exposed to the above-mentioned hydraulic loads, were determined by means of a point gauge (manually). The results of these measurements are shown in Figure 3.10.

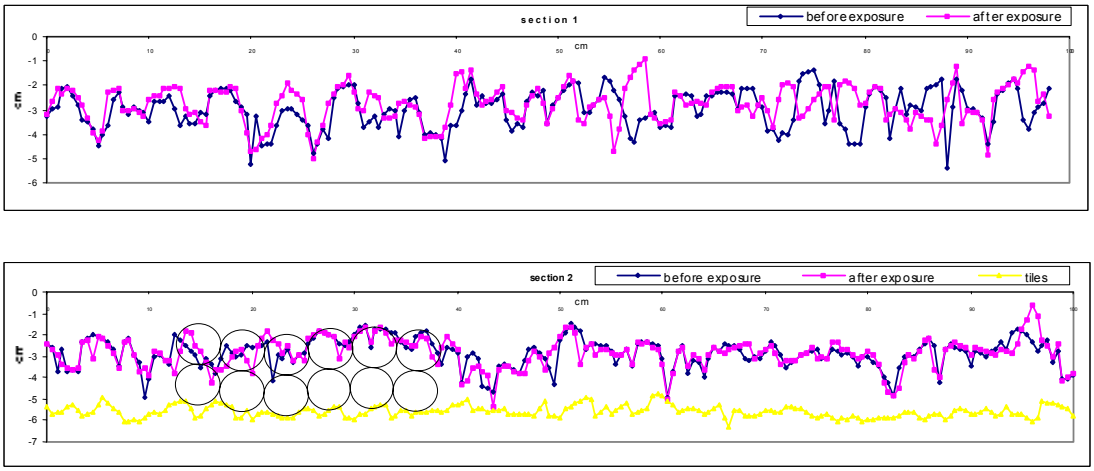

FIGURE 3.10 *Bed profiles before and after being exposed to hydraulic loads. Upper plot: section 1 upstream of measuring area. Bottom plot: section 2 downstream of measuring area. In the bottom plot the profile of the plate with cement-bound stones is included to visualise the thickness of the layer of loose stones (the circles have a diameter that equals d_{n50}).*

As one can see, the profiles of the non-exposed and the exposed bed are only slightly different, as was the purpose of exposing the bed to the hydraulic loads. For section 2, the profile of the plate with the cement-bound stones underneath the layer of loose stones is also shown, so the thickness of the layer of loose stones after being exposed to the hydraulic loads can be obtained from this. It is approximately 1.54 times d_{n50}, marked by the circles, which have a diameter that equals d_{n50}.

For the design of the step structure the thickness of the plates with the cement-bound stones also had to be known, for the structure was placed directly on the bottom of the flume. The total thickness (plates + loose stones) was determined by measuring the water depth in the flume in a spot with no cement plates, while the water was completely still and horizontal and the water surface at such a level that it was just protruded by the highest stones only (see Figure 3.11). In fact it was tried to get the water level about 0.2 times d_{n50} below the highest peaks of the stones. The thickness of stones and plates together turned out to be 5.96 cm (10.43-4.47, see Figure 3.11).

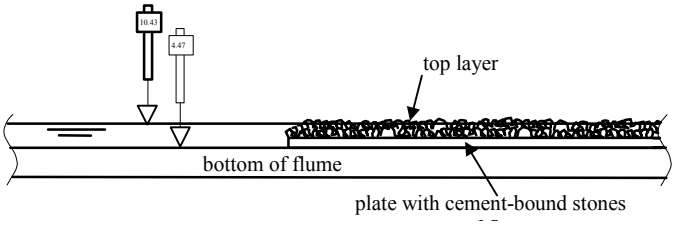

FIGURE 3.11 *Determining the total thickness of layer of loose stones and plates with cement-bound stones.*

3.8 Overview of conducted experiments

In this paragraph an overview of the experiments conducted and the accompanying flow conditions are given. Before water depths could be determined from the water level readings, the level that would be considered as “the bed level” and at which we chose to locate the

vertical position of the origin of the co-ordinate system (the level $y = 0$) had to be known. In the previous section we chose the level about 0.2 times d_{n50} below the highest peaks of the stones as the reference level. We could not use this level as a reference level for the velocity measurements, as we did not know where it was located on the PIV images; it simply served to design the height of the structure that was used to create the BFS. Furthermore, once the results of the uniform flow experiments were available we could determine the level $y = 0$ from the mean longitudinal velocity profiles of these experiments (see appendix F) and use this level, which is more befitting for granular bed material, as the bottom level*. The result of this method is a bottom level that was located 2.5 mm below lift sensor 1. In Figure 3.7 one can see that this level is below the summits of the stones in the granular bed. As the bottom level was now known, the water levels that were obtained could be translated to water depths.

We used two methods to determine the step height: (1) by putting the needle of the fixed point gauge (see Figure 3.1) on top of the step structure each time it had been moved and (2) by measuring the vertical distance from the reference level (y = 0) to the top of the step structure by means of a vernier calipper rule while the step structure was placed in the measuring area (as during experiment B010, see Figure 3.12). Since neither the bottom of the flume nor the bottom of the step structure were completely horizontal, (1) yielded a range of heights with a maximum difference of 3.5 mm. Besides, when the point gauge was close to the trailing edge of the step structure, the structure itself was relatively far from the measuring area and vice versa. Therefore we chose to use the height obtained by (2) which was accurate for the experiment during which the step structure was close to the measuring area and which was 3 mm larger than the average of (1), but we beard in mind that the step height might have been somewhat less when positioned somewhere else in the flume. This choice yielded a step height H of 6.7 cm, resulting in an aspect ratio (b / H) of 7.4.

3.8.1 Locations of measuring area

The positions of the measuring area with respect to the BFS during the different experiments are displayed in Figure 3.12. The experiments are denoted by B001 – B010.

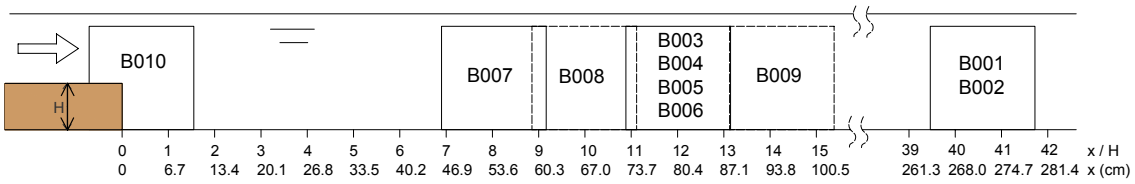

FIGURE 3.12 *Overview of locations of measuring area.*

During the experiments B006 through B010, flow conditions were more or less identical (see Table 3.2). The measuring areas of these experiments overlapped so that despite the lesser quality of the margins of the PIV recordings, the complete course of the velocities (u and v) as a function of the horizontal co-ordinate could be established, without gaps between the measuring areas. Besides, the overlaps enabled verification whether the flow conditions were indeed identical during two experiments of which the measuring areas were adjacent, as was the aim.

* Since the reference level obtained by the results of the uniform flow experiments was not yet available when the step structure was designed, it could not be used to determine the height of this structure.

3.8.2 Flow conditions

Even though an aspect ratio larger than 10 has been recommended by some investigators to avoid significant sidewall effects in the vicinity of the centre line of the test section, it was assumed that in the current experiments the influence of the glass side walls of the flume on the flow would be small if a maximum water depth of three times the width of the flume was chosen. This seemed a justifiable assumption, because the bottom wall was very rough and the sidewalls were relatively smooth. Hence, although the water depth in the flume could vary between 0.05 m and 0.25 m, it was tried to limit the water depth to a maximum of ca. 0.16 m.

On the other hand, the discharge had to be increased until the flow caused the target stone to move, resulting in unwanted rather large Froude numbers if the water depth had to remain below a certain value. Whereas at first it seemed that these conflicting requirements could not be met simultaneously, in the end it turned out that with flow conditions as during the experiments B006 & B009, as listed in the table below, it could after all.

Moreover, altering the discharge brought about that the position of the target stone with respect to the occurring flow phenomena changed. Besides, if certain flow conditions made the target stone move, then the same flow did not necessarily make it move when the distance between step and target stone changed. However, experiments under the same flow conditions but with a changing distance from the target stone to the BFS during which movement of the target stone occurred, were desired. An additional difficulty was the desired low-mobility condition, which required a long time before one could tell whether established flow conditions were able to make the target stone move. It was not until after some experiments that the right distances from the step and satisfying flow conditions were found.

TABLE 3.2 *Overview of experiments. Reminder: subscript 1 = 50 cm upstream of BFS, subscript 2 = 23 cm downstream of target stone and subscript 3 = 500 cm downstream of BFS.*[*]

Experiment ID	x (cm)	Discharge ± 2 (l/s)	h_1 ± 0.02 (cm)	U_1 (m/s)	Fr_1	h_3 / h_1	H / h_3	Mobility	*Re* based on water depth
B001	270.4	34.6	8.60	0.81	0.88	1.72	0.45	0	69883
B002	270.4	38.3	11.32	0.68	0.65	1.61	0.37	0	77446
B003	80.5	41.9	18.46	0.46	0.34	0.73	0.50	?	84697
B004	80.5	44.9	13.68	0.66	0.57	1.39	0.35	low	90699
B005	80.5	40.5	12.96	0.63	0.56	1.42	0.37	?	81834
B006	80.5	33.4	11.60	0.58	0.55	1.53	0.38	low	67509
B007	53.8	33.4	11.16	0.60	0.58	1.59	0.38	0	67493
B008	66.9	32.8	11.57	0.57	0.54	1.54	0.37	0	66281
B009	95.5	33.2	11.35	0.59	0.56	1.57	0.38	low	67051
B010	3.1	31.8	10.79	0.59	0.58	1.63	0.38	0	64178

The values in the second column denote the horizontal distance x from the centre of the target stone to the BFS. In the columns 3 to 9 some flow conditions are listed. The water levels were obtained with an accuracy of ± 0.02 cm, but the accuracy of the water depth on top of the step structure (h_1) was less due to the uncertainty in the step height. Since we chose a level $y = 0$, the water depths downstream of the step with respect to this level were known with the same accuracy as the level itself. In the last but one column the mobility of the target stone is given. A zero (0) indicates that no stone movement occurred. This could be caused by the hinge that did not allow movements of the target stone in the negative x-direction (in the recirculation region) or by flow conditions that were too weak. The Reynolds numbers listed in the last column are based on the water depth. Since the discharge ($Q = Uhb$) and the width of the

[*] During all experiments (save experiment B005) the same artificial stone was used. This stone had a nominal diameter that was more or less the same as the d_{n50} value of the real stones and its Curry shape factor was similar to that of the average value of the real stones (see appendix B). The relative submerged density of this stone was 0.3.

flume (b) are independent of the horizontal position in the flume, Uh is constant throughout the flume. Therefore the Reynolds numbers based on the average flow velocity and water depth ($Re = Uh / \nu$) upstream, downstream and on top of the step structure are the same.

The experiments are numbered in the same order as they were conducted. From Table 3.2 it can be seen that there are five tests with the same flow conditions (B006 – B010), all conducted at different locations in the flow. During B006 stone movement with a probability of occurrence corresponding to low-mobility transport occurred under satisfying flow conditions. The first five tests (B001 – B005) preceded B006 and were needed to arrive at these satisfying conditions. After B006 we searched for other locations at which movement of the target stone occurred under the same flow conditions. This proved to be the location at which B009 was conducted. It turned out that the locations of B007 & B008 were still too close to the BFS for movement of the target stone in the positive x-direction to take place. B010 was conducted to obtain the velocities of the approaching flow at the established flow conditions.

Of the tests that preceded the ones with identical flow conditions, B003 – B005 were conducted at the same location as B006, but with different flow conditions. Experiment B005 was conducted with a different target stone as well. Tests B001 & B002 were conducted at the same location relatively far downstream of the step. No trigger signal was available during these last two tests.

In a nutshell: two experiments were conducted with more or less the same flow conditions, but at different locations in the flow, during which the target stone moved according to low-mobility transport conditions. These experiments are B006 and B009. During these experiments velocities were measured over (almost) the entire water depth with the largest possible temporal resolution.

3.8.3 Settings of measuring equipment

There were a lot of parameters and settings of which the values could differ for each experiment. Only the parameters and settings that were the same throughout all the experiments are given below.

Sample frequencies

The sample frequency of the pressure measurements was set to 500 Hz. The same frequency was used for the inductive sensor, meaning that the sensor was capable of detecting all stone movements for which the contact between the piece of metal under the target stone and the sensor was broken for more than 1 / 500 s. As the signal from the EMF had to be registered and saved continuously to check if irregularities were present at the points of time at which the target stone moved, its sample frequency was much lower, namely 1 Hz. These sample rates were the same throughout the whole measuring program.

Three kinds of PIV recordings were made during the experiments. The first recordings consisted of the series of images around the movements of the target stone. These recordings were made with the maximum possible sample rate, viz. 15 Hz. A sample frequency of 15 Hz implied that every 0.067 s a velocity field was obtained. A typical value of the number of images per event was 55, so around each event a time span of 3.7 s was covered. The vector fields calculated from these recordings were used to inspect the velocity fields around the target stone during entrainment and to make conditionally averaged vector fields.

The second series of images were made while the target stone was secured to the bed, so it could not move at all, with a sampling frequency of 0.5 Hz for 10 minutes (300 images). Since no stone movement occurred during these recordings and because the time span was long with respect to the characteristic time scale of the turbulent motions, the vector fields

from these recordings were well suited for calculating average values of the velocity components.
The third and last series were also made with a target stone that could not move, but this time with a sample frequency of 15 Hz. The maximum of 300 images now resulted in a duration of the measurement of 20 s. The vector fields computed from these series were, among other things, used to investigate if quasi-periodic mechanisms were present.

Trigger settings
In the script used to set the total number of images that had to be saved each time the target stone moved we could also set how long the contact between the target stone and the inductive sensor had to be broken before the signal from the sensor was used as a trigger for the read-out procedure of the ring buffer. In this manner it was tried to avoid to save the recordings of merely rocking of the target stone, which is of less interest than real movement (pivoting around axis of hinge). During most experiments, this time was set to at least 2 images (= 0.13s). Some trial tests showed that a stricter criterion (i.e. stone had to be up longer, as was the case during the uniform experiments) would hardly have resulted in any events. These tests also showed that most of the time the target stone was all the way up and back in its pocket again in just a few images. As the signal from the sensor was registered continuously, all stone movements were registered and not only the ones that fulfilled the requirements formulated above.

3.8.4 Selection of experiments for analysing

As the flow conditions during experiments B006 – B010 were approximately the same, we focus hereinafter on the experiments B006 – B010. As can be seen in Table 3.2 the ratio H / h_3 of these experiments is in the same order of magnitude as the ones by Nakagawa & Nezu (1987) and De Gunst (1999), who both conducted experiments with H / $h_3 \approx 0.35$, what enabled us to compare our results with theirs. During B006 & B009 movement of the target stone occurred. Due to time limitations we choose to analyse only one of them, namely B006.

4 DATA PROCESSING

4.1 Introduction

The experiments resulted in large amounts of (raw) data, therefore a proper way of archiving them and the use of protocols how to process the data was of utmost importance. The data processing methods that were used are explained in this chapter. The different measured quantities are treated separately, for most of them are obtained from different measuring devices.

Due to time limitations and because it was reasonable to expect that the PIV measurements could give more insight in the cause of entrainment than the measured pressures, most attention was paid to the PIV measurements (of experiment B006). It is explained how velocity maps were calculated from the raw images obtained by PIV, followed by an explanation of the different techniques we used to interpret these vector fields. However, before the raw images could be converted into velocity maps, the stone movements events during which a pivoting motion of the target stone was visible needed to be discriminated from the ones during which a mere rocking motion was present, and it had to be checked if the movements were not provoked by external influences.

In the next chapter the processed data are analysed and interpreted.

4.2 Determining the stone movement events

As already explained, the points in time at which stone movements of the target stone (events) occurred could be derived from the signal of the inductive sensor. This signal indicated whether the target stone was in its original position or lifted up, and was used as a trigger for the readout operation of the ring buffer. As mentioned before in §3.8.3, the requirement for saving the PIV recordings consisted of a minimum time for which the contact between the sensor and the target stone had to be broken, so a first distinction was made between rocking events and events during which the target stone made a pivoting motion. Still, the saved events needed to be subjected to a visual inspection to filter out all the rocking events. Only the events for which the target stone pivoted more than ca. 60 degrees around the axis of the hinge were selected and considered to be real stone movements (movements for which the target stone would have rolled away if there would have been no hinge).The distinction between moving and rocking was harder to make than in case of uniform flow.

Sometimes an event was only partially recorded or not recorded at all. This was the case when a new event occurred while the computer was still busy saving the data of the previous event or when a new event occurred while the ring buffer was not yet completely full. These events were nonetheless present in the registration of the movement sensor and from this it could be deduced that, fortunately, they hardly ever occurred.

In Table 4.1 it is shown how the number of approved events was reduced by both the minimum-time-up criterion and the visual inspection. The duration of an experiment and the average entrainment (mobility), based on the events that remained after the visual inspection, are listed as well.

TABLE 4.1 *Selection of the events.*

Exp.	Total # of events	# of events fulfilling the minimum-time-up criterion	# of events after visual inspection	Duration of exp. (hours)	Mean movement frequency (events/hour)
B006	65	36	8	9.6	0.83

The number of events that can be found in the fifth column is the final number of events that resulted from the selection. Mainly these selected events were used in the search for the cause of entrainment of stones from a granular bed downstream of a BFS. As can be seen in the last column, the established flow conditions yielded a (very) low frequency of stone movement, corresponding to the desired low-mobility conditions.

The visual inspection learned that the first image at which the continuous upward displacement of the target stone (pivoting) was observable was sometimes not the same as the frame at which the very first stone displacement could be discerned (rocking before pivoting). The first image at which the pivoting motion was observable was used as the reference frame for synchronising the different events (this was e.g. required for the construction of conditionally averaged images, see §4.5.2).

4.3 Check of flow conditions by Electro Magnetic Flow meter

Once the times at which the events took place were known it could be checked whether the signal from the EMF showed some large-scale irregularities at these points of time. It could e.g. be possible that fluctuations in the power supply of the electricity network caused the pump to alter the discharge slightly or that a long wave oscillated in the flume. This check was relevant, as the flow conditions were often such that the smallest change in e.g. the discharge resulted in a significant change of the mean entrainment.

Since the EMF was located relatively far downstream of the measuring area, the presence of a structure that made the target stone move might only have been observable in the signal from the EMF if it was a large-scale structure. In Figure 4.2 both horizontal velocity components that were measured by the EMF are displayed for one event of experiment B006.

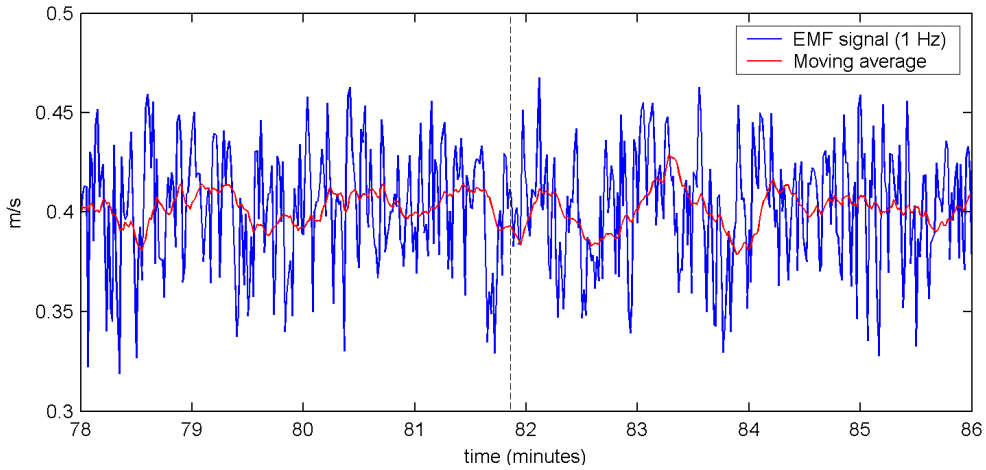

FIGURE 4.1 *EMF signal (u-velocity) around the time at which the first approved stone movement of B006 occurred. The instant of the event is indicated by the dashed vertical line.*

A mode with a period of a little less than 1 min. seems to be present in this example, but the event does not coincide with a maximum of it. Of course this check was performed for all approved events and it turned out that none of the events seemed to be brought about by unwanted large-scale deviations of the mean flow velocities.

In addition, for each experiment it had to be checked if the mean flow velocities were constant during the whole time span of an experiment. For experiment B006, this is visualised in Figure 4.2.

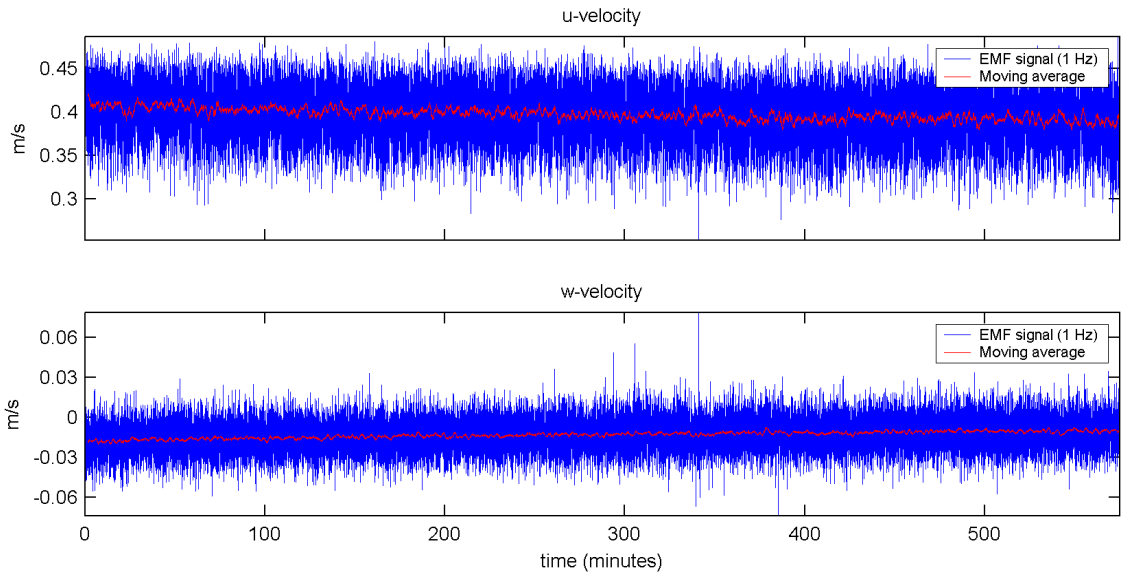

FIGURE 4.2 *EMF measurements of experiment B006, u and v velocity components.*

Both signals show a clear drift in the course of time as can be seen from the slope of the lines that depict the moving averages. Nonetheless, we presumed that, since the time intervals between events (i.e. all the events, not only the selected ones) did not decrease in the course of time and since EMFs are known to display this kind of behaviour, the drift was probably caused by the EMF itself and not by a slow change of the mean flow velocities. The combination of electrodes and electronics, and the fact that the EMF becomes filthy after a while, make an EMF susceptible to electronic noise and zero-offset drift.

4.4 Pressures

All four signals from the pressure transducers were low-pass filtered by means of analogue filter devices before they were saved digitally with a cut-off frequency of 240 Hz. As this frequency was a little less than half of the sample frequency, which was 500 Hz, aliasing by digitization was avoided.

The advantage of the use of analogue filters instead of digital ones was that there was no need to digitize the signal before filtering. The conversion from analogue to digital would have caused a time delay, which would have complicated the synchronisation of the pressure signals and the PIV recordings.

As time restrictions did not allow investigation of the pressure signals in-depth, we shall pay no further attention to the way these signals were processed.

4.5 Particle image velocimetry

It is not known (yet) which phenomena are responsible for the dislodging of stones from a bed downstream of a BFS. Not even the scales of the phenomena are known. Maybe relatively large-scale, long lasting fluid packets with high momentum (sweeps) are responsible or perhaps it are local, briefly existing vortices in the vicinity of the stones of a granular bed that cause damage to the bed. Anyhow, we had to search for the cause of entrainment within a range of scales and therefore had to make sure that this whole range could be resolved from the measurements.

To what extent we could reveal details of the flow was determined by the spatial resolution of the measurements. This depended on the values of some parameters that were used to compute vectors from the tracer particle images. To judge if structures larger than the measuring area played a role in the entrainment process we used a technique based on Taylor's hypothesis (frozen turbulence) which we called "splicing".

In fact splicing is one of several visualisation techniques we used to reflect the large amounts of data in an orderly manner. The way of presenting the data was especially important for this research, for to reproduce a range of rather long time series of velocity fields on paper is burdensome. Moreover, it turned out that printing complete vector fields on A4 size paper yielded unclear pictures. During the analysis we used for instance movies of vector fields, swirling strength, divergence etc. to gain insight in the structures responsible for entrainment in a qualitative way. Unfortunately it is hard to reproduce that information in writing or in the form of graphs. There are some visualisation techniques, however, that helped to partially overcome this inconvenience. Moreover, they served to quantify the characteristics of the flow structures and to discriminate between different possible causes of entrainment. These techniques are introduced in the following paragraphs.

4.5.1 Calculation of vector fields

Velocities had to be calculated from the raw images, as recorded during the experiments. To arrive at the final vector plots, which could be further analysed, a sequence of steps had to be performed. First an overview of the different steps in the sequence is given and subsequently some of the parameters used to compute the vectors are elucidated.

Sequence of the different stages of the vector computation procedure

The vector computation procedure consisted of several steps: image preprocessing, the vector computation itself, pre-postprocessing of the vectors and postprocessing of the vectors.

First a mask was applied to the raw images in DaVis to exclude areas from the vector calculation procedure. These areas consisted of the stones that were visible on the images and the sides of the images where the illuminating of the seeding particles was sometimes not sufficient to calculate reliable vectors.

After the images were corrected for distortion, the vectors could be calculated. A lot of variable parameters influenced this calculation. The values of these parameters, of which the most important ones are discussed in this paragraph, were a compromise between the amount of vectors that resulted from the calculation and the reliability of the vectors.

The reliability of the vectors could be improved by postprocessing. Most of the post-processing was aimed at rejecting vectors that were spurious. The main tool used for this was a so-called median filter.

After the postprocessing the vector plots were of such quality that they could be used for analysis. All of the above was done by means of the DaVis software package. Although this package offered dozens of visualisation techniques, we also imported the vector fields in the well-known software package Matlab to enable some additional operations (e.g. splicing and conditional averaging (see §4.5.4 & §4.5.2).

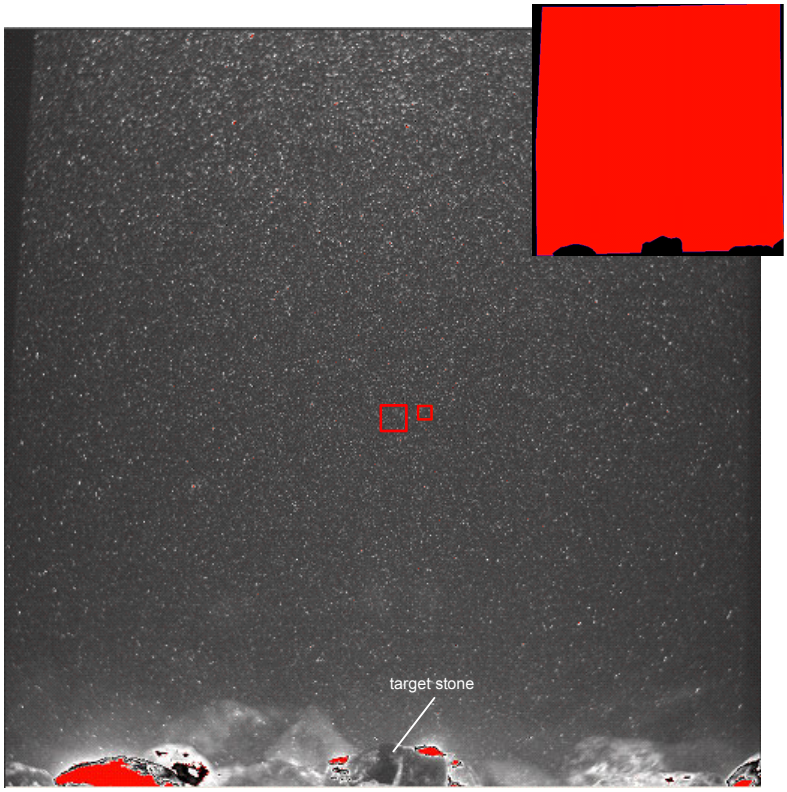

FIGURE 4.3 *Example of a raw image with the seeding particles and the stones on the bottom of the flume clearly visible. The two small rectangles in the centre are interrogation windows with sizes of 32 x 32 pixels and 16 x 16 pixels. The image in the upper right corner shows the mask used.*

Vector calculation and postprocessing

An example of an image as obtained from the PIV measurements is given in Figure 4.3. Two of such frames as depicted in Figure 4.3 together, formed one double-framed image from which one vector field could be calculated. The way that was done was already briefly explained in the first chapter. Of the parameters involved only the ones that determined the final spatial resolution and some of the ones that influenced the fidelity of the vectors are clarified below.

The calculation consisted of determining the peak of the cross-correlation function for each interrogation window (to reduce computation time this was done in the frequency domain (using the Fast Fourier Transformations of the images). The multi-pass method that was used consisted of two passes with interrogation window sizes of 32 x 32 pixels and a final pass with window sizes of 16 x 16 pixels. Deformed interrogation windows were used to increase the fidelity of the vectors even more. The displacement vectors obtained from each previous pass were used as initial shifts for the interrogation windows of the following pass. Since the final interrogation windows overlapped 50 % in both horizontal and vertical direction, the final spatial resolution was 8 pixels. This meant that the space between two neighbouring vectors was ca. 1.2 mm and that each vector map contained about 15000 vectors. To give a notion of the sizes of the interrogation windows in relation to the size of a complete image both a 32 x 32 pixels and a 16 x 16 pixels window are depicted in Figure 4.3.

Although the spatial resolution of 1.2 mm was not large enough to unveil the smallest scales in the flow (down to the Kolmogorov scale), it was sufficiently large to reveal the smallest of phenomena capable of moving the target stone (it was assumed that these phenomena could not be much smaller than the target stone).

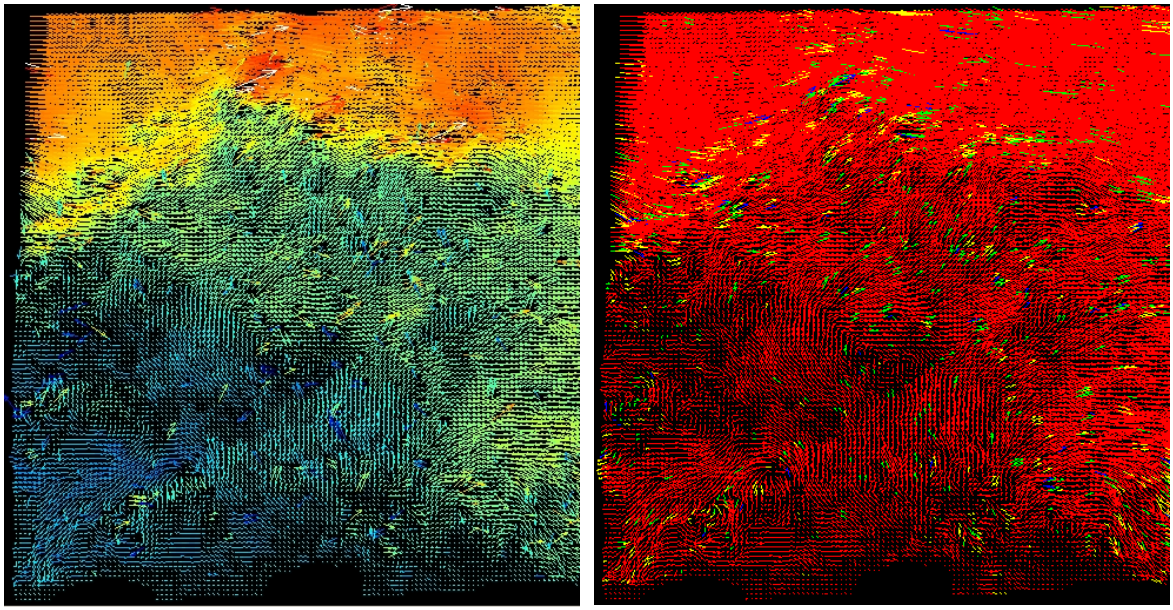

FIGURE 4.4 *Left-hand side of figure: example of a vector field before postprocessing. The vector colours depict the u-velocity (red = positive, blue = negative). Right-hand side of figure: same vector field after postprocessing. The colours of the vectors now indicate on which correlation peak they are based: red = first peak, blue = second peak, green = third peak, yellow = interpolated vectors.*

Figure 4.4 shows the same arbitrarily chosen velocity field twice, both times in the form of a vector plot. The picture at the left side depicts a vector field that resulted from the multi-pass method before it was postprocessed, the one at the right side after it was postprocessed. From this figure it can be seen that, although the vector field at the left-hand side (before postprocessing) already looks quite reasonable, the appearance of the one at the right-hand side (after postprocessing) is even smoother. We mention that the postprocessing step mainly involved filtering out spurious vectors and replacing them by iteratively calculated ones by means of the median filter that is explained below. No smoothing was used during postprocessing.

Not only the appearance had to be such that further digital analysis was feasible, the fidelity of the vectors had to be high as well. The parameters that probably influenced the fidelity the most were the minimum permissible value of the peak ratio factor Q, the criteria of the median filter that was used and the fact that vectors outside an allowable range of velocities were rejected.

The peak ratio factor Q factor was defined as: $Q = (P_1 - min) / (P_2 - min)$, in which min is the lowest value of the correlation plane and P_1 and P_2 are the heights of the highest and second highest correlation peak respectively.

The median filter computed a median vector from the eight vectors adjacent to the vector under consideration and compared this vector to the median vector. The vector under consideration was rejected when it was outside the allowed range of the median vector $\pm$ x times the root-mean-square-value of the eight neighbour vectors and, if so, a new iteratively calculated vector was inserted. In fact the deviation was not computed on all components; rather the two most deviating values were ignored (only if more than five neighbouring vectors existed). Besides, vectors with less than a predetermined number of neighbouring vectors could be removed as well. This filter was a powerful tool that was even capable of rejecting groups of spurious vectors and was ideally suited whenever it was desired that a vector field should not contain any spurious vectors, even with the drawback that some good

vectors were rejected too. As false vectors usually deviate by a large amount, this was for instance the case when averages had to be calculated. For quantities that consist of derivatives of velocities, like vorticity, spurious vectors were even less wanted, as in these cases bad vectors create even larger errors. Some other advantages of this filter were: it was independent of the frame of reference, it was independent of the magnitude of the vectors and it adapted to changing magnitude of the velocity gradient.

Since measurements were conducted at different distances downstream of the BFS and sometimes with different discharges as well, the flow phenomena, turbulence intensities and mean flow velocities at the measuring section were never the same. This occasionally required different time intervals between the two laser pulses needed to construct one double-framed image and as a consequence sometimes the values of parameters involved in the vector computation procedure needed to be adapted as well. Of the experiment B006, the experiment that is analysed in Chapter 6, the values of all parameters can be found in appendix G. For an explanation of the terms used herein one can for instance consult LaVision (2002).

For most of the experiments B006 – B010 we managed to obtain velocity fields of which more than 90% of the vectors were based on the highest correlation peak (the red, first choice vectors of the right-hand side of Figure 4.4). For all experiments the second choice vectors (based on the second highest correlation peak) together with the first choice vectors was more than 90% of the total amount of vectors. (So, more than 90% of the vectors was based on measurements and these vectors were not obtained by interpolation) To arrive at these results the values of all vector computation-related parameters could be kept constant for all the experiments B006 – B010.

More postprocessing (in Matlab)

Although the DaVis software package offered a lot of ways to visualise the velocity fields, we also needed to perform operations for which DaVis could not be used. For these operations Matlab was used instead, primarily to calculate conditionally averaged vector fields and spliced images, to filter the vectors with a Gaussian filter to avoid aliasing when for clarity it was desired to plot only every other vector, for plotting the local swirling strength and to perform a classification procedure. Besides, Matlab enabled us to make contour plots of the velocities, streamline plots, plots of the divergence and so on. The most important of these visualisation methods and the ones we came up with ourselves are explained in the next paragraphs.

4.5.2 Conditional averaging

Instead of looking at all the flow fields corresponding to points in time at which stone movement events took place one by one, we also examined the average of these flow fields. Since only the flow fields around stone movement events were used to construct the average flow fields, the average fields are called “conditionally averaged” flow fields, the movement of the target stone being the condition that had to occur.

To explain how the conditionally averaged vector fields were constructed, we introduce N to denote the total number of events, n to denote the rank of a single event and i to denote a single vector field (see also Figure 4.5). As both the vector fields of points in time before and after movement of the target stone were of interest, i could be positive or negative. First all N series of vector fields had to be synchronised. The first image at which the pivoting motion of the target stone was discernible (i.e. the first frame at which the continuous upward motion was observable, which was not necessarily the same as the frame at which the very first displacement was visible) was used for this and named $i = 0$. Then we summed every i^{th} vector field of each event, and divided the result by N. This was repeated until an average flow field was known for a desired time-span (i.e. a desired range of i). Obviously, the

number of frames before and after the start of the pivoting motion that were included in the conditional averaging could be varied. In the following figure the procedure is visualised.

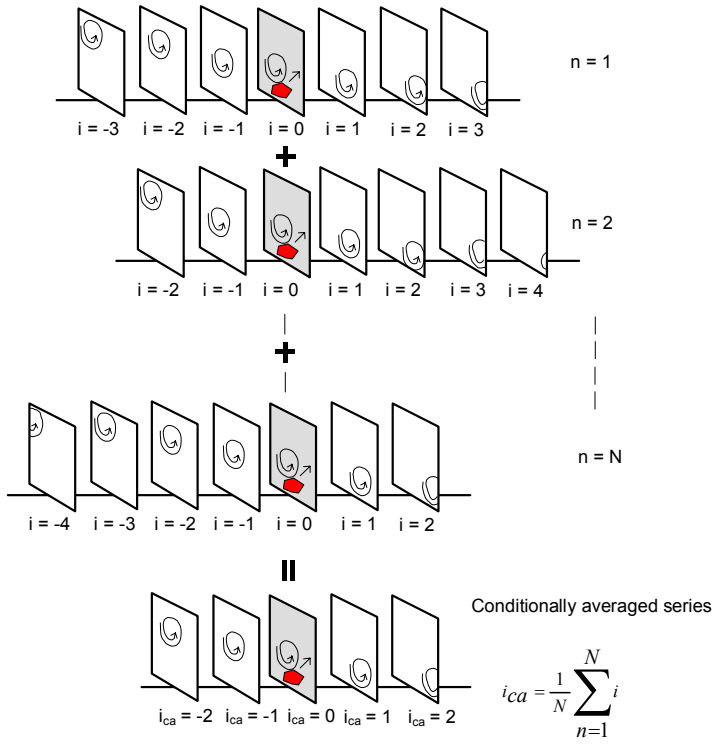

FIGURE 4.5 *Schematic representation of conditional averaging. Each row represents a single event; the frame that is coloured differently is the first frame at which the pivoting motion of the target stone is visible (stone starts to pivot somewhere between i = -1 and i = 0). In this example each event consists of seven vector fields. Due to the synchronising the resulting conditionally averaged series consists of only five frames.*

Although one might think that conditional averaging could prevent that all events had to be inspected and that it is a reliable technique as it is based on several events, still the instantaneous velocity fields of all events had to be inspected and we had to be careful with drawing conclusions from the conditionally averaged flow fields.

In the first place, because of the low-mobility conditions, the number of approved events was relatively small. Secondly, clear patterns might result from conditional averaging, but these patterns (e.g. a vortex) may have been smeared out by the jitter in the location of the centre of the pattern (location of centre of the vortex). Thirdly, if there were two (or more) structures capable of dislodging the target stone, both (or all) structures were likely to appear in the conditionally averaged vector fields while in reality the presence of only one structure may have been the cause of movement.

In spite of these limitations, conditional averaging was a very useful tool. Although a pattern might have been boosted and appeared more distinct in the conditionally averaged vector fields than it was in reality, it was present in reality, albeit less distinct. Besides, to get around the last drawback we came up with a method to classify the causes of entrainment before conditional averaging. This method is described in the next section.

4.5.3 Classification

Results from the uniform-flow conditions showed that the entrainment of stones often was caused by either a vortex, a less vigorous vortex that was immediately followed by a sweep event or just a sweep event (Hofland & Booij, 2004). To find out if also a distinction could be made in the causes of entrainment of stones downstream of a BFS, we compared the values of two characteristic parameters of the flow in the vicinity of the target stone just before entrainment, with values in periods in which no stone movement occurred.

In Chapter 2 a distinction was made in the causes of forces on stones in the top layer of a granular bed. Two mechanisms were discussed: turbulent wall pressures (TWP) and Quasi-steady forces (QSF). We defined two parameters, one to indicate the magnitude of the force on the target stone caused by the longitudinal velocity (QSF) and one to be used as an indicator for the other force generating mechanism, viz. TWP. Since the steady drag and lift force vary according to $u|u|$ and u^2 respectively, the first parameter was defined as: $F_A \propto \langle u \rangle_A |\langle u \rangle_A|$. In this, A denotes an area in the vicinity of the target stone of which the dimensions are determined later on in this report. As vortices that procure TWP fluctuations can be identified as relatively large fluctuations of the velocity normal to the bed (large v'), the instantaneous spatial standard deviation of this velocity in an area B, denoted by $\sigma_B(v)$, is relatively large if a vortex is present and could therefore be used as an indicator for the presence of the second force generating mechanism. The dimensions of area B did not have to be the same as those of A, but obviously also area B had to be in the vicinity of the target stone. Again the size of B is determined later on.

If one of both mechanisms was responsible for the dislodging of the target stone from its pocket, then, around movement of the target stone, the value of the corresponding parameter should be larger than its time averaged value. So if a scatter plot was made of F_A versus $\sigma_B(v)$ the values corresponding to moments in time just before movement of the target stone should be positioned relatively far from the mean values of F_A and $\sigma_B(v)$[*]. In the next chapter this procedure is applied to the obtained velocity data.

4.5.4 Splicing

It may well be possible that a structure or phenomenon that caused the target stone to move was much larger than the measuring area or existed much longer than the time between the two consecutive laser pulses used to construct one vector field. Therefore a technique was used to regard the large-scale flow structure, which we called "splicing". It is based on the Taylor hypothesis, also known as the frozen-turbulence approximation, which states that: if $u' << \bar{u}$ then $u(\bar{u}t) \approx u(x)$ and $Du/Dt \approx 0$ ($= \partial/\partial t \approx -\bar{u}\, \partial u/\partial x$). In words: as long as the structures under consideration do not change during the passage time and the velocity fluctuations caused by these structures do not affect the transport velocity significantly, the turbulence is seen as a field in which the structures are frozen and which passes with a constant velocity along a fixed observation point.

The splicing technique is a hybrid technique to merge a sequence of recordings. To this end, first the correlation of the upstream part of the u' field of the first image and an equally sized downstream part of the u' field of the second image was determined as a function of the overlap length. Subsequently the overlap length for which the correlation function was maximal was used to create a new flow field by averaging the velocities of the overlapping part of the two images and adding the remaining parts of the original images on the correct sides. Successively, this total image was used as the first image and the third image of the

[*] As we used $F_A \propto \langle u \rangle_A |\langle u \rangle_A|$ and not $F_A \propto u^2$, the direction of the forces remained known. Notwithstanding the fact that negative drag forces could not lead to entrainment of the target stone, because of the way the hinge was manufactured, it remained favourable to conserve the signs of F_A. A correct sign meant that the average value of F_A was not spoiled.

series as the second. This procedure was repeated for all recordings of a single event. A visualisation of the procedure is depicted in Figure 4.6.

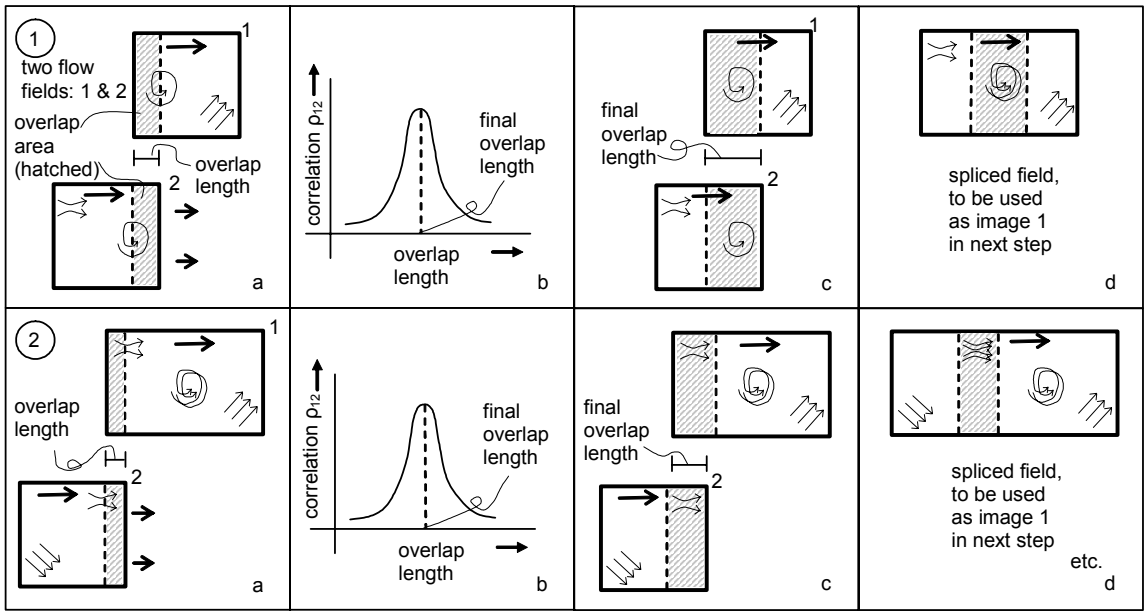

FIGURE 4.6 *Schematic representation of splicing technique.*

The function that was used to determine the correlation of two consecutive velocity maps reads:

$$\rho_{12}(overlap\ length) = \frac{\left\langle u_1' u_2' \right\rangle_{overlap}}{\sqrt{\left\langle u_1'^2 \right\rangle_{overlap} \left\langle u_2'^2 \right\rangle_{overlap}}} \tag{4.3}$$

in which the subscripts *1* and *2* refer to the corresponding images and ρ_{12} is the normalised cross-covariance function. See for instance Bendat & Piersol (1971) for more details about this type of function.

The overlap length for which ρ_{12} was maximal was taken to be the final overlap length. For this length the two flow fields matched best. From this resulting final overlap length and the known time between two consecutive images (Δt), the mean (instantaneous) convection velocity U_c of the total structure could be determined:

$$Final\ overlap\ length = max(\rho_{12}(overlap\ length)) = U_c\, \Delta t \tag{4.4}$$

If the final overlap length calculated by this function deviated more than a predetermined value from the median overlap length (as determined from a first calculation round), the median overlap was used instead. From Eq. (4.4) it follows that the horizontal axis of a spliced image represents both the x co-ordinate as well as the time (or to be more precise: $U_c \Delta t$).

Due to the nonuniformity of the flow downstream of a BFS, the frozen turbulence assumption is not really valid. Therefore the splicing technique was best suited for the measurements that were conducted relatively far downstream of the BFS. For the measurements relatively close to the BFS, the spliced images have to be interpreted as the development of the flow in the measuring section in time, rather than a spatial reproduction of the flow upstream and downstream of the target stone at the moment of stone movement.

Another difficulty that was encountered when using the splicing technique for BFS flow was the fact that the flow consisted of two parts, separated by a shear layer, of which the velocities differed tremendously. In the upper part near the water surface, high streamwise velocities occurred, while in the part near the bottom very low, or even negative, velocities could be found. A vortex in the upper part of the flow was not likely to span a part of the region with low velocities as well. So, when the correlation function was employed to determine the overlap length, this length was long if the highest correlation was found in the upper part of the flow and relatively short if it the highest correlation occurred in the lower part.

4.5.5 Visualisation techniques

Though the techniques that were described above already offered a lot of data analysis possibilities, there were some other convenient visualisation techniques. Obviously we used the vector representation of both absolute and decomposed velocity fields to gain insight, but in particular colour-coded contour plots of the velocities yielded a lot of insight at once. Of course, plots at which only the values of the local swirling strength above a certain threshold value were displayed were very useful too. To investigate the quasi-periodic mechanisms, plotting of the streamlines could be used to see if a flapping motion was present or the data could be analysed in the frequency domain.

Most of the times a combination of the aforementioned techniques was used. For instance, conditionally averaged, spliced velocity fields were constructed. To display these fields, filled contour plots were most suited. Vector plots were well suited to be accompanied with a colour-coded background to indicate local values of quantities like swirling strength, divergence etc. In the next chapter extensive use is made of these techniques.

5 RESULTS: MEAN FLOW AND TURBULENCE CHARACTERISTICS

5.1 Introduction

From the third chapter it is known that the flow conditions in the experiments B006 through B010 were almost equal, and it was decided that of these tests only B006 would be used in the search for causes of entrainment of stones from bed protections downstream of a BFS. But before the measured pressures and in particular the 2-D velocity measurements of experiment B006 are analysed in detail, it is convenient to have an overview of the mean flow conditions of the experiments with peer flow conditions. Some mean flow quantities are given and compared to results of other authors. Besides, the overview enabled us to deduce the location of the mean reattachment point. The following quantities are considered: mean horizontal velocities, turbulence intensities and the mean reattachment length.

5.2 Longitudinal velocity and turbulence intensity

5.2.1 Profiles of $\bar{u}$ and u'

Vertical distributions of $\bar{u}$ and u' are plotted in Figure 5.1 for several distances downstream of the BFS. The mean large-scale properties of the flow are clearly visible:

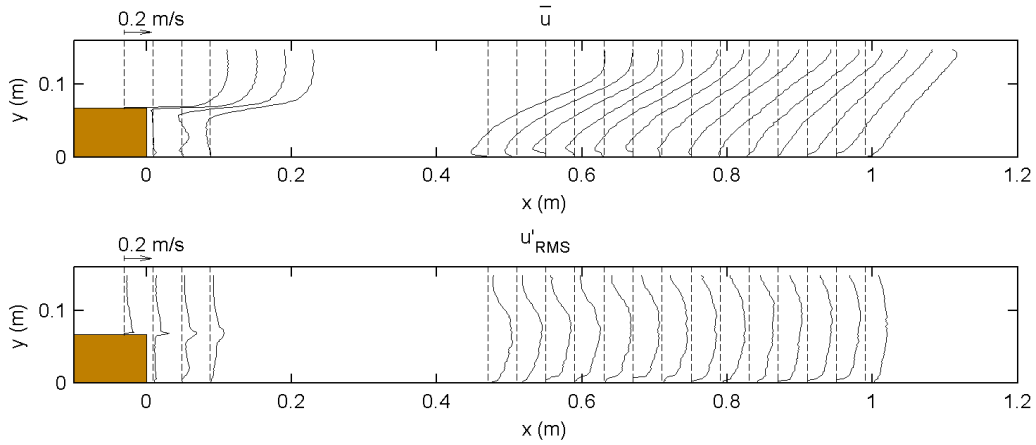

FIGURE 5.1 *Upper plot: profiles of mean longitudinal velocity. Bottom plot: root mean square value of longitudinal velocity fluctuations. The distance between two consecutive cross-sections for which profiles are plotted is fixed.*

The upper plot ($\bar{u}$) clearly shows the main flow phenomena of a BFS flow as described before in chapter 2. A zone with negative velocities is visible near the bottom, stretching from $x = 0$ m to about $x = 0.80$ m. In this region a spiraling clockwise motion was present. The secondary eddy that is normally located directly downstream of the step is not visible here, on the contrary, a gust with positive u-velocity can be found. This was most probably caused by seepage through the foam rubber that was used to close the gap in the cross-board at the downstream side of the BFS. This seepage was only present during the last experiment when the step structure was placed in the laser sheet. Further downstream the velocity profiles develop gradually towards a log-law profile, although this profile cannot yet be found within the measured range.

In the bottom plot, the increased longitudinal velocity fluctuations directly downstream of the step at the same height as the step indicate the presence of a shear layer between the upper part of the flow and the recirculation bubble. From the profiles it is observable that, with increasing distance from the step, the part of the depth in which the fluctuations are significant, increases. Also from this plot one can see that the relaxation to an equilibrium profile is slow. The profile located all the way at the right, displays larger fluctuations near the water surface than its neighbouring profile, indicating that the profile is still far from equilibrium. As the step height was less than half of the water depth downstream of it, it was to be suspected that the most upstream location at which the presence of the BFS (the mixing layer) would influence the flow near the water surface would be further from the step than the mean reattachment point. The exact location at which the flow reattaches to the bed is determined in one of the following sections.

5.2.2 Check of similarity of flow conditions

The edges of the recorded PIV images were often of minor quality, resulting in spurious vectors or no vectors at all at the boundaries of the measuring area. However, the measuring areas overlapped a little in horizontal direction to obviate this and to achieve that vectors were known for a continuous stretch downstream of the BFS. Nonetheless, after calculating vectors it turned out that between experiment B006 and B009 still a small stretch without reliable vectors was present.

The overlapping of the measuring area also enabled us to check to what extent the experiments were conducted under the same flow conditions. If the flow conditions were indeed identical, then in the overlapping areas the velocity profiles obtained from two different, but adjacent experiments should coincide. This check is visualised in Figure 5.2.

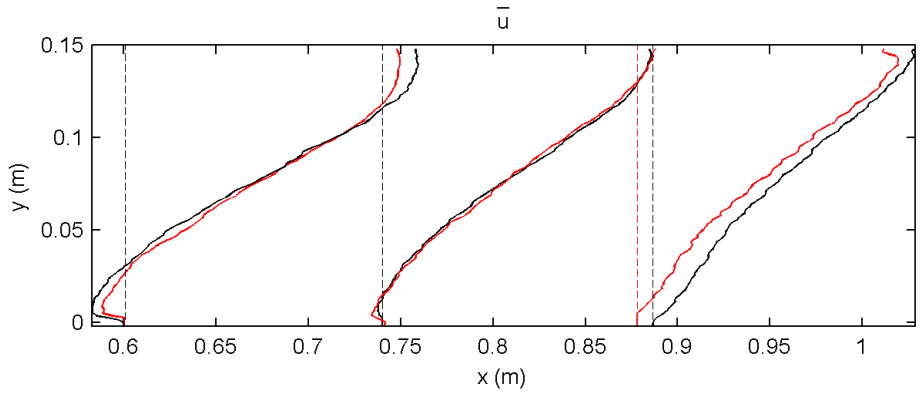

FIGURE 5.2 *Comparison of mean longitudinal velocity profiles of adjacent measuring areas. Left-hand side: B007 (red) and B008 (black); centre: B008 (black) and B006 (red); right-hand side: B006 (red) and B009 (black). See also Figure 3.12.*

From the profiles at the left-hand side of Figure 5.2 it is observable that the flow conditions during experiment B007 and B008 were not exactly the same. The profiles in the centre on the other hand, coincide very well, indicating that the flow conditions during experiment B008 and B006 were very much alike. The remaining two profiles do not correspond to the same value of x, for reasons explained above. Nevertheless, one can conclude that the flow conditions during B006 and B009 could not have differed tremendously, as the profiles look very much alike.

5.2.3 Determination of mean reattachment length

From Figure 5.1 it seems that the flow reattaches to the bed in the region around x = 0.8 m. To determine this length more precisely, a zoomed plot of the area around x = 0.8 m, as depicted in Figure 5.3 was used. Obviously, in this picture the horizontal distance between two consecutive velocity profiles is less than in Figure 5.1 to pinpoint the location of the reattachment as accurate as possible. As near the reattachment point the average horizontal velocity near the bottom is zero, the profile of $\bar{u}$ near the reattachment point should be recognisable by its vertical part near the bed. Moreover from the mean reattachment point on, the mean u-velocity should only be positive.

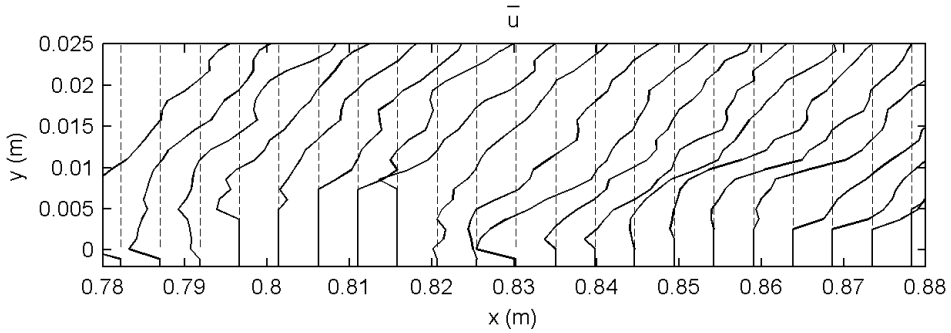

FIGURE 5.3 A*rea around the mean reattachment point: profiles of mean longitudinal velocities*.

The several zero-velocity areas that are clearly visible in Figure 5.3 are due to the stones that were present at these locations. In fact there is no profile observable that has a vertical part that indicates the location of the mean reattachment point and even from Figure 5.3 it was still hard to identify the exact location of the mean reattachment point. Downstream of x = 0.80 m, the u-velocity appears to remain positive over the entire depth, but a closer look reveals that even further downstream, at x = ca. 0.83 m, negative velocities occur near the bed again. We presumed, however, that these negative velocities were caused by the stones in the bed (wake behind a stone) and that the first cross-section at which no negative velocities occurred indicated the location of the mean reattachment point. So hereinafter X_R = 0.80 m, or $X_R \approx 12H$. A distance of $12H$ between the step and the mean location of reattachment is longer than the distances that were encountered in literature. In one of the following paragraphs a possible reason for this rather large value of X_R is introduced.

5.2.4 Relative depth-averaged turbulence intensity

In a guideline for the design of granular bed protections downstream of discharge structures (Franken *et al.,*1995) it is suggested to use the relation introduced by Hoffmans (1993), Eq. (2.24), to obtain the depth-averaged relative turbulence intensity $\langle r \rangle_h$. The relative turbulence intensity is defined as: $r = \sigma_u / \bar{u}$. Subsequently, the obtained value of $\langle r \rangle_h$ can be used in a design criterion (e.g. Eq. (2.25) can be used after substituting $\langle r \rangle_h$ in Eq. (2.23)). To check its validity, we compared Eq. (2.24) with our measurements, see Figure 5.4.

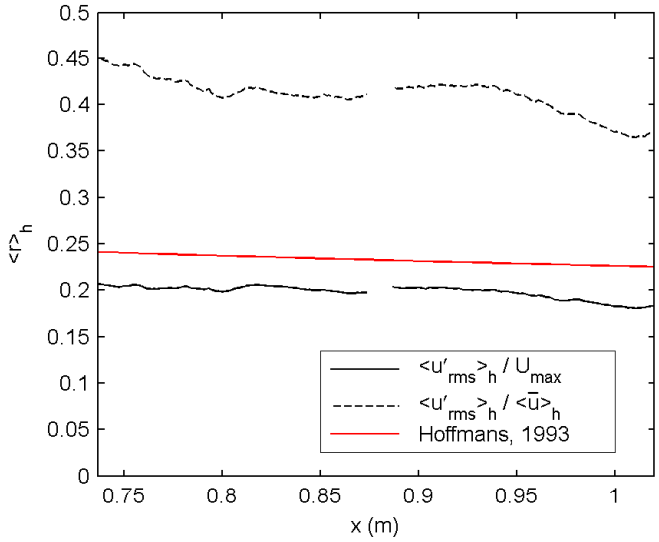

FIGURE 5.4 *Depth averaged relative turbulence intensity, measurements compared to Hoffmans (1993).*

The velocity that is used for normalising the turbulence intensities is of great influence on the value of $\langle r \rangle_h$. It is generally presumed that Eq. (2.24) yields the depth-averaged turbulence intensity relative to the local depth-averaged velocity. However, further investigation of the origin of the terms in Eq. (2.24) revealed that most terms are related to BFS flow and only one (the last term at the right-hand side) originates from uniform flow. In BFS flow studies U_0 is generally used to make turbulence intensities dimensionless, while for uniform flow $\langle \bar{u} \rangle_h$ is commonly used. So it is not so trivial that Hoffmans' formula yields turbulence intensities relative to $\langle \bar{u} \rangle_h$. Figure 5.4 confirms this train of thought, as the measured intensities normalised by $\langle \bar{u} \rangle_h$ deviate largely from Hoffmans' formula, while the use of U_{max} ($\approx U_0$, see §5.3.1) for normalising yields a good resemblance. This holds for the slope of the lines (relaxation rate towards a log-law profile in streamwise direction) as well as for the values of $\langle r \rangle_h$. Moreover, Hoffmans presumed that the location of the reattachment point is always $X_R \approx 6H$, which is a rather crude assumption, see §5.3.2.

5.3 Comparison to other experiments

5.3.1 Longitudinal velocity

To compare our results with the results of Nakagawa & Nezu (1987) the velocities were made dimensionless by dividing them by U_{max}. This is the spatial maximum of the time averaged horizontal velocity that occurs in a BFS flow. In other words: U_{max} is the mean velocity near the water surface right above the trailing edge of the step (at $x = 0$). This velocity resembles the free stream velocity U_0 of boundary-layer experiments. We measured $U_{max} = 0.72$ m/s. Both the horizontal distance from the BFS as well as the vertical co-ordinate are made dimensionless by the step height H. Furthermore, in both cases the ratio H / h_2 was approximately the same, viz. 0.35 and 0.38 for the experiments of Nakagawa & Nezu and our experiments, respectively.

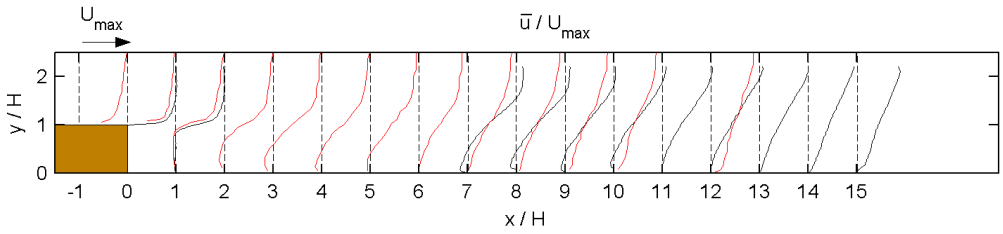

FIGURE 5.5 *Plot of dimensionless mean longitudinal velocity. Black lines: present experiments; red lines: Nakagawa & Nezu (1987).*

Although near the step the profiles taken from Nakagawa & Nezu are almost identical to the ones taken from the present experiments, both sets of profiles deviate largely at distances further from the BFS. Clearly this was to be expected as we already found that the mean location of flow reattachment in our experiments was located much further from the step than Nakagawa & Nezu found. Altogether both sets of profiles display the same kind of development, only the development in the present measurements is slower than that of Nakagawa & Nezu.

Near the water surface, e.g. at $x / H = 7$, the velocity is even larger than U_{max}. This can be caused by differences in the flow conditions between experiment B010 (on top of the step structure) and the experiments conducted downstream of the BFS. Most probably it cannot be assigned to a physical phenomenon, although the relatively small width of the flume may be a cause. Unfortunately, we had no data available for the part between $x / H = 1$ and $x / H = 7$ to compare both flows in this area.

As the most striking difference is the location of the mean reattachment point, we decided to compare values of the mean reattachment length obtained by different authors in the following section.

5.3.2 Dependence of the mean reattachment length on the Froude number

Nakagawa & Nezu (1987) already suggested that the Froude number (Fr) could affect the mean reattachment length, as they found that X_R tends to increase with increasing Froude numbers. This dependence is assigned to undulations of the water surface that occur when Fr increases. They also showed that X_R varies with the Reynolds number such that X_R decreases asymptotically to a constant, minimum value when the Reynolds number increases. We therefore only used data of experiments conducted with high Reynolds numbers ($Re > 18000$) to investigate the influence of Fr. Results from numerical simulations and from experiments conducted in ducts were not included*. So, we only compared results taken from high Reynolds, open channel flow experiments, to construct Figure 5.6.

* In general it seems that X_R in duct flow is less than in open channel flow, even for large Froude numbers. Obviously the pressure distribution in duct flow differs largely from open channel flow. Sometimes even a second recirculation bubble forms under the upper wall of the duct, indicating that this type of flow cannot, without more ado, be compared to free surface flow.

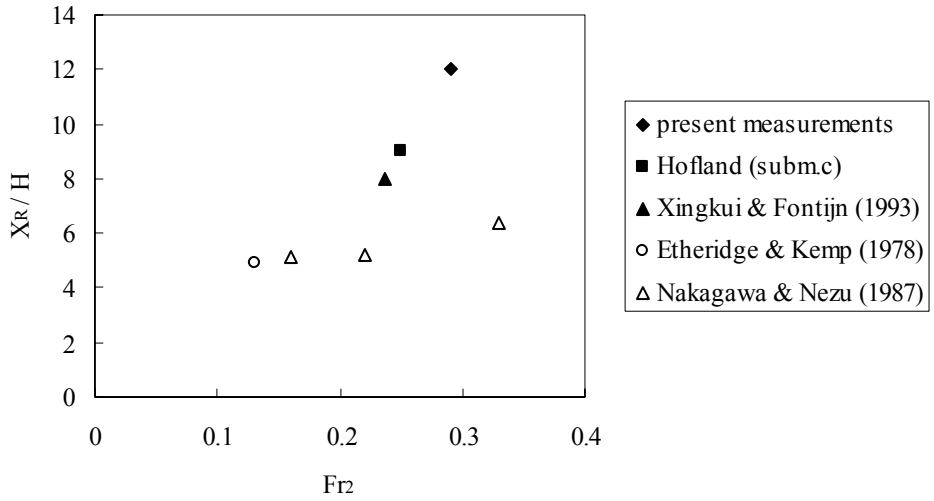

FIGURE 5.6 *Dependence of the mean reattachment length on the Froude number (downstream). Solid markers: rough wall. Open markers: smooth wall.*

One major difference between the experiments of Figure 5.6 is that the ones by Nakagawa & Nezu (1987) and the one by Etheridge & Kemp (1978) concerned smooth walls, while the others were conducted with a bottom wall downstream of the BFS that consisted of roughness elements. Still, the tendency of the mean reattachment length to increase with increasing Froude numbers is clear from this graph. It seems, however, that X_R tends to be larger in cases of a rough wall. Most probably the relatively large Froude number in combination with a rough wall caused the large X_R found in the current experiments.

Further investigation on both the influence of *Fr* as well as the influence of the roughness on X_R is desired, as there are only a few experiments available. Besides, it is not clear yet why a rough wall gives rise to larger values of X_R. We used Froude numbers based on the water depth and velocity downstream of the step, as did Nakagawa & Nezu. However, a high Froude number on top of the step structure also causes undulations, so maybe the ratio h_1 / h_2 also influences X_R as this ratio determines the values of Fr_1 and Fr_2. Yet another possibilty that may influence X_R, is the width of the flume. A limited width might prevent the less energetic mode of the 3-D structure to occur, hence forcing the 3-D structure to adapt to another mode, which in turn can yield a different value of X_R.

5.4 Mean flow around reattachment region

As the next chapter focuses on experiment B006, it is convenient to consider the mean flow field of this experiment in somewhat more detail. In the following figure the mean flow field of experiment B006 is visualised by contour plots of both the horizontal and the vertical component of the velocity.

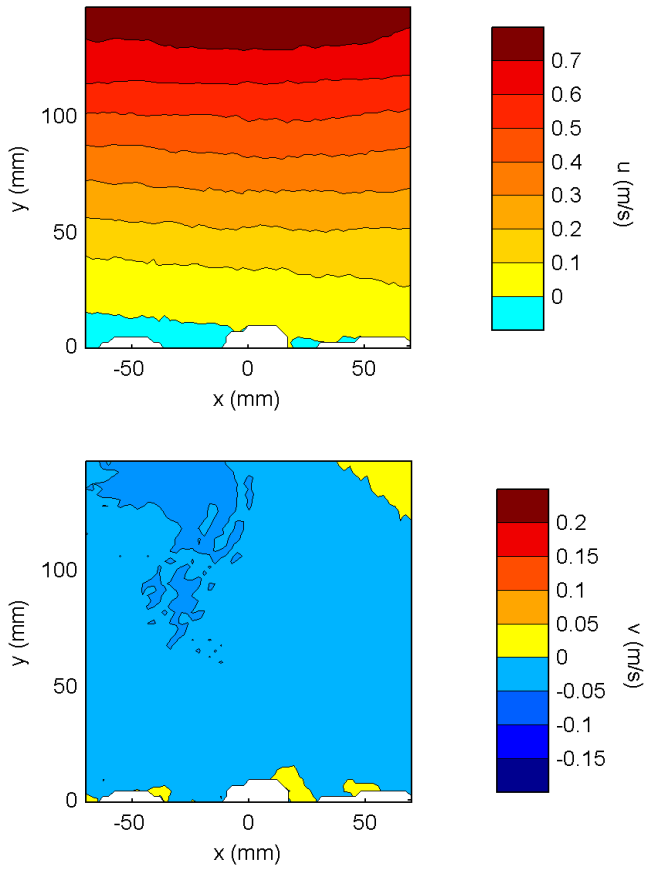

FIGURE 5.7 *Mean flow of experiment B006. Upper plot: u-velocity. Bottom plot: v-velocity. Target stone located at x = 0.*

In this figure a local co-ordinate system is used, that has its origin in the centre of the target stone, i.e. at $y = 0$ m and $x = 0.805$ m (see Table 3.2) of the global co-ordinate system that has been used hitherto. Note that the velocities are colour-coded in a way that positive velocities are indicated by the range yellow ─ red, with red corresponding to the highest velocities, and the range light blue ─ dark blue indicates negative velocities, where dark blue is used for the largest negative velocities. So it is immediately clear, which part of the flow has a positive velocity and which part a negative.

In the upper plot one can see that the target stone is located exactly at the mean reattachment point. So during experiment B006, the measuring area covered the reattachment region. Near the water surface the mean horizontal velocity has still the same order of magnitude as the mean horizontal velocity near the water surface upstream of the BFS.

In the bottom plot one can see that on average the flow is directed slightly towards the bed, meaning that the water surface dropped in the direction of the mean flow or that the flow was not completely 2-D at this location. Since Figure 5.7 is only a visualisation of the flow in the

centre of the flume, it might have been possible that near the walls of the flume the flow on average was directed slightly towards the water surface. Then some kind of large-scale spiralling motion must have been present. In that case there must also have been significant lateral velocities (*w*-velocity) in the centre of the flume. Even though we could not measure these velocities, their presence could be deduced from our 2-D velocity measurements by looking at the divergence of the 2-D flow fields. Fortunately, there were no areas observable in the mean flow field that indicated large *w*-velocities.

Although contour plots are very convenient to visualise the flow in an orderly way, it is still hard to imagine the 2-D flow structure from these plots. Vector plots are much more useful for this purpose, but as mentioned before, the large range of velocities made it hard to print clear vector plots on paper. By plotting streamlines on top of vectors, it is nonetheless feasible to give an impression of the 2-D flow structure:

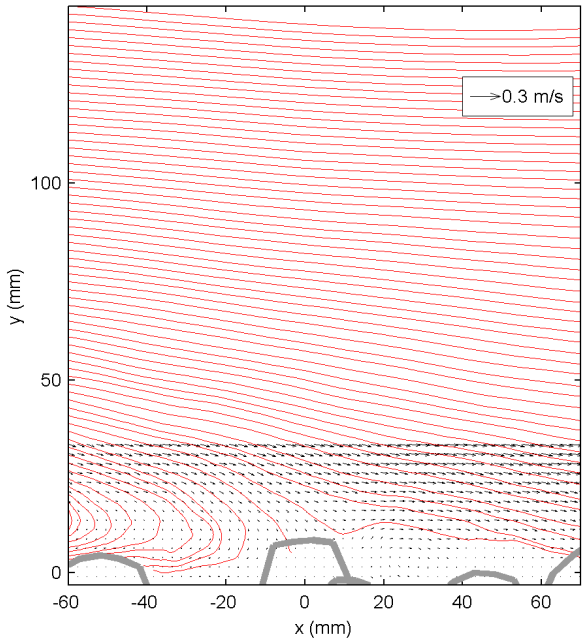

FIGURE 5.8 *Mean flow around the mean reattachment point, visualised by velocity vectors (for clarity only in the lower part of the flow) and streamlines.*

Figure 5.8 gives a good impression of the mean flow pattern around the reattachment region. Again the recirculation zone is clearly visible. Behind the target stone a vortex is visible, caused by obstruction of the flow. So we were indeed right when assuming that the negative horizontal velocities near the bed at this location were not due to the overall flow pattern and when we argued that X_R = 0.80 m in §5.2.3. It can also be seen that the time-averaged dividing streamline (the streamline that divides the streamlines inside the recirculation bubble from the ones outside of it) is much steeper and situated somewhat higher than the contour line between the blue and the yellow area of the upper plot of Figure 5.7. This is perfectly logical, although it may seem contradictory at first. The dividing streamline may be considered as the centre of the shear layer, while mean negative horizontal velocities only occur well inside the recirculation bubble.

The course of the dividing streamline is not in agreement with the observation of other authors, namely that the shear layer remains horizontal for a long time before suddenly starting to bend towards the bed a little upstream of the reattachment point. This general observation however is based on smooth wall, duct experiments. Our observation is maybe

different due to the presence of the rough bed downstream of the BFS or the free water surface.

6 RESULTS: TURBULENCE STRUCTURES AND ENTRAINMENT

6.1 Introduction

In the previous chapter the measured time-mean flow field behind a BFS was presented. It was observed that during experiment B006 the target stone was located at the mean reattachment point. In this chapter only the data collected during this experiment are used.

The mean reattachment region is a very interesting location. As the mean longitudinal near-bed velocity is low, the mean drag force on bed elements is small, leaving turbulence as the sole cause of entrainment. Surely it is to be expected that during entrainment the instantaneous flow field deviates significantly from the average field, but it is not known yet in which manner.

The purpose of this chapter is: (1) to find out if there is only one type of flow structure that can be held responsible for entrainment in the reattachment region or that it is a combination of flow structures; (2) to describe the structure(s) in detail; (3) to discover if the (combination of) structure(s) is an intense version of a common (combination of) structure(s), or a very rare (combination of) flow structure(s); and (4) to investigate the influence of the quasi-periodic mechanism related to BFS flow on entrainment in the vicinity of flow reattachment. Moreover, throughout this chapter, the results are compared to the results obtained from the uniform flow experiments (Hofland, 2004).

We used the classification procedure and conditionally averaging procedure as described in Chapter 4 and visualised the flow around stone movement in several different ways. We analysed the spectra of the measured pressures and looked at the evolution of the flow in the reattachment region in time. To verify the mobility conditions and to compare them to the uniform flow experiments, this chapter starts with a brief analysis of the signal that indicated stone movement.

6.2 Occurrence of stone movement

The established flow conditions yielded such low-mobility levels that stone movement events were very rare. Probably the number of events was too low to derive reliable statistical quantities from them. Therefore the signal from the inductive sensor was only briefly analysed and all stone movement events registered by the inductive sensor were included when possible, even the ones that did not satisfy the criterion for movement, see §3.8.3.

6.2.1 Duration that target stone was detached from the bed

A histogram of the durations of the stone movements of experiment B006 can be found in Figure 6.1. Only the events for which PIV recordings were made were used to construct this graph. Since the difference between these events and all events is caused by the minimum-time-up criterion, there would only have been more very short duration events when all events would have been used.

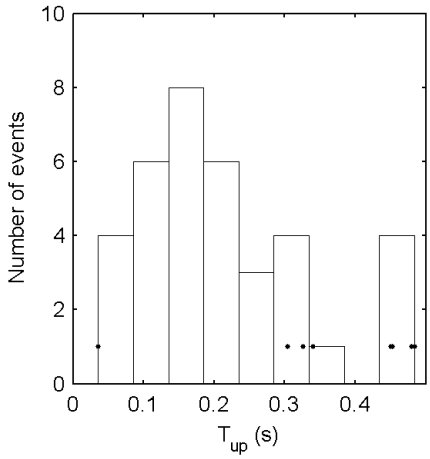

FIGURE 6.1 *Histogram of the durations that the target stone was detached from the bed. The eight visually selected events are indicated by the dots (•).*

During most of the visually selected events, during which the stone reached a large pivoting angle, the target stone was up for a relatively long time (almost all dots are situated at the right-hand side of the graph). Compared to the uniform-flow experiments, however, the target stone returned to its original position fast. During the latter experiments it sometimes stayed up as long as 100 s. When under uniform flow conditions the stone pivoted, then, due to the increased area exposed to the flow in combination with the high mean near-bed horizontal velocity (compared to the present case), large drag forces acted on the stone. Only if, for whatever reason, the *u*-velocity decreased, could the stone fall back. Near reattachment, the situation is completely different and the target stone seemed only to be detached from the bed as long as the flow structure responsible for entrainment was present. This might mean that near the reattachment region stones are only dragged along with the flow over a relatively short distance.

6.2.2 Time between stone movements

A distribution of the time intervals between events is depicted in Figure 6.2. All stone movement events that were registered by the inductive sensor were included.

The line in this graph indicates the chance *P* on a certain time interval between two successive events. As it is a semi-logarithmic plot, the more or less monotonic decrease of the line indicates that the time between stone movements is distributed exponentially. The chance of occurrence of a relatively long time between events is small, but this does not mean that the chance to see stone movement within a relatively short period of time after an arbitrarily chosen point in time is large. On the contrary, it means that this chance is small. After all, although the chance on a long interval is small, the interval itself is very long. The same kind of distribution was found for the time intervals between stone movement events under uniform flow conditions.

Knowledge about the type of distribution of the time between successive events may be helpful when creating a model that links flow conditions to bed damage. One should be aware that Figure 6.2 is based on only one stone and that the target stone was attached to a hinge that only allowed a pivoting motion in the mean flow direction.

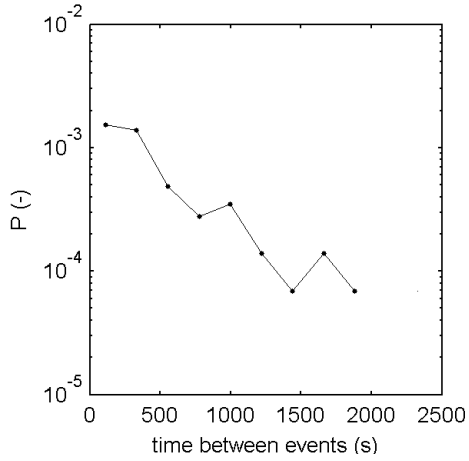

FIGURE 6.2 *Probability density function of the time between stone movement events on a semi-logarithmic scale.*

6.2.3 Stability

An average frequency of movement of one event per 4311 s (see §4.2) seems low, but in fact there is no reference to conclude this. We can only compare it to the uniform flow experiments during which the same target stone with the same relative protrusion moved, on average, once every 526 s.

To have a notion of the stability it would be helpful to know the value of the Shields parameter. However, it was unfeasible to determine the shear velocity or bed shear stress in an accurate way. Therefore another procedure was used to obtain an estimation of the Shields parameter, denoted by Ψ_e, where the subscript e indicates that it is a parameter equivalent to the Shields parameter Ψ. In appendix H the procedure is described in detail, here only a brief explanation is given.

The transport of stones per meter width was calculated and substituted in a transport formula for uniform flow (Paintal, 1971). From this formula the Shields parameter could be deduced. Some crude assumptions needed to be made and data from de Gunst (1999) were used to calculate the transport of stones per meter width from the average frequency of movement. This procedure yielded: $\Psi_e \approx 0.035$.

As the target stone was attached to a hinge that only allowed a pivoting motion in the mean flow direction, the observed average frequency of movement maybe smaller than when the hinge would have been absent. If it is assumed that the average frequency of movement would have been twice as high if there had been no hinge, the procedure yields an equivalent Shields parameter that is only a little higher than the value given above.

So, the stability during our experiment B006 corresponded more or less to a stability that under uniform flow conditions is considered a safe choice for the threshold of motion and that is used as a critical value when designing bed protections ($\Psi = 0.03$).

6.3 Classification of causes of stone movement

In this section we investigate which force mechanisms (QSF or TWP) were active at the time of stone movement, by means of the parameters F_A (for QSF) and $\sigma_B(v)$ (for TWP) that were introduced in §4.5.3. Before this could be done, we needed to determine the sizes of the areas A and B for which F_A respectively $\sigma_B(v)$ were calculated. Different sizes were tried and the sizes were chosen that discriminated the values of the two parameters during entrainment from their averaged values based on flow with a fixed target stone the most (see appendix I).

The resulting dimensions for the areas A and B and the accompanying scatter plot of F_A versus $\sigma_B(v)$ are depicted in Figure 6.3.

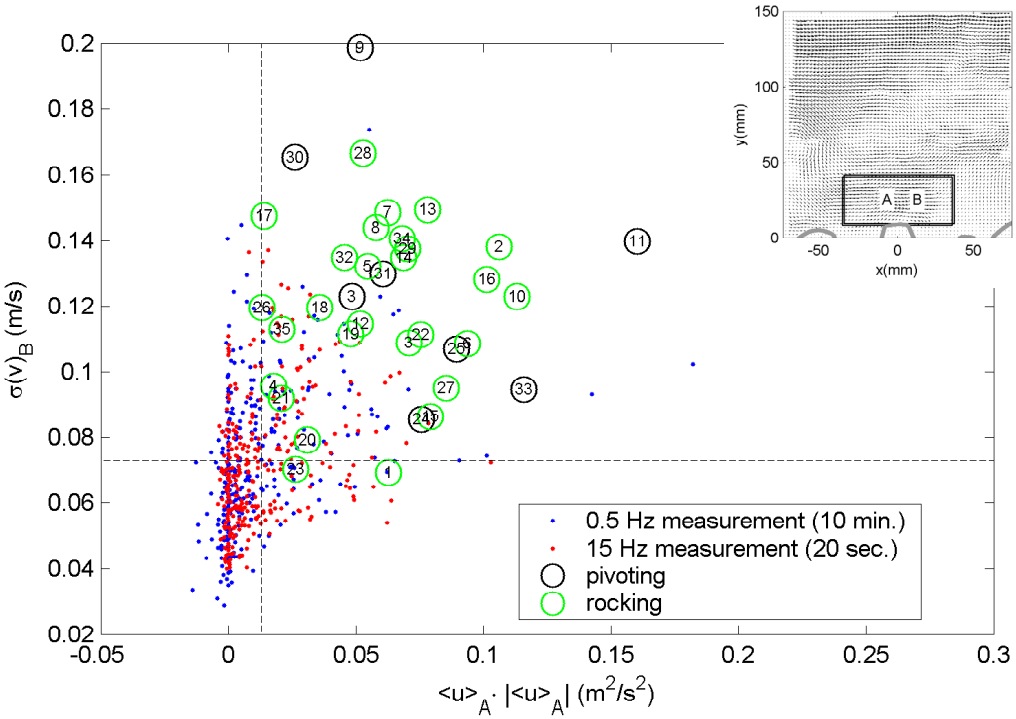

FIGURE 6.3 *Scatter plot of F_A versus $\sigma_B(v)$ of experiment B006 . The numbers in the circles indicate the number of the event (36 events). The dashed lines indicate the average values of the two parameters. Upper-right corner: dimensions of the areas A and B.*

The green circles present the rocking events and are based on the last frame that was recorded before the target stone started to move, the black circles present the visually selected events and are based on the last frame that was recorded before the target stone started to pivot around the axis of the hinge. The small red and blue dots are the results of the 0.5 Hz / 10 min and the 15 Hz / 20 s measurements with a fixed stone.

It is clearly visible that for almost all stone movement events the value of F_A as well as that of $\sigma_B(v)$ are higher than average, especially for the visually selected events. Apparently an increased longitudinal velocity had to occur simultaneously with a large fluctuation of the vertical velocity (probably a vortex) in order to dislodge the target stone from the bed. Although it seems that at least one of the two parameters needs to be relatively large and that a value slightly higher than average for both parameters is not sufficient to dislodge the stone (no visually selected events occur near the intersection of the dashed lines, near event 20), we cannot discriminate two different types of events, caused by either TWP or QSF, as was possible with the events of the uniform flow experiments.

To gain some more insight in the cause of the increased u-velocity (what phenomenon caused the high longitudinal velocity?), the size of the area A provides some information. Since this area is restricted to the vicinity of the target stone, only the u-velocity close to the bed is larger than average during entrainment. If, during entrainment, the u-velocity over a larger part of the depth would have been increased, then a larger area A would have discriminated the events from the average values better. This finding seems logical as experiment B006 was conducted in the vicinity of the mean reattachment point where the upper part of the flow is still quite undisturbed and hardly shows large-scale fluctuations of its mean u-velocity. However, this does not exclude the possibility that the increased u-velocity in area A could

have been caused by a downward movement of a fluid package with high longitudinal momentum from the upper part of the flow (sweep or Q4 event).

Also area *B* is limited to the vicinity of the target stone. This means that the fluctuation of *v*-velocity needs to be located near the bed as well in order to entrain the target stone. Most probably the large fluctuation of *v*-velocity is caused by a vortex, as vortices are capable of creating a large fluctuation in a small area. Moreover from Chapter 2 it is known that a vortex creates an underpressure on the bed that is proportional to a^{-3}, where *a* denotes the distance from the vortex core to the bed.

During the visual inspection there were a number of events for which it was not immediately clear whether to regard them as rocking or as real pivoting events. From the seven events for which this severe doubt existed, four are also mapped on locations far from the dashed lines in the scatter plot of Figure 6.3, indicating that the classification procedure works well, fortifying the impression that both F_A and $\sigma_B(v)$ need to be raised in order to make the target stone pivot. These events are: 2, 10, 13 and 29. Furthermore, some of the rocking events almost coincide with a pivoting event, e.g. nrs. 6 and 25.

According to Figure 6.3, rather high values of F_A and $\sigma_B(v)$ occur quite often as they can also be found in the 0.5 Hz / 10 min measurement and even, although less frequent, in the 15 Hz / 20 s measurement. For the events that showed merely a rocking motion of the target stone the value F_A and $\sigma_B(v)$ are, on average, already somewhat higher and for the visually selected events they reach even higher values. This possibly indicates that the target stone was entrained by a common flow structure, or rather an extreme variant of a common combination of flow structures.

From the classification procedure we drew the preliminary conclusions that for entrainment of the target stone at the mean reattachment point, the longitudinal near-bed velocity needed to be higher than average and a large fluctuation of vertical velocity near the stone had to occur simultaneously. Presumably, two flow structures need to appear simultaneously: one creating the fluctuation of *v*-velocity (most probably a vortex) and one the high *u*-velocity. Most probably this combination of flow structures is very common, but at times of stone movement the combination is more intense, i.e. more capable of dislodging stones from their pockets. For a first verification of these preliminary conclusions we examined the conditionally averaged images as described in the next section.

6.4 Conditionally averaged flow

Before the conditionally averaged images are discussed it is brought to attention that in this section and the following, we maintained the colour-coding for velocities as described at the end of the previous chapter as far as the colours used for positive respectively negative velocities are concerned. This does not mean that all pictures have the same velocity scale! On average the start of the pivoting motion occurred halfway between two recordings. As a result, $i = -1$ (see §4.5.2) corresponds to 1/30 s before stone movement. We choose $t = 0$ as the start of the pivoting motion. Again the local co-ordinate system is used and, for brevity, the subscript *ci* (used for λ) is omitted.

6.4.1 Visually selected events

Decomposed velocity fields

The results of the conditional averaging procedure for the eight visually selected events are depicted in Figure 6.4. Each column of the figure shows a sequence of 3 images. At the left-hand side of the figure the conditionally averaged Reynolds decomposed horizontal velocities

are visualised by means of contour plots. In the pictures in the right column the accompanying conditionally averaged velocity fields in the vicinity of the target stone are displayed by means of Galilean decomposed vector plots. The velocities depicted by the vectors are Galilean decomposed velocities, obtained by subtracting 30% of the free stream velocity (= U_{max}) from the conditionally averaged velocities.

The Reynolds decomposing implies that for each point for which a velocity was known, the time-averaged *u*-velocity of that point was subtracted. This means that in Figure 6.4 in reddish areas the *u*-velocity is larger than it usually is in those areas and that in blue areas the *u*-velocity is less than it is on average at these locations. This does not mean that in reddish areas the *u*-velocity is necessarily larger than in blue areas.

When looking at the pictures in the left column from top down, it is clearly observable that a fluid package with large *u*-velocity arrives and that while it is advected to the right it moves towards the bed. When it arrives at the position of the target stone ($x = 0$) the stone is removed from its pocket. The longitudinal velocity close to the stone just before it starts to pivot is 0.25 m/s higher than on average.

The pictures in the right column show that this high momentum fluid package is accompanied by a clock-wise rotating vortex, of which the centre is marked by a capital "A" (depicted in the contour plots as well). The vortex and the fluid package with the increased *u*-velocity arrive at the target stone at more or less the same time and together they are able to move the stone from its position. Probably the vortex, which arrives a little sooner at the stone than the fluid package with the increased *u*-velocity, lifts the stone from the bed a little, increasing the area of the stone that is exposed to the longitudinal velocity, and the relatively large *u*-velocity that follows directly after the vortex drags the stone away. One can consult appendix J for a sequence of vector plots combined with contours of λ^2 that cover the complete measuring area.

Although the shapes of the structures are different, the sequence of a small area of upward directed fluid near the bed followed by a large-scale patch of downward moving fluid was also observed in the uniform flow experiments.

As the package of high *u*-velocity remains close to the vortex, both the package and the vortex must have had the same convection velocity. As $0.3U_0$ was subtracted from the conditionally averaged velocity field to reveal the vortex, the convection velocity is less than the velocity several authors found for the convection of large-scale structures in BFS flow, namely $0.6U_0$. This seems to be in agreement with the size, as judged by eye, of the diameter *d* of the vortex, which is much less than the water depth and therefore the vortex can probably not be considered a large-scale structure.[*]

About the size of the vortex in Figure 6.4 in relation to the size of the target stone, one can say that it seems capable to dislodge the target stone from its pocket (at least it is not too small or too far from the bed, see Chapter 2). Later on the scales of the structures responsible for entrainment are discussed some more.

Since the vortex is at first situated at some distance above the bed before it moves towards the bottom, it probably originates from the mixing or shear layer. This observation differs from what can be concluded from the uniform flow experiments. In these experiments the vortices related to entrainment were clearly to be associated with wall turbulence. High values of the swirling strength only occurred relatively close to the bed.

[*] In fact, it is not clear when to regard a vortex as large-scale. Scarano *et al*. (1999) for instance did not encounter vortices larger than $d / H \approx 0.44$ in their BFS flow experiments, see Chapter 2.

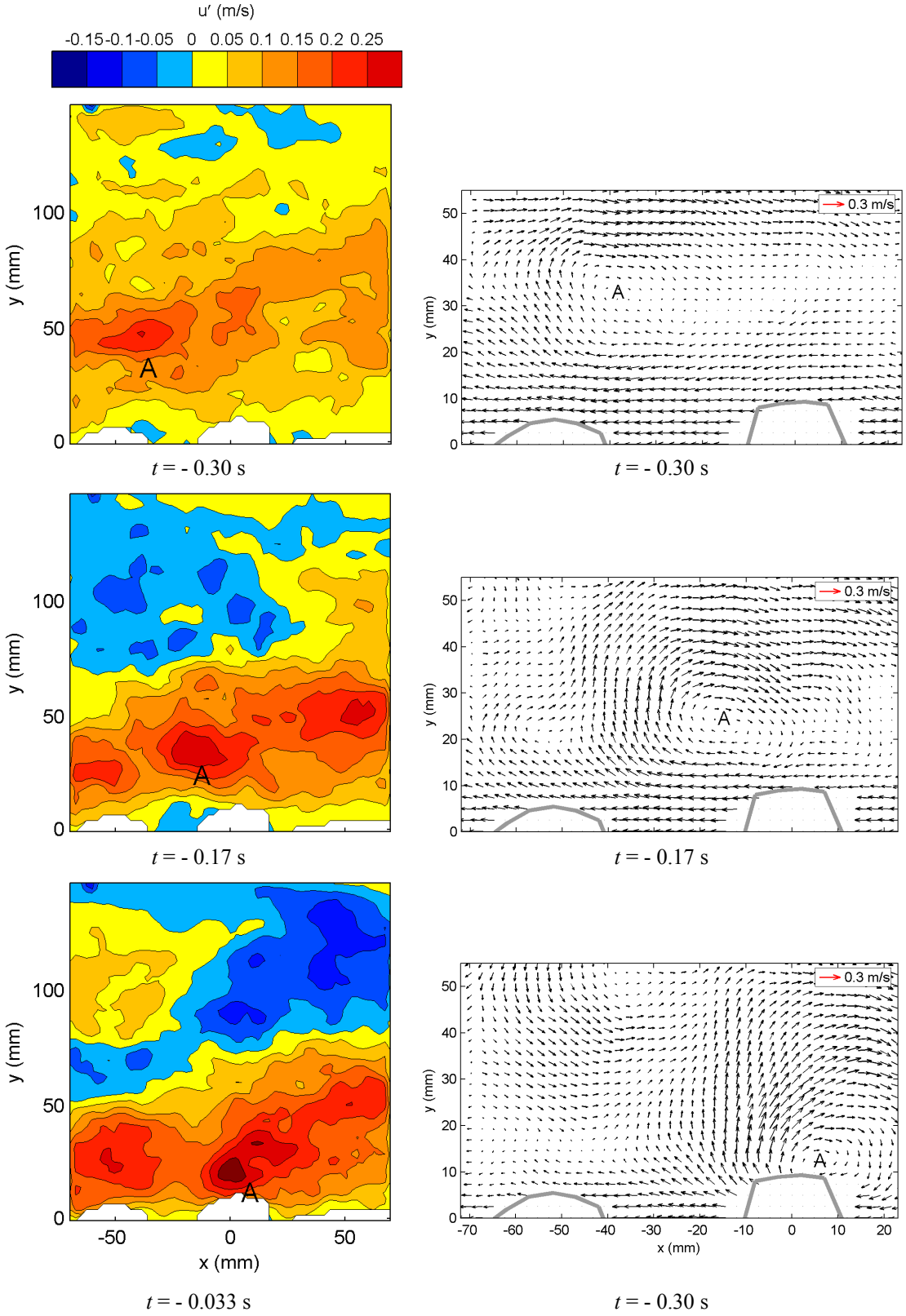

FIGURE 6.4 *Sequence of conditionally averaged flow fields of the visually selected events 5, 3 and 1 frame(s) before the target stone (located at x = 0) started to pivot. Left column: u'-contour plot. Right column: detail of Galilean decomposed ($u = u - 0.3U_0$, where $U_0 \approx 0.72$ m/s) vector plots. For clarity only one out of four vectors is shown; a 4 x 4 size filter was used to avoid aliasing. "A" denotes the centre of the vortex that can be observed.*

From the conditionally averaged pictures we can conclude that near the stone both an increased *u*-velocity and the presence of a vortex are required to move it. This is in agreement with what was found after performing the classification procedure. Obviously, we need to check if both structures that appear in the conditionally averaged pictures also appear in the instantaneous velocity fields around stone movement events. However, first the non-decomposed velocities around the points in time that the target stone moved are to be discussed.

Non-decomposed velocity fields

Non-decomposed velocity fields of the same points in time as the Reynolds decomposed velocity fields are depicted in Figure 6.5. The large deviation of the conditionally averaged fluid motion from the mean flow (as presented in the last section of the previous chapter) is apparent from both sequences in Figure 6.5. From the pictures that represent *u* it can be seen that the region with high *u*-velocity of the upper part from the flow starts to spread in downward direction and touches the stone at the moment just before the stone starts to pivot ($t = 0$).

The vortex that was observed in Figure 6.4, indicated by "A" again, is located in a fluid patch with a horizontal velocity of 0.2 – 0.3 m/s. This agrees with the velocity that was found before, namely $0.3U_0$ (= 0.3·0.72 m/s = 0.21 m/s). From the pictures that represent the vertical velocity, it is clearly discernible that a fluid package with a large upward directed velocity approaches the target stone and that, at the moment it arrives at the stone, the *v*-velocity reaches its maximum. The *v*-velocity pattern is in agreement with the presence of the clockwise-rotating vortex that is located directly downstream of the patch with positive vertical velocity. Moreover, this patch is surrounded by a region of large-scale negative *v*-velocity that transports the high *u*-velocity downward.

Moreover, during the whole time span the horizontal velocity near the water surface remains larger than the near-bed *u*-velocity. It can also be seen that when the velocity near the bed increases, the velocity near the surface becomes less (as the discharge was constant this seems logical). This is the reason that a large averaging area *A* in the classification process could not reveal the change in *u*-velocity near the bed.

As *v* near the stone is positive and v' is almost the same as *v*, and since from Figure 6.4 it is known that u' near the stone is positive, the flow just before entrainment can be classified as a Q1 event (outward interaction). Nelson et al. (1995) found, based on single-point velocity measurements, that Q1 events, although less common than Q4 events, individually are just as capable to move sediment from a bed as a Q4 event. Besides they discovered that near the step (including the reattachment zone) the most effective events to move sediment were Q1 events. They also stated that near the step the magnitude of the Q1 events is large, because of the large, low-frequency eddies, associated with flapping of the free shear layer and vortex shedding from the separation point that may cause them.

Although we dare say that the small-scale vortex observed in the conditionally averaged vector plots originates from the shear layer, it is not clear whether it can be associated with one of the quasi-periodic mechanisms that occur in BFS flow. Later on, in the last section of this chapter, the influence of the quasi-periodic mechanisms on entrainment is discussed.

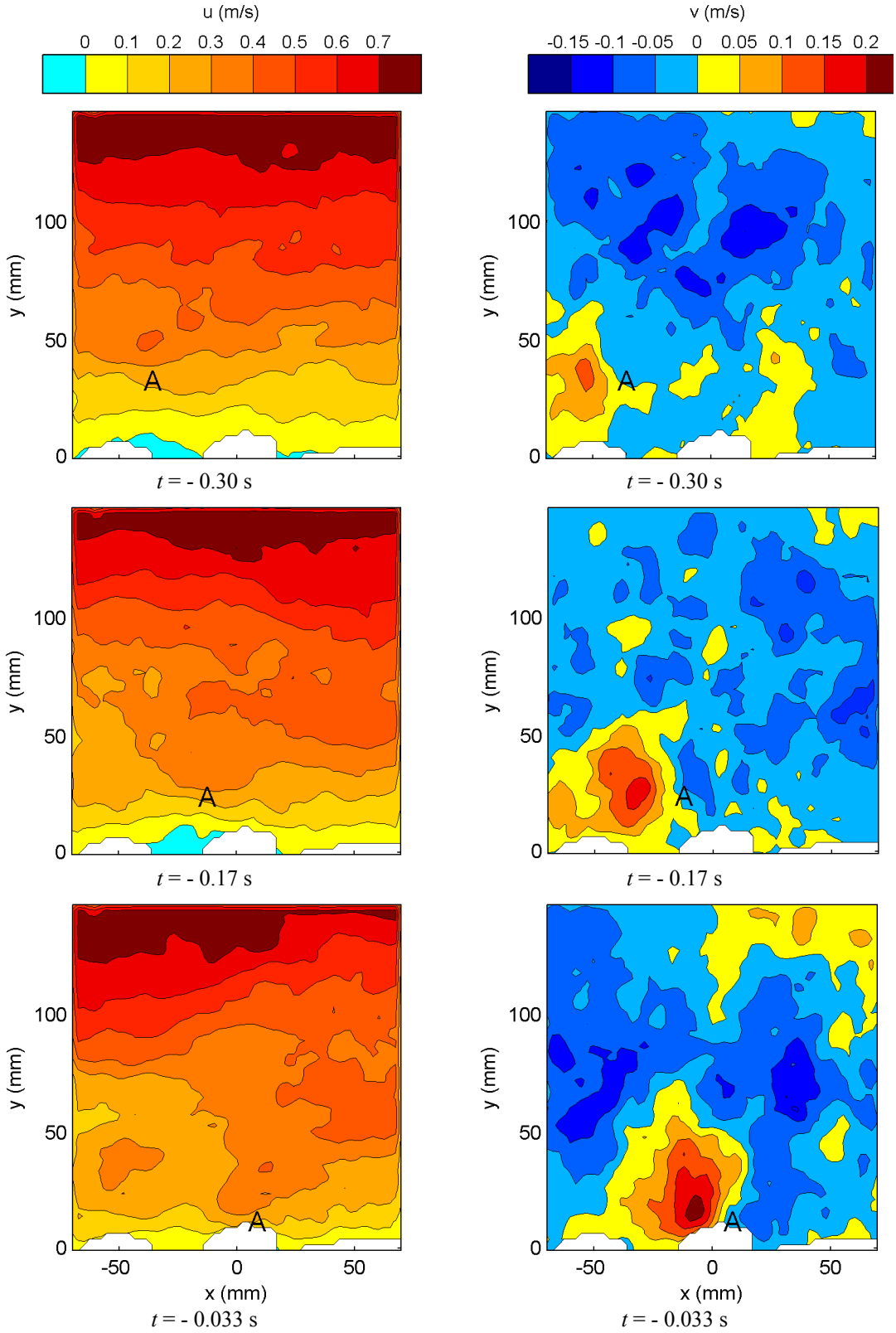

FIGURE 6.5 *Sequence of conditionally averaged flow fields of the visually selected events 5, 3 and 1 frame(s) before the target stone (located at x = 0) started to pivot. Left column: u-velocity. Right column: v-velocity. Note that the velocity scales of u and v are not equal. "A" indicates the centre of the vortex that can be observed in Figure 6.4.*

Large-scale spliced flow structure

To regard the flow responsible for entrainment at a larger scale than the measuring area, large-scale images were constructed using the splicing technique. For the visually selected events the conditionally averaged flow field is portrayed in Figure 6.6.

Since the flow considered here is far from uniform, the images represent the evolution of the flow in the measuring area in time, rather than a spatial reproduction of the flow at the time the target stone moved. To see the evolution in time, one must look at the pictures from right to left, as indicated by the arrow. The target stone moves at $x' = 0$. The prime denotes that the horizontal axis is both a length axis and a time axis. As a length axis it can be considered linear (that is why a length scale (in mm) is given) and both length scales (horizontal and vertical) are the same. However, as a time axis it is not linear. Although the time between to consecutive images used to construct the spliced images was always the same, the overlap of two consecutive images was not, as the convection velocity U_c of flow structures that produced distinctive flow patterns and hence large values of the correlation function, was always different. This implies that: the higher the average convection velocity, the longer the resulting spliced image. For conditional averaging the spliced images were aligned at $x' = 0$ and only the overlapping part of the images could be averaged. So, the shortest image determined the resulting length of the conditionally averaged spliced image, and it is not known what the total time span of such an image is. It is hard to interpret these conditionally averaged spliced images. Only a qualitatively impression of the flow around stone movement events can be gained. However, for a spliced image that represents a single stone movement event, the total time span is known.

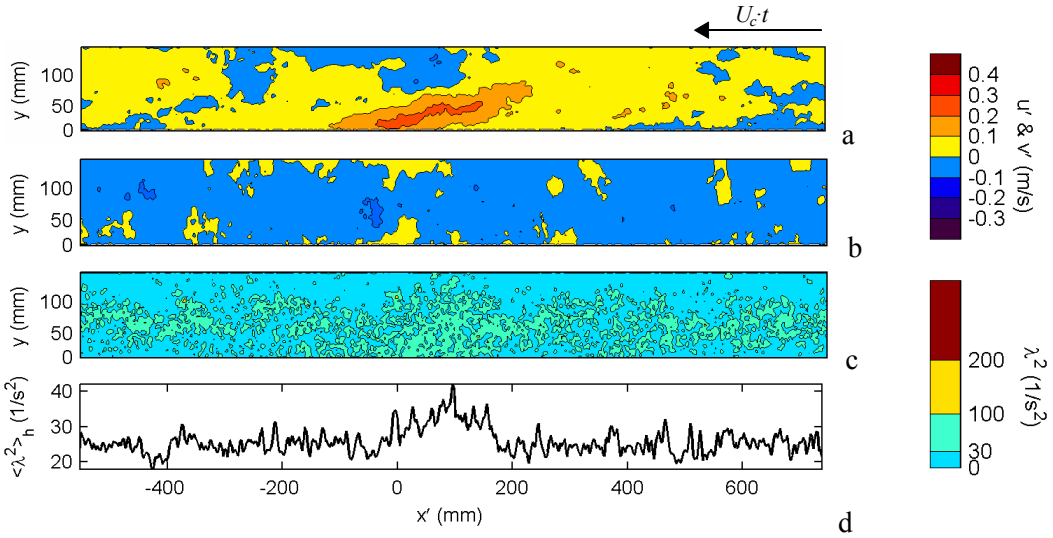

FIGURE 6.6 *Conditionally averaged spliced images. From top down: u', v', λ^2 and $<\lambda^2>_h$. To see the evolution in time one has to look at the pictures from right to left. Target stone moves at x' = 0.*

Figure 6.6a is in line with the sequence of conditionally averaged fields from Figure 6.4. Around stone movement the longitudinal velocity near the stone is high and the fluid package with relatively high velocities enters the region around the target stone at about $h/3$ to $h/2$ above the bed, with h being the local water depth. While migrating in downstream direction it moves towards the bed and after the stone has been dislodged the velocity near the bed stays high for a little longer. This is why the target stone stays up for a time and does not fall immediately back.

Figure 6.6b shows that the positive vertical velocity at the moment that the target stone is dislodged from the bed is only present in a small region around the stone and is surrounded by negative vertical velocity. From Figure 6.6a and Figure 6.6b combined we see that the small-scale patch of positive v is imbedded in a large-scale sweep or Q4 event. When looking at the small-scale structure while moving along with its translational velocity, as is done in the right column of Figure 6.4, the small-scale structure appear as a Q2 event. When both structures are superimposed, then the already mentioned Q1 event is the result. This is similar to what was observed in the uniform flow experiments.

From Figure 6.6c it is apparent that from a short time before the target stone is lifted up until a little after, a large area with relatively high values of the swirling strength λ^2 can be observed. The flow near the target stone seems to be more turbulent then at other times. The vortices appear to originate from the shear layer. In Figure 6.6c, apart from the region near $x' = 0$, the high values of λ^2 can be found at a distance above the bed and not close to the bed (as in uniform flow) or near the water surface.

From Figure 6.6d it can be seen that slightly before the moment of entrainment the depth averaged value of the swirling strength reaches a maximum value, confirming the pattern observed in Figure 6.6c. However the swirling strength near the bottom remains high until $x' = 0$. It would have been more useful to average the swirling strength over the lower part of the water depth.

Alltogether, the spliced flow fields seem to confirm that a small-scale vortex gives the target stone an initial lift and that next high u-velocity hauls it further away. Moreover, they show that the outward interaction or Q1 event that was observed before is a superposition of a large-scale sweep and a small-scale Q2 event imbedded within the sweep event. This was also observed in the spliced fields of the uniform flow experiments.

6.4.2 Rocking events

Also from the events during which the target stone not really pivoted, but just rocked in its pocket, conditionally averaged pictures have been made. In this section these images are described. As, for obvious reasons, they are of less relevance in the search for flow structures that cause entrainment than the visually selected events, the description is brief. They serve to discover differences and resemblances between both types of mentioned events. To make this feasible the same velocity scales are used as for the visually selected events for all types of visualisations (contour plots, vector plots etc.). This time only the pictures just before the start of the rocking motion of the target stone are given.

Decomposed velocity fields

Again we start with investigating the decomposed velocity fields (Figure 6.7). Both pictures show great similarities with those that can be found in Figure 6.4 (for t = -0.033s). Only this time the flow structures seem to be less intense: the u-velocity near the stone is less and the vertical upward directed velocity near the stone, at x = -10 mm, is less as well. The complete sequence of images can be found in appendix K and confirms this observation. The sequence of vector plots combined with contours of λ^2 that cover the complete measuring area, can be found in appendix J. Also from this appendix it becomes clear that the swirling strength near the stone is less than during the visually selected events.

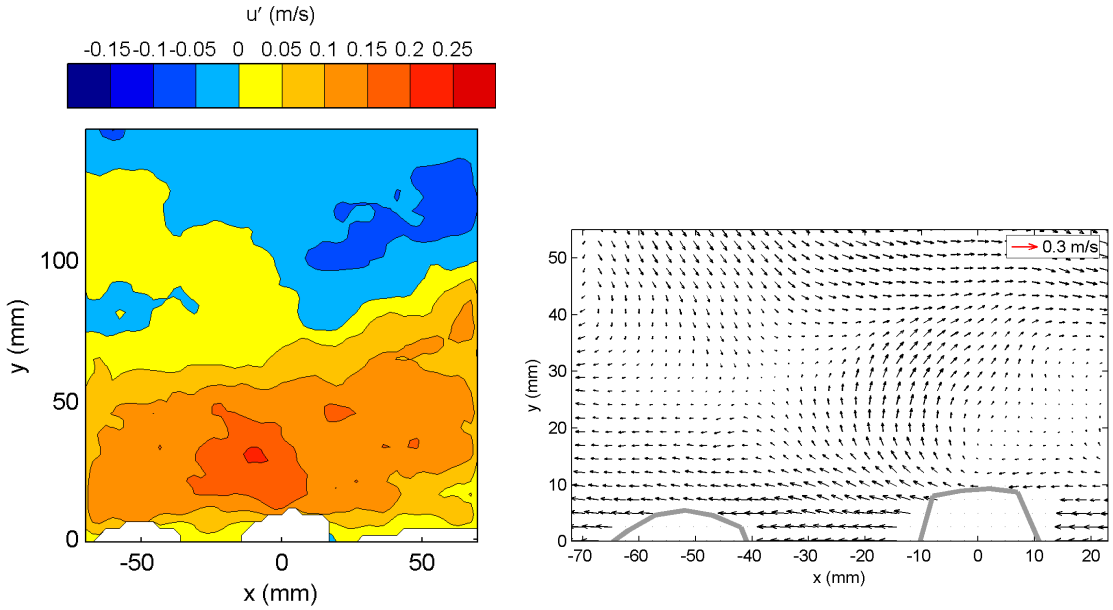

FIGURE 6.7 *Conditionally averaged flow field of the rocking events 1 frame (t = - 0.033s) before the target stone (located at x = 0) started to move. Left column: Reynolds decomposed u-velocity. Right column: Galilean decomposed (u = u - 0.3U$_0$) vector plot.*

Non-decomposed velocity fields

The non-decomposed conditionally averaged velocity field just before movement of the target stone are depicted in Figure 6.8. Also these flow fields show similar, but weaker structures than the non-decomposed velocity fields of the visually selected events. Water with high u-velocity is still transported to the bed, but the inflexion of the 0.3 and 0.4 m/s contour lines is much less. Evidently also the magnitude of the positive v-velocity is less. Besides, the patch of positive v-velocity is smaller than in the cases the target stone reaches a large pivoting angle.

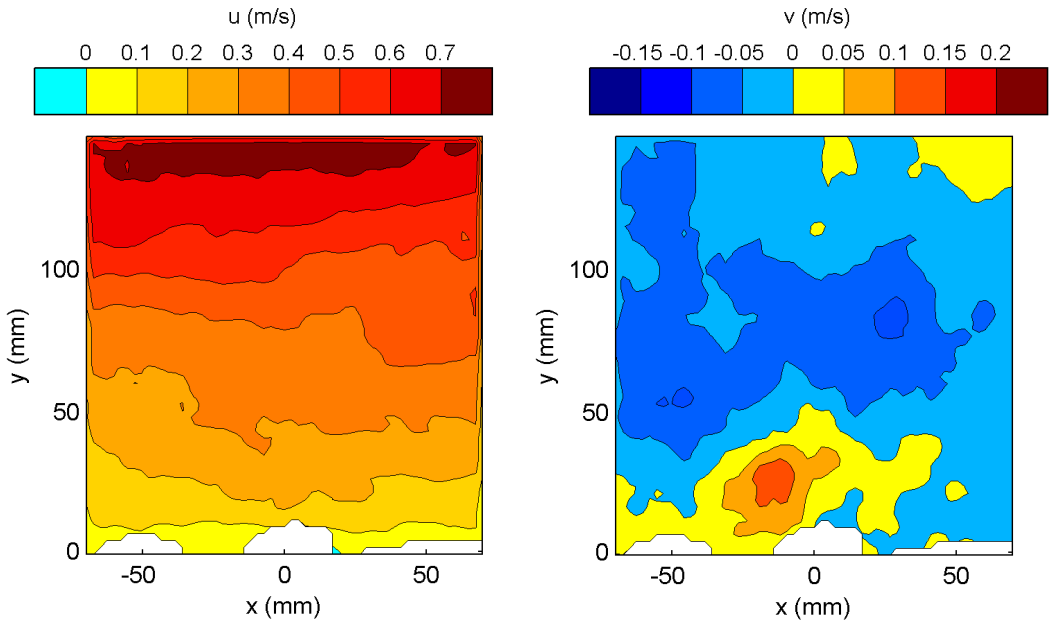

FIGURE 6.8 *Conditionally averaged flow field of the rocking events, 1 frame (t = -0.033s) before the target stone (located at x = 0) started to move. Left column: u-velocity. Right column: v-velocity.*

Large-scale spliced flow structure

Finally, Figure 6.9 shows the conditionally averaged, spliced flow field of the rocking events. These images corroborate the conclusion that the rocking events are brought about by the same, but weaker flow structures as the visually selected events. This might be a clue that entrainment in the reattachment is probably caused by an intense version of a common combination of structures. One may think that, as the number of rocking events (36) is significantly more than the number of visually selected events (8), the averaging procedure causes the structures to appear weaker. However, Figure 6.3 gives evidence that the structures are indeed weaker.

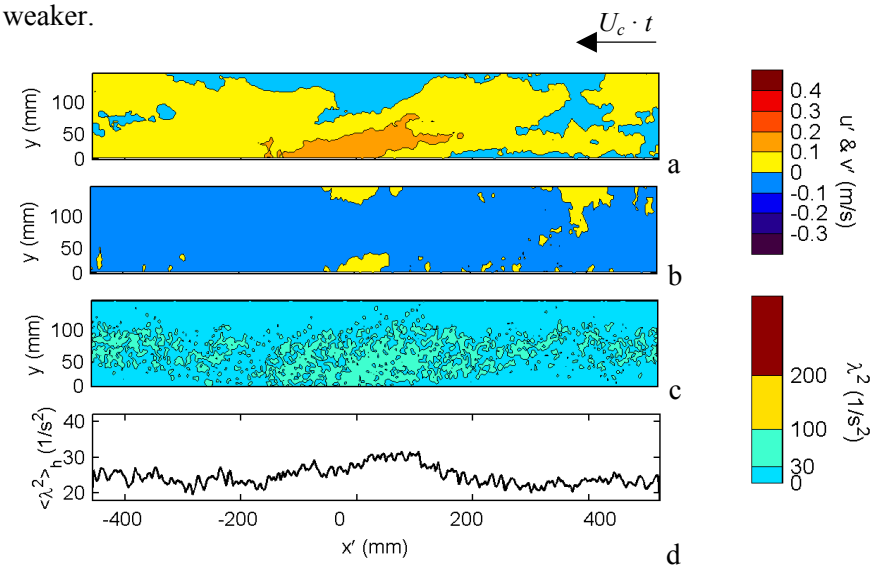

FIGURE 6.9 *Conditionally averaged spliced images of rocking events. From top down: u', v', λ^2 and $<\lambda^2>_h$. To see the evolution in time one has to look at the pictures from right to left. Target stone moves at x' = 0.*

6.5 Instantaneous flow

From the conditionally averaged flow we already have a good impression of the flow structures that occur at the times of entrainment. However, it needs to be checked if the instantaneous flow fields that caused stone movement resemble the conditionally averaged field and that the latter is not a hotchpotch of different kinds of instantaneous flow fields. For obvious reasons we cannot present all instantaneous flow fields of all events. Instead we choose to present just one arbitrarily chosen event of the visually selected events here. An overview of all these events in the form of large-scale spliced images can be found in appendix L.

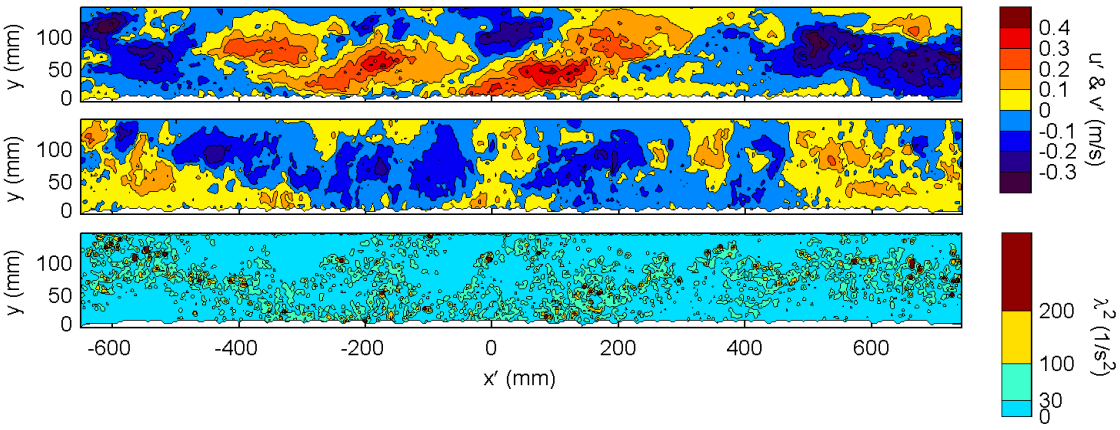

FIGURE 6.10 *Typical instantaneous spliced flow field (event 3). From top down: u', v' and λ^2. The stone moves at x' = 0. On average 100 mm corresponds to 0.2 s.*

Figure 6.10 shows the same flow structures as described when discussing the large-scale conditionally averaged spliced imagest. In appendix L it can be seen that most instantaneous flow fields are remarkably like the conditional average, indicating that the conditionally averaged field is truly representative for the flow that occurs around times of stone movement events and that both a large-scale sweep with a small-scale patch of upward directed fluid embedded within (a vortex near the stone) are required to entrain the target stone. A clear difference is that in the instantaneous flow fields the large-scale sweep is often much smaller than the one in the conditional average plot. This is probably caused by the jitter in the location of the structures, resulting in larger structures in the conditionally averaged pictures.

A striking feature is the evolution in time of the position of high swirling strength. High values of λ^2 can alternatively be found near the bottom and near the surface, indicating the presence of some kind of periodic mechanism. The influence of the known quasi-periodic mechanisms on entrainment in the reattachment region is discussed in the following section.

From Figure 5.7 it is known that the mean horizontal velocity near the bed is almost zero. From the upper plot of Figure 6.10 we can see that whenever positive *u*-velocity is present near the bed it is often very high, as it originates from the upper part of the flow (this downward movement of high *u*-velocity was already observed and can also be seen from the upper and middle plot of Figure 6.10 combined). This means that there have to be relatively long periods of negative *u*-velocity near the bed in order to get a mean horizontal near-bed velocity of zero. This is visible in the upper plot of Figure 6.10 (long stretches of blue areas directly above the bed). So the mean horizontal velocity plot in Figure 5.7 is tricky, lots of times the target stone may have been completely surrounded by negative horizontal velocity, indicating that it sometimes was well inside the recirculation bubble. Also this is checked in the next section.

6.6 Quasi-periodic mechanisms

The flow fields responsible for entrainment in the reattachment zone have been described in detail. For damage prediction of bed protections, for the design of turbulence models and for the development of a stability criterion, it would be very convenient to know what causes these flow fields. From the previous sections we already have some indications that they are related to the quasi-periodic mechanisms that occur in BFS flow: the fact that they seem to occur quite often (the rocking events are similar to the events that showed a pivoting motion of the target stone) and the evolution in time of the distribution of high values of the swirling strength over the depth. The quasi-periodic mechanisms of interest (vertical flapping of shear layer, oscillation of reattachment length and large-scale vortex shedding) are depicted in Figure 6.11.

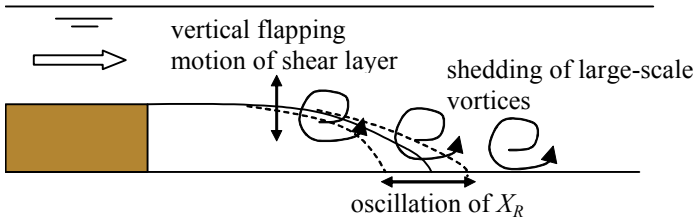

FIGURE 6.11 *Quasi-periodic mechanisms in BFS flow relevant for entrainment.*

To verify if entrainment of stones in the reattachment zone is in some way related to these quasi-periodic mechanisms we analysed the measured pressure signals, tried to discover if the conditionally averaged field perhaps occurred in a certain frequency and looked at the evolution in time of the flow field near the reattachment region. First an overview of the frequencies of the relevant different quasi-periodical mechanisms, see Chapter 2 and Figure 6.11, is given.

6.6.1 Previously reported frequencies of quasi-periodic mechanisms

With the step height H or the reattachment length X_R as length scale and the free stream velocity U_0 as velocity scale, the dimensionless frequencies (or Strouhal numbers) of the quasi-periodical mechanisms could be calculated. These were compared to the frequencies measured in previous investigations. As some authors used X_R and other used H to obtain dimensionless frequencies and we already showed that the ratio X_R / H is not constant, we could not simply substitute X_R by H (or vice versa) to verify if the expressions given by different authors yielded the same frequencies. Only if the authors gave values for X_R and H this was possible. This does not necessarily mean that the expressions are only valid for a certain ratio X_R / H. Maybe the mean reattachment length is the right choice to create dimensionless frequencies, perhaps the frequencies of quasi-periodic mechanisms depend only on the step height or possibly it is the ratio of X_R / H that determines the frequencies. Probably it depends on the mechanism considered.

An example: Lee & Sung (2002) found that $H = X_R$ / 7.4. If this is substituted in their expression for the frequency of the vertical, flapping motion of the shear layer, it yields the same expression as the one given by Simpson (1989). However, as we found that $X_R = 12H$, our frequencies calculated from both expressions by Lee & Sung (2002) for the flapping motion, one expressed in X_R and one in H, both yield a different frequency. An overview of the Strouhal numbers and the frequencies calculated from these numbers for the experiment considered here, is given in Table 6.1. Whenever a Strouhal number based on X_R is given for Lee & Sung (2002), it is calculated from their Strouhal number based on U_0 and their observation that $X_R = 7.4H$.

TABLE 6.1 *Overview of Strouhal numbers of quasi-periodic mechanisms related to BFS flow and the corresponding frequencies (f) for the present experiment based on H and either the measured value of U_0 or X_R.*

	(1) fH / U_0	(2) fX_R / U_0	(from 1) f (Hz)	(from 2) f (Hz)
Flapping of shear layer				
Lee & Sung (2002):	0.0136	0.1	0.15	0.09
Simpson (1989):	-	< 0.1	-	< 0.09
Shedding of large-scale vortices				
Lee & Sung (2002):	0.065	0.48	0.7	0.43
Oscillation of reattachment length				
Simpson (1989):	-	0.6–0.8	-	0.54–0.72

Hence, according to these values, the period of the flapping motion in our experiment could have ranged from 6.7 s to 11.1 s, the period of shedding of large-scale vortices from 1.4 s to 2.3 s and that of the oscillation of the reattachment length from 1.4 s to 1.9 s. From this it can be concluded that in the 15 Hz / 20 s measurement the oscillation of the reattachment length and the shedding of large-scale vortices must have occurred ca. 10 times, but the vertical flapping of the shear layer just once or twice. In the 0.5 Hz / 10 min. measurement the flapping motion must have occurred about 50 times.

Moreover we have strong indicatons to believe that the shedding of large-scale vortices and the oscillation of the reattachment length are related. Lee & Sung (2002) observed a more or less sawtooth shaped reattachment length time history, which is believed to be caused by a constant downstream movement of the reattachment position along with the growth of a large-scale structure followed by a sudden retreat of the reattachment position when the vortical structure detaches from the shear layer. Besides the frequencies of both mechanisms (see Table 6.1) have the same order of magnitude.

6.6.2 Evolution in time of flow near reattachment point

When discussing the pattern of the occurrence of vortices in the spliced plots that represented the flow around a single event, we already mentioned that there seemed to be some kind of repetitive motion visible. Also the 15 Hz / 20 s measurement was used to construct spliced images. These images give a good impression of the evolution in time of the flow near the mean reattachment point. The spliced image for the swirling strength is depicted in Figure 6.12. One can consult appendix M for the spliced images of the horizontal velocity, the vertical velocity and the Reynolds decomposed horizontal velocity.

Again it can be seen (Figure 6.12) that the locations with high values for the swirling strength λ^2 (locations with vortices) move up and down, as indicated by the dashed line. Alternately, high values of the swirling strength in the upper part of the water depth, up to the water surface, and high values of the swirling strength near the bed can be discerned. This pattern is in keeping with the presence of a quasi-periodic motion of some kind. Moreover, the swirling strength field deviates largely from that found for uniform flow. While in the results from the uniform flow experiments high values for λ^2 could be found near the bed (caused by the bed itself, e.g. hairpin vortex packages), they now appear over the entire water depth and originate from the shear layer. It is reminded that for each value of *x',* Figure 6.12 represents the flow near the reattachment point, so the shear layer is always close.

It can be seen in appendix M that the occurrence of high λ^2 values near the bottom is positively correlated to negative vertical velocities over the entire water depth and to high positive streamwise velocities near the bed. These sweeps ($u' > 0$, $v' < 0$) are clearly observable at x' = 200, 800, 1800, 2700, 5300, 5900, 6600, 7200, (8000) and 9200 mm. At these points in time the swirling strength near the bed is high, as vortices originating from the

shear layer are transported by the sweep event towards the bed (in Figure 6.12 one can see that vortices arrive from a distance well above the bed, before impinging on the bottom).

As the flow considered here is the flow in the reattachment region, it seem logical to assume that the sweep events are caused by a temporary decrease of the reattachment length. When the recirculation bubble retreats towards the step, it allows the high *u*-velocity from the upper part of the flow to move toward the bed. An inspection of Figure M.1, which shows the evolution in time of the non-decomposed horizontal velocity in the reattachment region, seems to confirm this supposition: negative velocities near the bed occur before each sweep event, indicating that at these times the recirculation bubble is still present in the measuring area.

As we observed ca. 10 sweep events in 20 s of flow, the average frequency of these events is 0.5 Hz. This is only slightly less than the frequency calculated from the Strouhal number given by Simpson (1989) for the oscillation of the reattachment length.

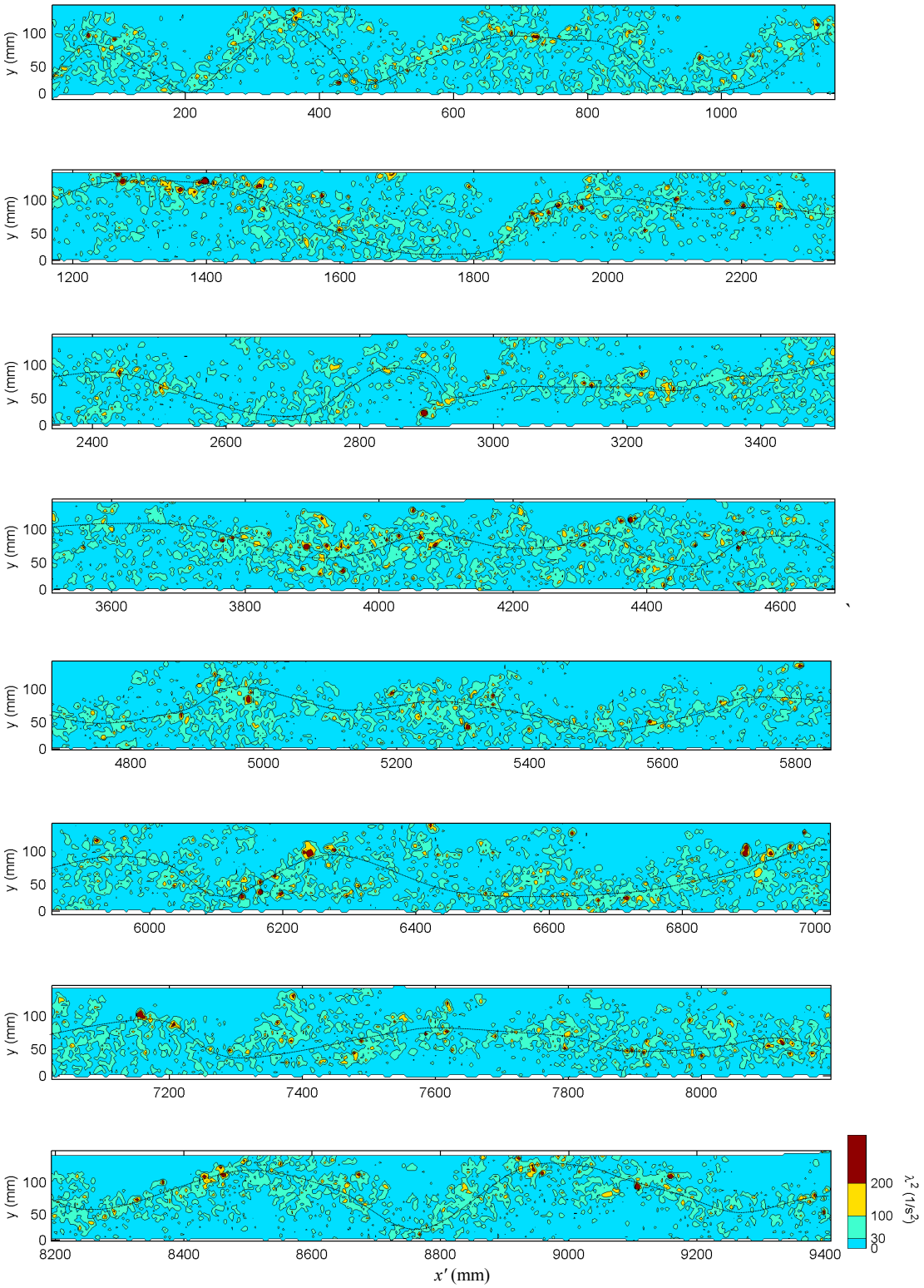

FIGURE 6.12 *Evolution in time of the swirling strength near the reattachment zone. Spliced image based on 15 Hz / 20 s measurement. For the evolution in time one must start looking at the series in the lower right-hand corner and look from right to left (100 mm ≈ 0.2 s).*

As $Fr_1 \approx 0.55$, an oscillation of the standing wave that occurred, might also have influenced the flow slightly, although the pressures caused by it most probably did not influence the pressures near the bed as they decrease rapidly in vertical direction. Moreover, the frequency of oscillation must have been much lower than that of the repetitive pattern observed in Figure 6.12, as it was not observable by eye.

The time between two consecutive recordings of the 0.5 Hz / 10 min measurement was too long to construct spliced images and could not be used to verify if a low-frequency flapping motion was present.

6.6.3 Spectral analysis of pressures

As already mentioned, pressures were measured simultaneously with the PIV measurements with a sample frequency of 500 Hz. We analysed these signals to see whether the quasi-periodic mechanisms associated with BFS flow were also present in our experiments, and to compare them with pressure measurements of other authors.

Before doing so, we emphasize that the reattachment process gives rise to a multitude of events with different frequency compositions, rather than a unique predetermined one. However, Simpson (1989) states that the maximum energy content of wall pressure fluctuations occurs at the frequency of the oscillation of the reattachment length, while Lee & Sung (2002) provide evidence that the pressure fluctuations on the bottom are mainly due to the vortical structure in the shear layer. They also state that there is a relation between the low-frequency pressure oscillations and the periodic enlargement/shrinkage motion of the separation bubble.

Spectra of pressures

Figure 6.13 shows the power spectrum of the pressures measured by the pressure transducers L1, L3 and D1 (see Figure 3.5 for the positions). To enable to compare our results with the smooth wall wind tunnel experiments of Lee & Sung (2002), the frequency has been normalised by the step height and the free stream velocity U_0 (= U_{max}) and the spectral density has been made dimensionless by a combination of the free stream velocity and the fluid density. The reference signal from the transducer that was positioned in the cavity below the measuring area has been used to correct for high frequency environmental noise.

We compare our measurements to pressures measured by Lee & Sung (2002) at $x / H = 10$ and at $x / H = 8$. The former because that is close to the reattachment length we found ($X_R / H = 12$), and the latter, because it is close to the reattachment length Lee & Sung (2002) found ($X_R / H = 7.4$). The present measurements coincide best with the line representing the pressures measured by Lee & Sung (2002) at $X_R / H = 8$. The wall pressure spectra of these two experiments show large similarities. The maximum value, the frequency at which the maximum value occurs and the high frequency slope of the spectra collapse nearly completely.

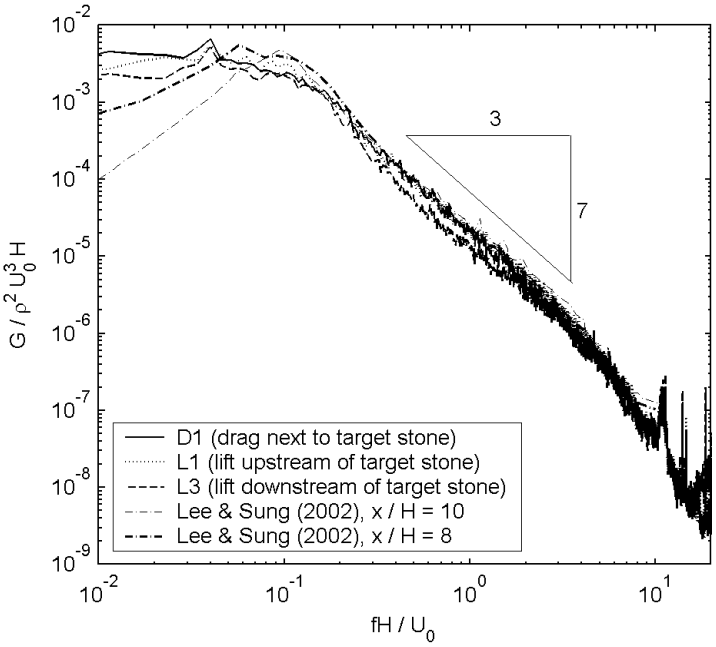

FIGURE 6.13 *Spectra of the pressures measured by the pressure transducers L1, L3, and D1 during experiment B006 (x / H ≈ 12) compared to spectra by Lee & Sung (2002).*

Moreover, the resemblance of all our three spectra with Lee & Sung (2002) confirms what was already suspected in chapter 2, namely that the pressures on the bottom wall are mainly due to the outer flow and not caused by the roughness of the bed or the shape of the bed elements. Hofland *et al.* (submc) already suggested this when they found the same pressure distribution on a cube in a rough bottom wall downstream of a BFS as Lee & Sung (2002) found on a smooth wall. However, some doubts remained as the suggestion was based on pressure measurements on a cubical bed element. Now that it has been shown that pressures on naturally shaped stones also yield the same pressure distribution, we dare say that TWP are indeed caused by the overall flow configuration. The drag sensor shows a similar spectrum as well, which means that the stones are not protruding enough for the QSF to give a large force contribution and that the TWP are dominant. Moreover, the slope of -3/7 is attributed to the turbulence term in homogeneous turbulence in a free shear flow (George *et. al*, 1984).

From Figure 6.13 it is hard to see if there are frequencies that can be associated with the quasi-periodical mechanisms. A semi-logarithmic plot, as depicted in Figure 6.14 is more suitable for this purpose. Again dimensionless values have been plotted. To preserve the variance of the pressures the spectra have been premultiplied by *f*.

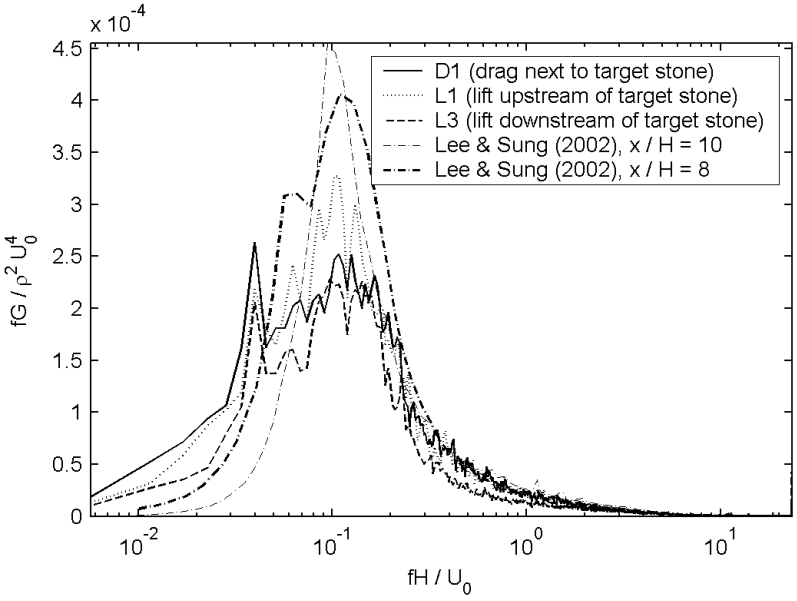

FIGURE 6.14 *Premultiplied, variance preserving spectra of pressures measured by the pressure transducers L1, L3, and D1 during experiment B006 ($x / H \approx 12$).*

All measured signals show a peak at $fH / U_0 \approx 0.1$. Although the spectra coincide with the spectra obtained from Lee & Sung (2002), the density at the peak is less. Lee & Sung (2002) found this peak for pressures measured at several cross-sections and attributed it to the multitude of events with different frequency compositions. For the present measurements the peak corresponds to a frequency of 1 Hz. This does not coincide with one of the frequencies in Table 6.1.*

In the three signals from pressure transducers L1, L3 and D1 a second, less high, but more distinctive peak is located at $fH / U_0 \approx 0.04$ (this peak became significant after using the reference pressure sensor for noise reduction). This corresponds to a frequency of 0.43 Hz. This more or less coincides with the frequency found for the swirling strength oscillation as seen in Figure 6.12. This oscillation, in turn, was suggested to be related to the oscillation of the reattachment length. However, 0.43 Hz is slightly less than the value found for the oscillation of the reattachment length in Table 6.1, but does coincide with the frequency of the shedding of large-scale vortices.

As a second, smaller peak is also observable in the line representing the pressures measured by Lee & Sung (2002) at $x / H = 8$ and not in $x / H = 10$, it may indeed be related to a phenomenon occurring only in the reattachment zone. If instead of H, X_R would have been used for normalising, then the smaller peak observed in the line representing the pressures measured by Lee & Sung (2002) at $x / H = 8$ and the peaks in the spectra from transducers L1, L3 and D1 would have coincided.

Lee & Sung (2002) did not present a cause for the smaller peak found in their spectrum, although it does appear at the dimensionless frequency they found for the shedding of large-scale vortices, Table 6.1.

* Maybe the burst frequency upstream of the step ($f = U_0 / (5h_1) \approx 1.2$ Hz) influences the frequency found; as it has the same order of magnitude. However, we did not investigate this any further.

Summary
All together we conclude that our pressures are in agreement with those measured by Lee & Sung (2002), that TWP are governed by the overall flow configuration and that they are not significantly influenced by the wall roughness. As TWP are very much the same for different cross-sections, they might be caused by large-scale vortices. As downstream of the reattachment zone the peak coherent vorticity of vortices decays slowly while being convected downstream (Scarano *et al.*, 1999), the TWP at different cross-sections remain more or less the same.

In the pressure spectra near the reattachment zone, two significant peaks appear. The cause of the frequencies with higher energy content is not incontrovertibly clear, although it seem that the oscillation of the reattachment length plays a large role. The peaks do confirm that more than one quasi-periodic mechanism was present. The corresponding frequencies have the same order of magnitude as those found in literature. From the analysis of the pressures alone, it is not clear which quasi-periodic mechanism causes entrainment in the reattachment zone.

6.6.4 Occurrence of flow field responsible for entrainment

If the flow structure responsible for entrainment in the reattachment zone, namely the conditionally averaged flow field, turns out to occur periodically, then this field is most probably caused by one of the quasi-periodic mechanisms. To verify this we compared the conditionally averaged flow field, the field at t = - 0.033 s obtained from the visually selected events, to each flow field of the 15 Hz / 20 s measurement and checked if they were more or less similar by using the normalised covariance function that was used before to construct the spliced images, and that for completeness sake is reproduced her again:

$$\rho = \frac{\left\langle u'_A u'_B \right\rangle_{ma}}{\sqrt{\left\langle u'^2_A \right\rangle_{ma} \left\langle u'^2_B \right\rangle_{ma}}} \tag{6.1}$$

In this equation the subscript *ma* stands for *measuring area*, and *A* and *B* for respectively the conditionally averaged stone moving flow field and an arbitrarly chosen field of the 15 Hz / 20 s measurement.

Eq. (6.1) yields a high value if both fields are very much alike (the function yields 1 if both fields are identical). The output is largely influenced by large-scale flow structures. Obviously the chance of finding a field that was exactly the same as the conditionally averaged field was small, after all the mobility conditions were low. However, the fields did not need to be completely similar. A quasi-periodic occurrence of a field less distinctive or less powerful (less capable of moving stones), but with similar features as the conditionally averaged field, would also indicate the presence of a quasi-periodic mechanism.

The procedure described above yielded the time signal of the adapted, 2-D normalised covariance function correlation (indicated here by ρ) as depicted in Figure 6.15.

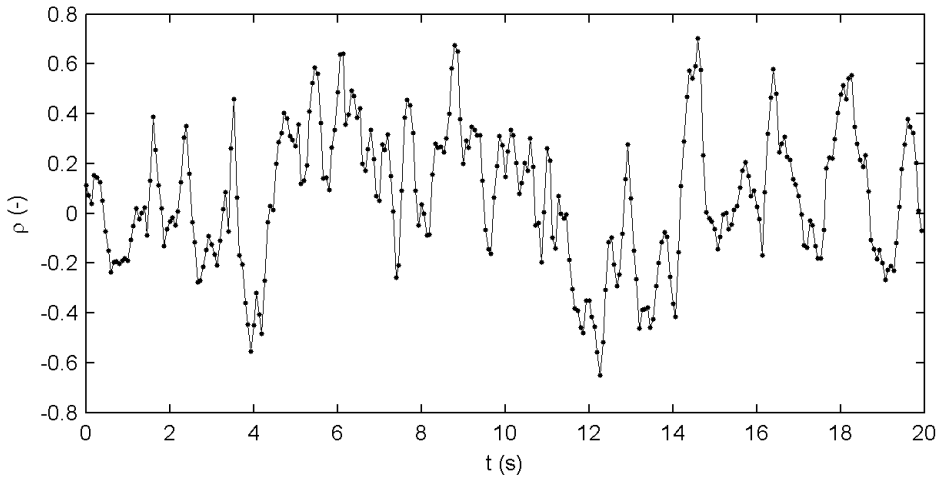

FIGURE 6.15 *Time signal of the 2-D, normalised covariance function when used to compare the conditionally averaged flow field to 20 seconds of flow.*

The signal shows some distinctive peaks with values of ρ up to 0.7, indicating that in merely 20 seconds of flow sometimes the flow field resembled the conditionally averaged flow field very well. The fact that each peak consists of several data points excludes white noise, but means that we are dealing here with a time-resolved signal. Furthermore it implies that the flow resembled the conditionally averaged flow for several frames, indicating that the repetitive structure is larger than the measuring area or has a slow convection velocity.

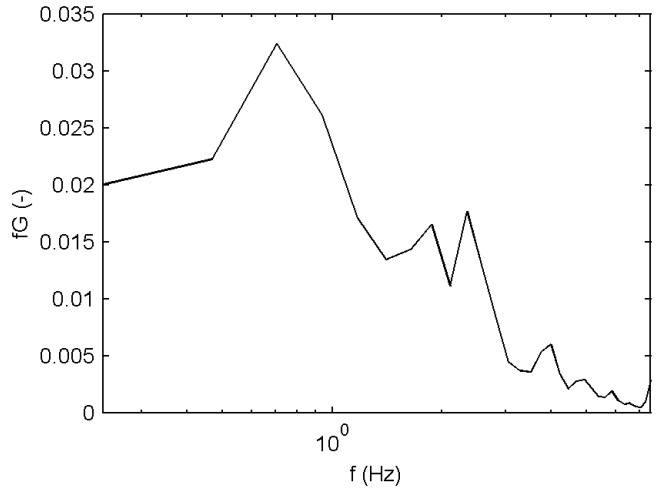

FIGURE 6.16 *Premultplied, variance preserving spectrum of the signal obtained from the 2-D, normalised covariance function used to compare the conditionally averaged flow field and 20 seconds of flow.*

From Figure 6.15 it is hard to tell if there is a dominant frequency. Therefore we consider the the spectrum of ρ premultiplied by the frequency f, see Figure 6.16. From this figure it may be concluded that the frequency of the occurrence of a field that resembles the conditionally averaged flow field is ca. 0.7 Hz, corresponding to a period of 1.4 s. This seems in agreement with the time between two consecutive peaks in Figure 6.15, especially for the peaks at the right-hand side of the figure. Moreover, this frequency is associated with the shedding of

large-scale vortices (Lee & Sung (2002)). However, 20 s is very short to check whether a mechanism with a period of 1.4 s occurs and hence the reliability of the frequency found is low.

The same procedure was applied to the 0.5 Hz / 10 min measurement, but as 0.5 Hz is less than the frequency obtained above (0.7 Hz) and also less than most frequencies listed in Table 6.1, it could only be used to check if it was the flapping motion of the shear layer that created the conditionally averaged flow field. However, from this analysis we found no evidence that confirmed this; most probably the sample frequency was too low.

Summary
As the whole field was correlated to obtain ρ, the correlation only reveals the presence of the large-scale structure of the conditionally averaged stone-moving structure. A small scale eddy does not influence the large-scale u-velocity field much. So from Figure 6.15 we know that the large-scale stone moving structure is often recurring ($f \approx 0.7$ Hz). The question remains, is the structure that removes the stone (and which occurs much less frequent than 1/0.7 s) an extreme value of the often recurring large-scale structure or an accidental combination of the large-scale structure and a specific small-scale structure near the stone.

7 CONCLUSIONS AND RECOMMENDATIONS

7.1 Introduction

In this last chapter the conclusions that were deduced throughout this report are summarised. From these conclusions one can determine to what extent the objective, being "the determination of the influence of turbulence structures on the stability of stones in the top layer of a granular filter downstream of a backward-facing step", has been fulfilled.

Some recommendations for further research on the topic of stability of stones in a bed downstream of a BFS are given. These recommendations include remarks for those planning to conduct new experiments and some suggestions for additional analysis of the data collected during the experiments described in the foregoing chapters.

7.2 Summary of how data was collected

Before the main conclusions of the experiments are given, some aspects of the experimental set-up and procedure relevant for the interpretation of the results are briefly summarised

- Aspect ratio $b/h = 2.7$.
- An artificial stone ($\Delta = 0.3$) was used to establish that initial stone movement occurred in the measuring area. This stone was attached to a hinge that only allowed a pivoting motion in the mean streamwise direction.
- Low-mobility conditions were investigated.
- 2-D PIV measurements were conducted in centre line of flume.
- Mean flow quantities were deduced from 0.5 Hz / 10 min measurements.
- Flow during entrainment was recorded with a frequency of 15 Hz ($fH/U_0 \approx 1.4$).
- Spatial resolution of PIV measurements: 1.2 mm x 1.2 mm (Δx x Δy); $d_{n50} / \Delta x \approx 15$.
- Pressures were measured (sample frequency 500 Hz) by means of transducers that were mounted inside some artificial stones in the bed.

7.3 Conclusions

7.3.1 Mean flow

From the time averaged flow fields of the experiments that were conducted at different distances downstream of the BFS, the main topological features of BFS flow (as e.g. observed previously by Nakagawa & Nezu, 1987) were readily recognised: the recirculation bubble separated from the high momentum flow near the water surface by the mixing layer, the high turbulence intensities in the mixing layer and the slow relaxation of the profiles of u-velocity towards a log-law profile in the downstream direction. However, some differences with experimental results of other researchers were encountered as well. These differences, together with some other observations of the mean flow pattern are listed below.

- The mean reattachment length X_R was found to be longer than the length generally found in open-channel flow, namely $X_R \approx 12H$ versus $X_R \approx 6$–$8H$. A brief analysis of mean reattachment lengths observed by different authors showed that an increase of the Froude number downstream of the BFS leads to larger reattachment lengths. Furthermore, it seems that experiments conducted with a rough bed downstream of the BFS have larger reattachment lengths than those conducted with smooth walls. (A limited width of a test facility may also cause a relatively large reattachment length.)

- The longitudinal velocity near the bed at the reattachment point has a strongly positively skewed probability distribution.
- The depth averaged relative turbulence intensity downstream of the reattachment point is in agreement with the formula proposed by Hoffmans (1993), provided that U_0 ($\approx U_{max}$) is used for normalising the measured intensities.

7.3.2 Turbulence structures and entrainment

We deduced the following conclusions from the observations of the flow around an entrained stone in the reattachment region and its movement frequency:

- The time between stone movements in the reattachment region is distributed exponentially. This knowledge may be very helpful when creating a model that links flow conditions to bed damage.
- The stone was only detached from the bed as long as the structures responsible for entrainment were present. The average flow was too weak to keep the stone up once these structures had passed.
- During both the pivoting and the rocking events the flow turned out to be similar save for the fact that during the rocking events the flow structures that were present were less intense, i.e. less capable of entraining the target stone.
- Both force generating mechanisms (QSF and TWP) needed to be present to dislodge the stone from its original position. Also in the results from the uniform flow experiments this was observed. However, then at least one mechanism was usually extremely strong and the events could be divided into events mainly caused by TWP and events mainly caused by QSF, while in the experiments discussed here usually both mechanisms were strong and no such distinction could be made. Moreover, this procedure showed that during the pivoting events the force generating mechanisms were more intense than during the rocking events and that during the rocking events both the QSF and the TWP were already larger than they were on average.
- The flow in the vicinity of the target stone responsible for entrainment can be classified as a Q1 event (outward interaction). Nelson *et al*. (1995) already found that Q1 events are well capable of transporting sediment from the bed and that they, together with Q4 events, are responsible for the majority of sediment transport. Moreover, they found that just downstream of the reattachment region most of the sediment is transported by Q1 events.
- A closer look learned that the Q1 event is in fact a large-scale sweep or Q4 event with a small-scale Q2 event imbedded. The superposition of both flow structures results in the Q1 event. Since the results of Nelson *et al.* (1995) are based on single point LDA measurements, they could not reveal this. The same superposition of flow structures was also observed in the uniform flow experiments.
- Right before the target stone moved, a vortex was present just above the stone. The small-scale Q2 event is probably caused by this vortex.
- The vortex, in turn, originates from the shear layer. It clearly arrives from a distance well above the bed, while in the results from the uniform flow experiments it was observed that the vortices causing entrainment were related to wall turbulence.
- As the vortex arrives at the stone a little sooner than the patch of high u-velocity (the sweep), the vortex probably lifts the stone slightly out of its pocket and hence increases the area of the stone exposed to the longitudinal velocity, before the increased longitudinal velocity can haul the stone away.

Furthermore we conclude that entrainment of stones in the reattachment region is caused by an extreme variant of a combination of flow structures that occurs more often than just during

entrainment. This is based on the fact that the combination also occurred at times when there was no real stone movement, namely during the rocking events.

It is emphasised that, although the origin of the structures responsible for entrainment in uniform flow is completely different from their origin in BFS flow, the flow fields in both types of flow around moments in time that entrainment occurred, are remarkably similar. Especially the small-scale flow structures are alike. Also the order of the stone moving structures (small-scale vortex followed by large-scale sweep) is the same.

7.3.3 Quasi-periodic mechanisms

Again the conclusions given in this section are only valid for the region around the mean reattachment point.

We searched whether quasi-periodic mechanisms were present with the same frequencies as found in literature for the oscillation of the reattachment point and for the shedding of large-scale vortices from the shear layer. Also the influence of a third mechanism, namely the vertical flapping motion of the shear layer, was included in the investigation.

In literature we found the dimensionless frequencies of the oscillation of the reattachment point ($fX_R/U_0 \approx 0.6$–0.8; Simpson, 1989) and that of the shedding of large-scale vortices ($fH/U_0 \approx 0.065$ or $fX_R/U_0 \approx 0.48$; Lee & Sung, 2002) Probably both mechanisms are related.

We obtained the following frequencies from different measurements:

- Looking at the evolution in time of 20 s of flow in the reattachment region revealed a quasi-periodic motion of the location of high values of the swirling strength. Alternately, high values of the swirling strength in the upper part of the water depth, up to the water surface, and high values of the swirling strength near the bed could be discerned. The occurrence of high λ^2 values near the bottom is positively correlated to negative vertical velocities over the entire water depth and to high positive streamwise velocities near the bed (sweeps transport vortices towards the bed). The frequency of this motion is about 0.5 Hz ($fH/U_0 \approx 0.05$, $fX_R/U_0 \approx 0.6$).
- A spectral analysis of the measured pressures (lift as well as drag) revealed two significant peak frequencies, one at $f \approx 1$ Hz ($fH/U_0 \approx 0.1$, $fX_R/U_0 \approx 1.1$) and one at $f \approx 0.43$ Hz ($fH/U_0 \approx 0.04$, $fX_R/U_0 \approx 0.5$).
- By comparing the conditionally averaged flow field to 300 PIV recordings (20 s of flow) we found that a large-scale structure similar to the large-scale structure that is present during entrainment (the sweep), occurs with a frequency of $f \approx 0.7$ Hz ($fH/U_0 \approx 0.07$, $fX_R/U_0 \approx 0.78$).

All the observed frequencies, save the peak at $f \approx 1$ Hz in the pressure spectra, have the same order of magnitude and more or less coincide with those found for the oscillation of the reattachment point and large-scale vortex shedding. The peak in the pressure spectra at $f \approx 1$ Hz is generally (e.g. Lee & Sung, 2002; Simpson, 1989) attributed to a multitude of events with different frequency compositions.

From the above we deduced the following model: the large-scale sweep or Q4 event that occurs when stones are entrained from the reattachment region, and which is frequently observed, is related to the oscillation of the reattachment position. When the recirculation bubble retreats it allows the high momentum fluid from the upper part of the flow to reach the bed (a sweep), increasing the QSF on the stones. The sweep transports vortices from the shear layer toward the bed, yielding an ideal sequence of structures to dislodge a stone from its pocket: first a vortex lifts the stone slightly up, and subsequently the increased horizontal velocity together with the increased area of the stone that is exposed to this high momentum fluid, hauls the stone further away.

We cannot express an opinion about the influence of the vertical flapping motion of the shear layer. The durations and frequencies of the PIV recordings did not allow investigating the influence of this mechanism in a sufficient way.

7.3.4 Pressures on the bed

Some additional results from the pressure measurements are:

- The pressures on the bottom wall are mainly due to the outer flow and not caused by the roughness of the bed or the shape of the bed elements. This is based on the fact that the measured pressure spectra collapsed with spectra measured in smooth wall BFS experiments.
- Both the pressures measured by the drag sensor and those measured by lift sensors showed a similar spectrum. This indicates that the stones were not protruding enough for the QSF to give a large force contribution and that the TWP were dominant.

7.4 Recommendations

7.4.1 Analysing the collected data

A lot more data were collected than analysed in this report. Especially the data collected during the experiment conducted somewhat downstream of the reattachment region (B009) is interesting. This experiment can be analysed as was done in this report for the experiment near the mean reattachment point. Suggestions for further analysis of the collected data are given below.

- Constructing streamline plots may reveal the influence of the flapping motion and the oscillation of the reattachment length on the entrainment of stones (some more).
- It needs to be checked if the times that λ^2 near the bottom is high coincide with the times that the correlation signal in Figure 6.14 has a high value.
- The signals from the pressure transducers at times that stone movement occurred could be analysed. These pressures can be conditionally averaged as was done with the PIV recordings. If vortices are responsible for entrainment, then large negative pressures need to be present. Obviously also the influence of large drag forces can be established.
- By constructing the conditionally averaged velocity field of the fields corresponding to the peaks of the normalised cross-covariance function in Figure 6.15 and to compare this field to the conditionally averaged stone moving field, the difference between both fields can be established. Probably the conditionally averaged stone moving field contains a small-scale structure that lacks in the conditionally averaged velocity field of the fields corresponding to the peaks of the normalised cross-covariance function.
- Perhaps the classification procedure discriminates stone movement events from average flow better when the area for which an indication of the magnitude of the TWP is determined is very small. The exact location of the vortex is probably very important when it comes to entrainment.

7.4.2 Suggestions for new experiments

The most important question that remained unanswered is: what is the influence of the flapping motion on entrainment? To answer this question, PIV recordings need to be long enough to include several flapping periods. At the other hand, the sample frequency needs to be large enough to capture all relevant flow phenomena. A larger storage capacity for the PIV recordings is desired. If this is not an option then we recommend to measure with the

following frequency: $fH/U_0 \approx 0.35$. Then about seven flapping periods will be present in a measurement with a maximum possible duration and the sample frequency is probably still high enough to see flow structures on about three or four successive recordings.

Other adaptations that are useful, but that sometimes require other equipment, are listed below.

- A larger ratio of h/d_{n50} and H/d_{n50} will have the advantage that the experiments will resemble reality some more and that the vortices that are shed from the shear layer are significantly larger than the vortices generated by the bed. This makes it easier to discriminate both types of vortices and to investigate the influence of both of them on entrainment. In the present experimental set-up this is only possible by using smaller stones, increasing h or H is not possible (aspect ratio would become very small; Froude numbers would become too large).

  Smaller stones also move sooner than larger ones and hence flow velocities can be lower. So experiments can be conducted with smaller Froude numbers. Using the same size stones as in the experiments described in this report, but with a lower density is not possible, the buoyancy of the stones would be too large. A smaller stone size has the disadvantage of losing the possibility to mount pressure transducers in the stones.
- Experiments without a hinge allow investigation of the flow structures that make stones move in the upstream direction. However, this is probably the only advantage of the absence of a hinge, while the experiments will become much more laborious. Besides, only in a small area upstream of the reattachment region stones move in the direction of the step.
- It would be very convenient to have a larger number of stone movements under low-mobility conditions. So experiments with a long duration, up to several days, are recommended.
- A higher sample frequency of the PIV recordings would enable determining temporal derivatives of the vector fields.
- At a later stage two cameras could be used to obtain 3-D flow fields (is possible with present software package).

LIST OF SYMBOLS

Greek symbols

- Δ = relative submerged density (= (ρ_s- ρ_w) / ρ_w))
- Π = protrusion
- Ψ = Shields parameter
- γ_l, γ_s = linear strain rate, shear strain rate
- δ = non-centrality parameter
- κ = von Kármán coefficient (= 0.4)
- λ (λ_{ci}) = swirling strength (sometimes λ = relaxation length)
- ν = kinematic viscosity
- ρ = density
- ρ_{12} = normalised cross-covariance function
- τ = bottom shear stress
- ω = vorticity

Roman symbols

- A = exposed area of stone
- A, B = areas around stone used to determine QSF respectively TWP
- B001 – B010 = experiment IDs
- C_d, C_l = drag and lift coefficient
- C_m = added mass coefficient
- D = discriminant of characteristic equation of 2-D local velocity gradient tensor
- D_1, D_2 = pressure sensors (drag) next respectively downstream of target stone
- E = entrainment rate
- F_A = indicator for magnitude of drag force on stone ($\propto <u>_A |<u>_A|$)
- F_d, F_l = drag and lift force
- Fr = Froude number
- H = step height
- K_v = velocity coefficient in stone stability
- $L_1 – L_4$ = pressure sensors (lift)
- Q = discharge; Weiss function; peak ratio factor
- P = chance; height of correlation peak
- Re = Reynolds number
- Re_H = Reynolds number based on step height
- Re_* = Particle Reynolds number
- S_f = Curry shape factor
- S_r = Strouhal number
- X_R = reattachment length
- U_0 = free stream velocity
- U_c = convection velocity
- U_{max} ($\approx U_0$) = mean maximum velocity above the trailing edge of the step
- V = volume of a stone
- a = distance from vortex core to wall
- b = width of flume
- c_f = friction coefficient
- d = diameter (e.g. of stone or vortex)
- d_n = nominal diameter
- d_{n50} = median nominal diameter
- e = exposure
- f = frequency
- g = gravitational acceleration

- h = water depth
- i = index to indicate recording time relative to the point in time of stone movement (in frames)
- k_0 = relative turbulent energy in the mixing layer
- l = step length (transported distance of stone)
- p = pressure
- q = transport of bed material
- r = turbulence intensity
- t = time, $t = 0$ is stone movement
- u, v, w = instantaneous velocity components in x, y, z directions
- $\bar{u}$, $\bar{v}$, $\bar{w}$ = mean velocity components in x, y, z directions
- u', v', w' = instantaneous fluctuating velocity components in x, y, z directions
- u_* = shear velocity
- x, y, z = rectangular Cartesian co-ordinates

Subscripts

- 0 = free stream
- 1 = upstream of BFS
- 2, 3 = downstream of BFS
- rms = root-mean-square value
- b = bed
- c = critical
- s = stone
- u = uniform
- w = water

Abbreviations

- 2-D, 3-D = two-dimensional, three-dimensional
- BFS = backward-facing step
- CS = coherent structures
- DNS = direct numerical simulations
- EMF = electromagnetic flow meter
- HVS = hairpin vortex signature
- LDA = laser Doppler anemometry
- LES = large eddy simulation
- PIV = particle image velocimetry
- QSF = quasi-steady forces
- TWP = turbulent wall pressures

Miscellaneous

- $\langle X \rangle_h$ = spatial averaging of quantity X over depth
- $\langle X \rangle_A$ = spatial averaging of quantity X over area A

REFERENCES

ADRIAN, R.J., K.T. CHRISTENSEN, Z.-C. LIU, 2000a. *Analysis and interpretation of instantaneous turbulent velocity fields*. Experiments in Fluids 29, pp275-290. Springer-Verlag.

ADRIAN, R.J., C.D. MEINHART, C.D. TOMKINS, 2000b. *Vortex organisation in the outer region of the turbulent boundary layer*. Journal of Fluid Mechanics 422, pp1-54. Cambridge University Press.

ADRIAN, R.J., S. BALACHANDAR, Z.C. LIU, 2001. *Spanwise Growth of Vortex Structure in Wall Turbulence*. TAM (Theoretical and Applied Mechanics) Report 980. University of Illinois. Also published in Korean Society of Mechanical Engineers International Journal 15, pp 1741-1749.

BATTJES, J.A., 1996. *Lecture notes Vloeistofmechanica.* Delft University of Technology. In Dutch.

BENDAT, J.S., A.G. PIERSOL, 1971. *RANDOM DATA: Analysis and Measurement Procedures.* Wiley-interscience.

BOSMA, C., 2001. *Porositeit in breuksteenconstructies, Onderzoek naar en bepaling van factoren die de hoeveelheid geplaatst materiaal bepalen*. M.Sc.-thesis, Delft University of Technology. In Dutch.

CHIEN, N., Z. WANG, 1999. *Mechanics of Sediment Transport*. Reston, Virginia: ASCE press.

CHRISTENSEN, K.T., R. J. ADRIAN, 2002. *The velocity and acceleration signatures of small-scale vortices in turbulent channel flow.* Journal of Turbulence 3, 023.

CUR REPORT 169, 1995. *Manual on the use of Rock in Hydraulic Engineering*. Gouda: CUR.

DELCAYRE, F., M. LESIEUR, 1997. *Topological feature in the reattachment region of a backward-facing step*. First AFOSR international conference on DNS and LES. Ruston.

DHL, 1985. *Hydraulic design criteria for rockfill closure of tidal gaps, vertical closure,* report M1741.

ETHERIDGE, D.W. & P.H. KEMP, 1978. *Measurements of Turbulent Flow Downstream of a Rearward-Facing Step.* Journal of Fluid Mechanics 86, pp 545-566. Cambridge University Press.

EINSTEIN, H.A., E.A. EL-SAMNI, 1949. *Hydrodynamic forces on a rough wall.* Reviews of Modern Physics 21, pp520-524.

FENTON, J.D., J.E. ABBOT, 1977. *Initial movement of grains in a stream bed: the effect of relative protrusion*. Proceedings of the Royal Society of London, Series A, vol. 352, pp523-537.

FRANKEN, A., E. ARIËNS, H. KLATTER, 1995. *Handleiding voor het Ontwerpen van granulaire Bodemverdedigingen achter tweedimensionale Uitstromingsconstructies.* Ministerie van Verkeer en Waterstaat, Directoraat-Generaal Rijkswaterstaat, Bouwdienst Rijkswaterstaat, Hoofdafdeling Waterbouw. In Dutch.

GEORGE, W. K., P. D. BREUTER, R.E.A. ARNDT, 1984. *Pressure spectra in turbulent free shear flows.* Journal of Fluid Mechanics 148, pp 148-191. Cambridge University Press.

GUNST, M.D. DE, 1999. *Steenstabiliteit in een turbulente stroming achter een afstap*. M.Sc.-thesis Delft University of Technology. In Dutch.

HOFFMANS, G.J.C.M., 1993. *A hydraulic and morphological Criterion for upstream Slopes in local-scour Holes.* Ministry of Transport, Public Works and Water Management. Road and Hydraulic Engineering Division. Delft.

HOFLAND, B, R. BOOIJ, 2004. *Measuring the flow structures that initiate stone movement*. Proceedings of the second international conference on fluvial hydraulics, 23-25 June. River flow 2004, volume 1, pp 821-830.

HOFLAND, B., J.A. BATTJES, R. BOOIJ. Subm.a. *Measurement of fluctuating pressures on coarse bed material.* Accepted by Journal of Hydraulic Engineering.

HOFLAND, B. Subm.b. *The probability density function for instantaneous drag forces and shear stresses on a bed.* Submitted to Journal of Hydraulic Engineering.

HOFLAND, B., J.A. BATTJES, R. BOOIJ, H.L. FONTIJN. Subm.c. *Turbulence wall pressures and forces on bed material, theory and measurements.* Submitted to Journal of Fluids and Structures.

JEONG, J., F. HUSSAIN, 1999. *On the identification of a vortex.* Journal of Fluid Mechanics 285, pp69-94.

JONGELING, T.H.G., A. BLOM, H.R.A. JAGERS, C. STOLKER, H.J. VERHEIJ, 2003. *Design method granular protections.* Tech. Rept. Q2933/Q3018. WL|Delft Hydraulics.In Dutch.

KOSTAS, J., J. SORIA, M.S. CHONG, 2002. *Particle image velocimetry measurements of a backward-facing step flow*. Experiments in Fluids 33, pp838-853. Springer-Verlag.

LA VISION, 2002. *FlowMaster Manual for DaVis 6.2*.

LEE, I., H.J. SUNG, 2002. *Multiple-arrayed pressure measurement for investigation of the unsteady flow structure of a reattaching shear layer*. Journal of Fluid Mechanics, vol.463000, pp377-402. Cambridge University Press.

NAKAGAWA, H., I. NEZU, 1987. *Experimental investigation on turbulent structure of backward-facing step flow in an open channel*. Journal of Hydraulic Research, vol. 25, no. 1.

NELSON, J.M., R.L. SHREVE, S.R. MCLEAN, T.G. DRAKE, 1995. *Role of near-bed turbulence structure in bed load transport and bed form mechanics*. Water Resources Research, vol. 31, no 8, pp2071-2086.

PAINTAL, 1971. *Concept of critical shear stress in loose boundary open channels.* Journal of Hydraulic Research, 9-1, pp91-113.

RAFFEL, M., C. WILLERT, J. KOMPENHANS, 1998. *Particle Image Velocimetry: A Practical Guide*. 3rd Printing. Berlin: Springer-Verlag.

SCARANO, F., C. BENOCCI, M.L. RIETHMULLER, 1999. *Pattern recognition analysis of the turbulent flow past a backward-facing step.* Physics of Fluids, vol. 11, no. 12.

SCARANO, F., M.L. RIETHMULLER, 2000. *Temporal analysis of coherent structures in a turbulent BFS flow with PIV.* Applications of Laser Techniques to Fluid Mechanics. 10th International symposium, 10-13 July 2000. Lisbon.

SCHIERECK, G.J., 2001. *Introduction to Bed, bank and shore protection*. Delft: Delft University Press.

SHIELDS, A., 1936. *Anwendung der Aehnlichkeitsmechanik und der Turbulenzforschung auf die Geschiebebewegung*. Mitteilungen der Preußischen Versuchsanstalt für Wasserbau und Schiffbau, Heft 26. Berlin.

SIMPSON, R.L., 1989. *Turbulent boundary-layer separation.* Annual Review of Fluid Mechanics, 21, pp205-234.

TROMP, M., 2004. *The influence that fluid accelerations have on the threshold of motion.* M.Sc.-thesis. Delft University of technology.

XINGKUI, W., H.L. FONTIJN, 1993. *Experimental study of the hydronamic forces on a bed element in an open channel with a backward-facing step*. Journal of Fluids and Structures 7, pp299-318.

APPENDICES

Appendix A Kinematic viscosity

Since the kinematic viscosity of water is temperature-depended, a new value was calculated for each experiment. Using the following formulae:

if $T < 20$ °C:

$$\nu = \frac{10^{\left(\frac{1301}{998.333+8.1855\cdot(T-20)+0.00585\cdot(T-20)^2}\right)-3.30233}}{10000} \tag{A.1}$$

if $T > 20$ °C:

$$\nu = 10^{\left(\frac{1.3272\cdot(20-T)-0.001053\cdot(T-20)^2}{T+105}\right)} \cdot \frac{1.002}{1000000} \tag{A.2}$$

in which:

T = temperature in degrees Centigrade (°C)
v = kinematic viscosity (m^2/s)

A density of the water of $\rho_w = 1000$ kg/m3 is assumed implicitly in these formulae.

Appendix B Stones

Porosity

The porosity of the stones used in the experiments was estimated at 40 percent. This is a common value for a first approximation for angular stones. Both literature as well as a simple experiment have verified this value. In the MSc-thesis of Bosma (2001), which deals with porosity of angular stones, a porosity of circa 40 percent was found for similar stones (shape, size, grading).

The experiment that was carried out to verify the porosity is a simple measurement of the amount of water that the voids between the stones can contain. This amount divided by total volume (stones and voids) is the porosity ε. To enable this, stones were placed in an elongated container made of glass (see Figure B.1). On one of the long sides of the container were two horizontal lines. One a little above the bottom and the other near the top of the container. The container was filled with water and the amount of water that was added between the two lines was registered. After the water and the stones were taken out of the container, it was filled with water again and once more the amount of water between the two lines was determined.

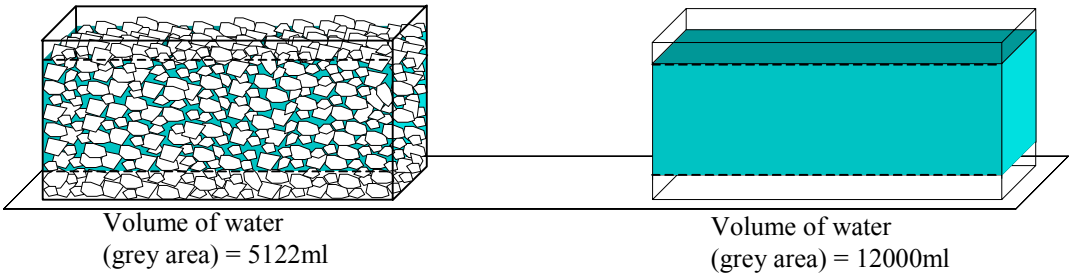

FIGURE B.1 *Determining porosity of stones used.*

The porosity turned out to be about 43 percent (5122 ml /12000 ml * 100% = 42.7%). This is a bit more then the above-mentioned 40 percent, but it is the same order of magnitude. In order to avoid the influence of the bottom, where the porosity is higher, the area near the bottom was not included in the measurement; only the area between the lines was taken into account. However, the influence of the sides of the container could not easily be eliminated in the way it had been done with the bottom, causing an error in the form of an increased value of the porosity. This, along with the rough way the experiment was carried out, could explain the difference between the percentages. Therefore a value of 40 percent was used.

Dimensions
The so-called Curry shape factor S_f (Chien & Wang, 1999) was determined by measuring the three dimensions of the stones, yielding:

$$S_f = \frac{a}{\sqrt{b \cdot c}} = \frac{15.4mm}{\sqrt{24.5mm \cdot 31.1mm}} = 0.56 \qquad \text{(B.1)}$$

in which:

a = shortest side of stone
b = intermediate side of stone
c = longest side of stone

We used a sample of 240 stones to determine the three dimensions. The dimensions were measured as depicted in Figure B.2. So a, b and c are in fact the dimensions of the smallest possible box that can contain the stone, see CUR report 169 (1995).

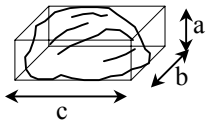

FIGURE B.2 *The sides of a stone.*

Sieve curve
The mass distribution of the stones used to construct the granular bed is depicted in Figure B.3. Also this figure is based on 240 stones.

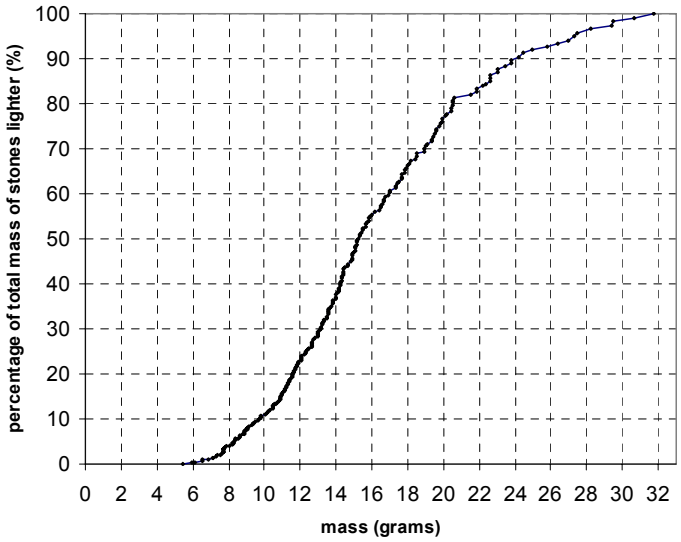

FIGURE B.3 *Cumulative mass curve.*

The average mass M of the stones was 14.6 grams and the average density was circa 2700 kg/ m^3. With this knowledge and the definition of the nominal diameter d_n (= $(M/\rho)^{1/3}$, where M denotes the mass of a stone and ρ the density), we can convert the cumulative mass curve to a distribution curve of the nominal diameters. The result is depicted in Figure B.4.

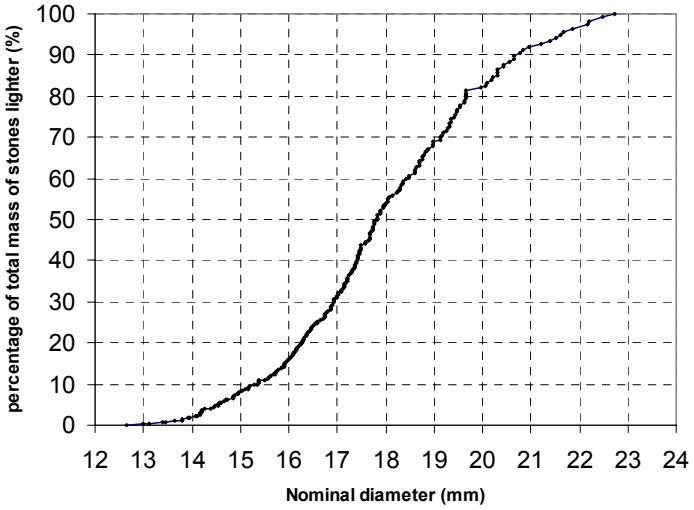

FIGURE B.4 *Distribution of nominal diameter.*

From Figure B.4 the d_{n50} could be determined. This is the diameter for which the following is true: the mass of all stones with a diameter smaller than d_{n50} is just as much as the mass of all stones with a diameter larger than d_{n50}. Furthermore, d_{n85} and d_{n15} (similar definitions) could be determined. We found the following values, see also Table 3.1: d_{n50}. = 17.81 mm; d_{n85} = 20.25 mm and d_{n15} = 15.92 mm.

Appendix C Discharge return pipework

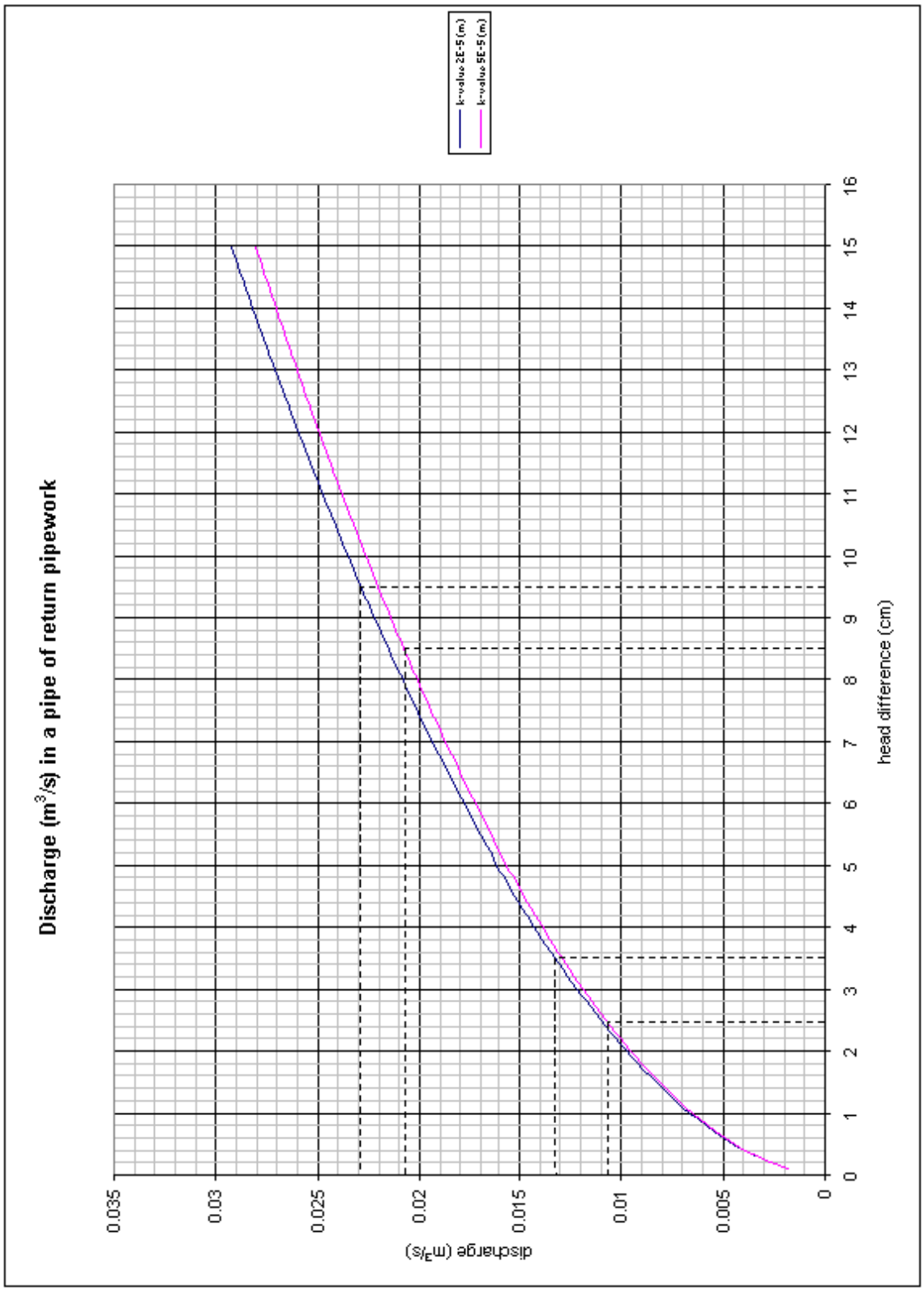

FIGURE C.1 *Discharge as function of the pressure head difference for the pipes of the return pipe work.*

In order to know the discharge in the flume, each pipe of the return pipework was equipped with a manometer from which the drop of pressure over a length of 11.01 m of each pipe could be determined. These readings were translated into discharges by means of a White-Colebrook type of formula. For this, the roughness of the interior of the PVC pipes must be known. The *k*-value, i.e. the equivalent sand roughness, for PVC was estimated to be somewhere between $2 \cdot 10^{-5}$ m and $5 \cdot 10^{-5}$ m (see e.g. Battjes, 1996).

$$u_* = \sqrt{gRi} \tag{C.1}$$

$$\mathrm{Re}_* = \frac{u_* \cdot k}{\nu} \tag{C.2}$$

$$\frac{1}{\sqrt{f}} = -2 \log\left[0.27 \frac{k}{D}\left(1 + \frac{3.3}{\mathrm{Re}_*}\right)\right] \tag{C.3}$$

in which:

u_* = shear velocity (m/s)
g = gravitational acceleration of gravity (m/s^2)
R = hydraulic radius (= 0.25D) (m)
i = friction slope [-]
Re_* = particle Reynolds-number [-]
k = equivalent sand roughness (m)
υ = kinematic viscosity (m^2/s)
f = Darcy-Weisbach friction parameter [-]
D = inner diameter of pipe (m)

Since the pressure head difference (Δp) over 11.01 m of each pipe is known, the friction slope i is know as well: $i = \Delta p$ / 11.01 m. Together with the known inner diameter of the pipe, the Darcy-Weisbach friction parameter can be calculated. With this parameter the discharge through a pipe can be calculated:

$$U = \frac{u_*}{\sqrt{f/8}} \tag{C.4}$$

$$Q = U \tfrac{1}{4} \pi D^2 \tag{C.5}$$

in which:

U = velocity averaged over pipe cross-section (m/s)
Q = discharge through pipe (m^3/s)

Note that it was assumed that the pipes were completely filled with water (R = 0.25D), which was indeed the case during the experiments.

If this computation is repeated for a range of pressure head differences, a curve as depicted in Figure C1 is the result. The graph actually shows two curves (solid lines), each for a different *k*-value. The blue line is for a *k*-value of 0.02 mm and the pink one for a *k*-value of 0.05 mm. The uncertainty of this value together with a reading accuracy of about 0.5 cm of the drop of pressure readings on the water-level gauge of the manometers, result in an inaccuracy of measurement of a little more than 2 l/s per pipe. This is indicated by the dashed lines for two representative values of the pressure head difference, viz. 9 cm and 3 cm. A pressure head difference of around 9 cm often occurred when the valve in a pipe was fully opened. As a

result a head difference of 3 cm often occurred in a second pipe (with valve only partly opened) to be able to transport all the water from the outlet structure back to the basin.

Now for each pipe the discharge is known, and since only stationary flow situations were examined, simply adding up of these discharges results in the discharge through the flume. Most of the time only two pipes were used, resulting in an accuracy of measurement of 4 l/s (± 2 l/s).

The graph was used to make a first estimation of the discharge through the flume during the experiments. For the kinematic viscosity a value of $1.0 \cdot 10^{-6}$ m^2/s was used when constructing the graph. When the data was analysed, the discharge through the flume was calculated by the formulae described above, but for each experiment with a more accurate, temperature-corrected value of the kinematic viscosity. The variation of the kinematic viscosity of water with with temperature, can be found in appendix A.

Check of calculation

To check the computation as described above, the discharge through the flume for an established flow was also estimated by another approach (PIV measurements were not yet available). This check was done by means of electromagnetic flow meter (EMF) measurements.

Velocities, at different heights above the bed, were measured at the hand of the EMF for three different distances from the side of the flume. In this way three vertical velocity-profiles were obtained. One of the profiles was located in the centre line of the flume, the other two were located between the centre line and one side of the flume, both at the same side of the centre line. With the EMF it was not possible to determine flow velocities near the water surface. In the region near the surface the EMF produces values that are too low: the closer to the surface, the lower the values. For this reason for each velocity profile the velocity from the point with the highest EMF value up to the water surface was taken constant, namely the highest EMF value. If it is assumed that the average flow is symmetrical with respect to the centre line (checked for one point in the flow) and that the velocities at the sides of the flume and on the bottom are zero then a 3-D velocity distribution as can be seen in Figure C.2 is the result.

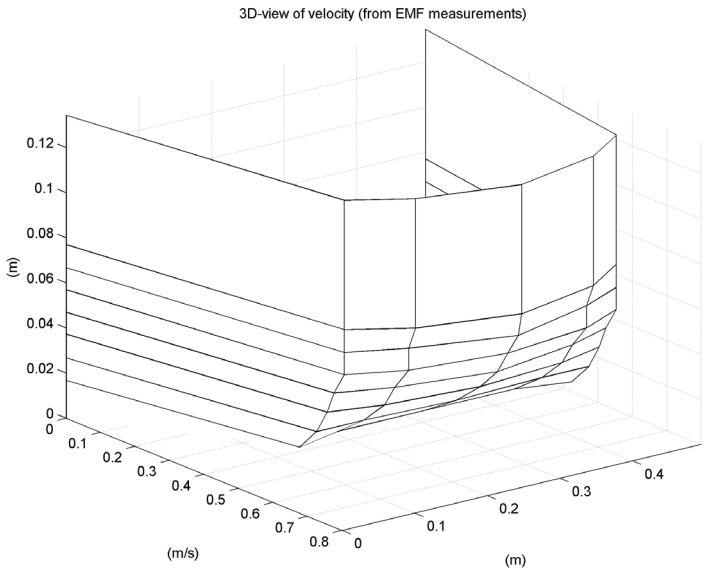

FIGURE C.2 *Longitudinal velocity profile determined by EMF measurements.*

For each intersection of lines of the 3-D plot of velocities a velocity is known (known either by measuring or mirroring of a measured value). For each arbitrary position in the flow, the velocity was chosen to be equal to the nearest known velocity. For those cases in which the arbitrary point is closer to a side of the flume or closer to the bottom than to a point for which the velocity is known the velocity was set to zero. So for a rectangle area encompassing each intersection the velocity was taken the same as the velocity in the intersection. In this way the discharge could be calculated by using a simple Matlab script. The result of this approach for a flow with a discharge of 38.6 l/s (according to the manometers) was 38.1 l/s. These values coincide better than was expected and even though it was already concluded that the accuracy of measurement of the manometers is something like 4 l/s (total discharge through flume), now at least it seems that this margin of 4 l/s is located around the appropriate (mean) value of the discharge.

Appendix D Specifications of equipment

Camera
Manufacturer: *Kodak*
Model: *ES 1.0*
Resolution: 1016 x 1018 pixels (In DaVis reduced to 1007 x 1007 pixels)
Maximum sample rate: 15 Hz for double framed images, 30 Hz for single images

Pressure transducers
Manufacturer: *Honeywell*
Model: *24PCEFA(XX)*

Amplifiers
Manufacturer: *HBM*
Model: *KWS 3020*
Type: direct current amplifier

Analogue electronic filters
Manufacturer: *Kemo*
Model: *VBF 8* dual variable filter
Range: 0.01Hz – 100kHz

Laser
Type: class IV, Nd:YAG (532 nm)
Manufacturer: *New Wave Research (Solo PIV)*
Model: *Solo TTT 15 Hz*
Purveyor: *LaVision GmbH* (name of set: Flowmaster 2)

Seeding
Manufacturer: *Potters Industries inc.*
Model: *Sphericel 110P8*
Purveyor: *LaVision GmbH*
Shape: spherical
Color: white
Composition: proprietary glass
Density: 1.1 g/cc
Particle size mean diameter: 11 microns

Appendix E Plates with cement-bound stones

In case the granular bed is placed directly on the bottom of the flume, an abrupt change in porosity will occur. Since the bottom of the flume is made of concrete (flat) and the shapes of the stones are irregular, there will be little contact between the stones and the bottom, resulting in a nearly hundred percent porosity near the bottom. The percentage of voids in the bed-material however, is approximately 40%. To avoid this abrupt change in porosity, plates made of reinforced cement, in which stones have been placed in a regular pattern, have been placed on the bottom of the flume.

Horizontal positions of the stones
The stones have been positioned in such a way that the ratio of the remaining area (i.e. the area of the cement between the stones) and the total area of the bottom, equals the porosity of the granular bed. To determine the distance t between the stones in the cement, in order to obtain the desired porosity, the following conditions and assumptions have been taken into account:

1. Porosity bed material (ε) = 0.40
2. Regular pattern of stones throughout the flume
3. Ratio of area in between stones and total area of the bottom = porosity bed material
4. Curry Shapefactor is 0.56 (see appendix B):
5. Stones are assumed to be box-shaped and all stones are assumed to be equal
6. Short sides of stones are directed upward, hence stones lie on intermediate and longest side

From condition 3 it follows that:

$$A_{total} - A_{stones} = A_{cement} \Rightarrow \frac{A_{total}}{A_{total}} - \frac{A_{stones}}{A_{total}} = \frac{A_{cement}}{A_{total}} \Rightarrow 1 - \frac{A_{stones}}{A_{total}} = \varepsilon = 0.4 \qquad \text{(E.1)}$$

In which A_{total}, A_{stones} and A_{cement} are the total area, the area covered by stones and the area between the stones respectively.

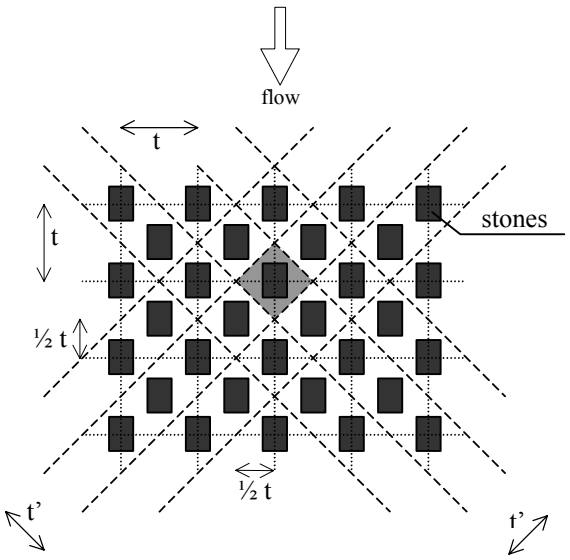

FIGURE E.1 *Top view of grid of cement bound stones*

By dividing the total area into segments as indicated in Figure E.1 (diagonal lines), there will be no overlapping of light grey areas (areas "belonging" to one stone). This, together with assumption 5, which in fact states that there is one box-shaped stone, which is representative for all stones, allows that the formula can be applied to one (the representative) stone. So, the distance *t'* can be used in this formula to calculate A_{total} ($A_{total} = t' * t'$). This results in:

$$1 - \frac{A_{stone}}{t' \cdot t'} = 0.4 \tag{E.2}$$

If A_{stone} is known, *t'* can be determined. Finally the distance between the stones *t* is known from the geometry:

$$t = \sqrt{2} \cdot t' \tag{E.3}$$

So, the area covered by the representative stone, A_{stone} , is the only remaining unknown parameter. This area depends on the method that is used to translate the values for a_{avg}, b_{avg}, c_{avg} (average values of the three sides of the stones), M_{avg} (average mass of stones) and ρ_{avg} (average density of stones), which are average values based on a sample of 240 stones (see condition 4 and appendix B), into the three dimensions of the representative box-shaped stone. From 6 it is deduced that of these three dimensions only the intermediate and the longest determine the area covered by the stone.

Three methods are used to translate the values for a_{avg}, b_{avg}, c_{avg}, M_{avg} and ρ_{avg} into the three dimensions of the representative box-shaped stone. The first approach is based on the assumption that the representative stone has a volume that is the same as the volume of the enclosing cuboid ($a_{avg} \cdot b_{avg} \cdot c_{avg}$) (see appendix B). In fact now the enclosing cuboid is the representative stone and the area covered by this stone is $b_{avg} \cdot c_{avg}$. This approach can be seen as an upper-limit of A_{stone}, for a stone can never be larger than its enclosing cuboid. Also this approach overestimates the area that is covered by a stone, because most of the times a stone will cover an area smaller than $b \cdot c$. With b_{avg} = 24.5 mm and c_{avg} = 31.1 mm this approach yields t = 50.4 mm.

The second method is based on the average mass and average density of the sample of 240 stones. With these values $D_{n,avg}$ (= $(M_{avg} / \rho_{avg})^{1/3}$) can be calculated, which yields $D_{n,avg}$ = 17.53 mm. The representative stone is now a cube and the area beneath it (A_{stone}) is $D^2_{n,avg}$. (Note that $D_{n,avg}$ is used and not $D_{n,50}$, because it is the size of the stones that is important. Since there are more stones that are smaller than $D_{n,50}$ than there are that are larger (by definition), $D_{n,50}$ would not be a proper value to use in this case.) The result of this approach is t = 32.0 mm. Because a cube is the smallest possible rectangular shape to contain a certain volume (i.e. the rectangular shape with the smallest surface area) and because it is assumed that the stones lie with their short sides directed upward, this method can be considered as a lower limit of A_{stone}. This will be explained some more: In the case of a lower limit, the volume of a stone must fit in a box with the smallest possible base. So the product $b \cdot c$ must be as small as possible. This is the case when a is as large as possible ($b \cdot c = V / a$), but a can never be larger than b, because a has to be the shortest axis. If a would be larger than b, then the stone would have a different orientation. Hence the maximum value for a is b. The product $b \cdot c$ is as small as possible, when b is as small as possible and when c is as small as possible. The smallest possible value for b is a and for c is b, because they are by definition the lengths of the intermediate and the longest axis respectively. All three sides are now equal, so the representative stone is indeed a cube. Since all three sides are the same, the shape factor

is one. The average shape factor however is 0.57 (see appendix B). Therefore the third method has to take the shape factor into account.

For the third way to determine A_{stone} the average volume of the stones as well as the shape factor is kept in mind. The average volume ($V_{avg} = M_{avg} / \rho_{avg} = D^3_{n,avg}$) is smaller than the volume of the enclosing cuboid ($a_{avg} \cdot b_{avg} \cdot c_{avg}$). The values for a_{avg}, b_{avg} and c_{avg} have to be smaller, so that $a_{avg} \cdot b_{avg} \cdot c_{avg} = V_{avg}$, but the shape factor has to remain the same. In order to achieve this, the three values for a_{avg}, b_{avg} and c_{avg} have to be divided by the cube root of V_{avg} / ($a_{avg} \cdot b_{avg} \cdot c_{avg}$). In formulae:

$$\begin{aligned} V_{avg} &= M_{avg} / \rho_{avg} = 5390 mm^3 \\ a_{avg} \cdot b_{avg} \cdot c_{avg} &= 11716 mm^3 \\ \alpha &= \frac{V_{avg}}{a_{avg} \cdot b_{avg} \cdot c_{avg}} = 2.17 \end{aligned} \qquad \text{(E.4)}$$

$$\begin{aligned} a' &= a_{avg} / \sqrt[3]{\alpha} = 11.88 mm \\ b' &= b_{avg} / \sqrt[3]{\alpha} = 18.89 mm \\ c' &= c_{avg} / \sqrt[3]{\alpha} = 24.02 mm \end{aligned} \qquad \text{(E.5)}$$

$$\begin{aligned} S_f &= \frac{a'}{\sqrt{b' \cdot c'}} \approx 0.57 \\ V &= a' \cdot b' \cdot c' = 5390 mm^3 \end{aligned} \qquad \text{(E.6)}$$

in which *a'*, *b'* and *c'* are the three sides of the representative box-shaped stone.

The shape factor now has the same value as the shape factor with the average values and the volume is the same as the average volume, so this is truly a representative stone. Now that A_{stone} (= *b'* * *c'*) is known, the distance *t* can be calculated, resulting in *t* = 38.9 mm, which is indeed between the upper-limit and lower-limit values. So this value has been used when the cement plates were produced.

Note that since a, *b* and *c* are correlated (by definition) the average of (a · *b* · *c*) is not the same as $a_{avg} \cdot b_{avg} \cdot c_{avg}$. Something similar holds for D_n. For each of the 240 stones of the sample a value for D_n ($=(M / \rho)^{1/3}$) can be computed. The average of these D_n-values is not the same as the value that is obtained when using the average values for mass and density of the stones to calculate $D_{n,avg}$ ($=(M_{avg} / \rho_{avg})^{1/3}$). However, the differences are small and can be neglected when taking into account the accuracy of manually positioning the stones in the cement, which is not that high.

Vertical positions of the stones

Now that the horizontal positions of the stones are known, the only remaining difficulty is their vertical positions. In other words: how deep do the stones have to be pushed into the cement? In the above it is assumed that the stones are box-shaped and that they lie on their intermediate and their longest sides. In reality the stones all differ in shape and size and therefore the horizontal plane, defined by the intermediate and the longest axis of a stone, can for instance be a quarter or half way up the height *a* of the stone. According to the way the

distance *t* has been calculated, every stone should be pushed just as far into the cement until the horizontal plane formed by the intermediate and the longest axes, is on the same level as the surface of the cement. But in that case a little stone (small shortest axis *a*) can protrude more than a large stone (large shortest axis *a*), which would not often be the case in reality. It is also difficult to position a stone as far into the cement as described, because when the neighbouring stone is placed the cement will rise a little, causing the first stone to end up deeper in the cement. A total length of 15 meters of cement plates had to be produced manually. The plates vary in length from 50 cm up to 120 cm, but most are approximately 1 m long. So over a length of circa 1 m and a width of around 50 cm, stones had to be placed before the cement hardened. Moreover the stones had to be deep enough into the cement in order to be held in place. For these reasons it was decided to place the stones half the height *a* into the cement and to neglect the effect of placing the adjacent stones.

Length of plates

As mentioned before, the plates with the cement-bound stones vary in length from 50 cm to 120 cm. The reason for this is that the section in which the PIV-measurements take place cannot be moved easily. It is nearly impossible to move the measurement equipment if measurements of pressures around the target stone are desired as well, as a hole in the bottom of the flume is necessary to connect the wires to the built-in pressure sensors. To be able to perform measurements at different distances downstream of the backward-facing step, the step had to be moved to the desired distance upstream of the target stone. The varying lengths of the plates made this possible.

This BFS study is part of a Ph.D. study, in which the fully developed, uniform turbulent flow above a granular bed is one of the subjects of investigation. The plates were also used to create this configuration, therefore their total length had to be long enough for the water motion to become fully developed. Because this fully developed, homogeneous flow can be considered as the flow that occurs far downstream (100 or more times the depth of the water) of the BFS, this configuration is also of interest for this research.

After a (abrupt) change in geometry it takes a length of about 45 times the water depth, before the water motion is fully developed again. In other words: after a length of 45 times the water depth downstream of the last change in geometry, the change is no longer perceptible. However when turbulent characteristics of the flow need to be examined, it is often desired that the flow is homogeneous and then a length of 50 to 100 times the water depth is required. During uniform flow conditions, over a length of 10.5 m, directly upstream of the target stone, the bottom of the flume was covered by the plates. The maximum water depth during uniform flow conditions at which measurements were carried out was about 15 cm, resulting in a length of 10.5 m / 0.15 m = 70 times the water depth. Over a length of circa 5 m downstream of the measuring section, the bottom was also covered with plates. Further downstream there just was the flat concrete bottom of the flume itself. It was assumed that 5 m was long enough for the transition granular bed-concrete bottom to be of no influence on the measurements.

Appendix F Determination of bed level

It seemed reasonable to consider the level $y = 0$ that is generally used as the reference level for the log-law for the horizontal velocity in uniform flows ($u(y) = (u_* / \kappa) \ln(y / y_0)$, where κ is the von Kárman constant and $u = 0$ at the height y_0) as the bottom level. To this end we determined the average $y = 0$ level of three different uniform flow conditions, by fitting log-profiles to the measured velocities as is visualised in Figure F.1. We used the least-square method to determine the profiles, but only for the lower part (up to 50 mm above the new to establish zero level) of the measured velocities. In this way the resulting bed shear stress deviated no more than 10% of the bed shear stress as determined from the slope in the water surface.

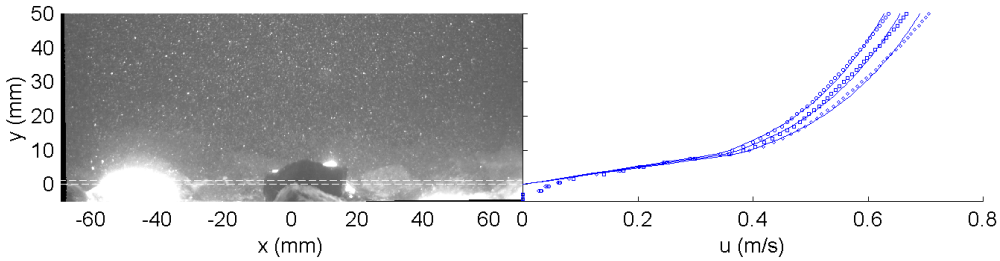

FIGURE F.1 *Determination of the level y = 0 by fitting longitudinal velocity profiles to three series of u-velocity measurements, each series representing other uniform flow conditions.*

The level $y = 0$ (lower horizontal dashed line) turned out to be 2.5 mm below lift sensor nr. 1 This level was considered "the bottom level". The level at which the mean u-velocity was zero, the level y_0, was located only a little (1 mm) above the reference level and is indicated by the upper horizontal dashed line.

Appendix G Settings for vector calculation (experiment B006)

In this appendix the settings of the parameters involved in the vector calculation procedure are listed. These settings are meant for those who want to use the same experimental equipment. The list given here is only valid for experiment B006, however during the other experiments the settings were only slightly different.

TABLE G.1 *Settings of PIV system for vector calculation*

data range:	mask
image preprocessing:	high pass(4)
Correlation mode:	cross-corr. 1 camera
interrogation window:	32 x 32 pixels (twice) followed by 16 x 16
Corr. Peak search confined:	Vx: 4 +- 10 Vy 0+-10
Sliding background:	4 pixels
Image correction:	yes

Interrogation window	
Initial shift:	dx =0 dy =0
Correlation Function	
initial passes:	I1 x I2 (FFT) no zero padding
final passes:	I1 x I2 (FFT) no zero padding
Adaptive Multipass	
Relative vector range restriction:	cell size/3
Absolute vector range restriction:	20 pixels
overlap for initial passes:	50%
Postprocessing	
delete vector if:	Q<1.2
fill up & fill up all:	both on by default
Median filter:	strongly remove and iteratively replace (default)
Smoothing:	once (3 x 3)
Median filter	
remove if:	> 1.5 rms of neigbours
remove if:	< 3 neighbours
insert if:	<1.5 rms of neighbours
Remove groups with less than:	off

Vector scaling:	m/s
Mask buffer:	yes, corrected for distortion

Vector postprocessing

Allowable vector range:	Vx: 7 +- 15 pix Vy: 0 +- 10 pix
Delete vector if Q<	<1.1
Median filter:	strongly remove and iteratively replace
Fill up empty spaces:	on
Fill up all:	off
Smoothing:	off
Apply allowable vector range again:	yes
Apply mask:	on
Median filter:	strongly remove and iteratively replace
remove if >	1.75 rms of neighbours
remove if <	3 neighbours
insert if <	1.75 rms of neighbours
Remove groups with less than:	5 vectors

Appendix H An approach to determine the Shields parameter (experiment B006)

The transport of bed material can be described by the following formula:

$$q_s = E \cdot l \tag{H.1}$$

in which:

q_s = the volume of transported bed material per meter width per second ($m^3/s/m$)
E = the so-called entrainment rate, this is the volume of bed material entrained from the bed per unit area per second (m/s)
l = the step length (m). This is the average distance a stone is transported once it has been dislodged from the bed.

From the data from De Gunst (1999), who counted the number of transported stones and their average displacement in the reattachment region, we found the ratio of average step length and stone diameter (d). It turned out that: $l \approx 6.2d$. The shape and size of the stones used in that experiment were similar to the stones used in this research.

As for a bed consisting of randomly placed spheres ca. 30% of the surface A is covered by spheres with the same high protrusion, we estimated that 30% of the surface ($0.3A$) of the bed in our experimental set-up had the same relatively high position as the target stone. So the number of stones per unit area that had the same high position as the target stone is $(0.3A)/(d^2A) = 0.3/d^2$. Together with the known average time between stone movements T, and the volume of a single stone V ($= d^3$), the entrainment rate E can be estimated: $E = (0.3V) / (Td^2) = 0.3d/T$. If the obtained estimations for E and l are substituted in Eq. (H.1) this yields:

$$q_s = E \cdot l = \frac{0.3 \cdot 0.6}{T} d^2 \tag{H.2}$$

With the known values for T and d from experiment B006, the volume of transported bed material per meter width per second in the reattachment region is known.

The transport formula of Paintal (1972) can be used to estimate the Shields parameter as follows:

$$q_s^* = \frac{q_s}{\sqrt{\Delta g d^3}} \tag{H.3}$$

$$\Psi_e = \sqrt[16]{\frac{q_s^*}{6.56 \cdot 10^{18}}} \tag{H.4}$$

As the Shields parameter is determined in a rather uncommon way, we used the subscript e to indicate that it is a parameter equivalent to the Shields parameter ψ.
Afterwards it needed to be checked if $\psi_e < 0.05$, if not then Eq. (H.4) is not valid and another expression must be used (not given here). This procedure yielded $\psi_e \approx 0.035$.

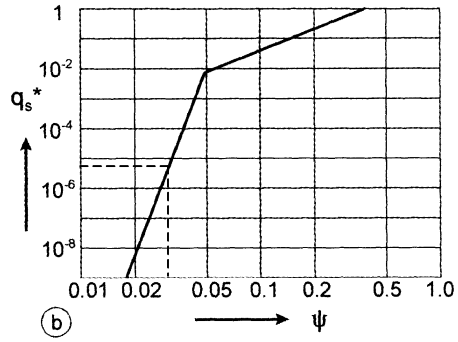

FIGURE H.1 *Transport of bed material according to Paintal.*

The approach described above is a very crude one. Moreover, Figure H.1 shows that a significant change in q_s^* hardly affects the resulting value of ψ $(=\psi_e)$, as the line that denotes the relation between the two parameters is very steep (provided that $q_s^* < 10^{-2}$ which was indeed the case, as we found $q_s^* \approx 3.3 \cdot 10^{-5}$, see dashed lines).

Appendix I Classification procedure (experiment B006)

Although it seems logical to chose semi-circles, with their centres located at the target stone, as areas for which values of F_A and $\sigma_v(B)$ needed to be calculated, we used rectangular areas (see right column of Figure I.1) for both areas A and B for practical reasons. The goal of altering the sizes of A and B was to find the sizes for which the scatter plot (see left column of Figure I.1) showed the largest segregation (both in horizontal as well as in vertical direction) of the black open circles, which represent the visually selected events, and the dashed lines which represent the average values. In that case the areas A and B can be considered the areas in which something occurs that causes the target stone to pivot; the areas that are "responsible" for entrainment.

Obviously, both area A and B had to be located in the vicinity of the target stone, but it was not so obvious how large these areas had to be. A few dimensions were tried that seemed logical as a first choice. All rectangles were located above the target stone, which is positioned at $x = 0$. Changing the size of area A could result (not necessarily) the horizontal position of each data point, changing the size of area B could change (again, not necessarily) the vertical position of each data point.

To compare the values of F_A and $\sigma_v(B)$ during entrainment to average values of F_A and $\sigma_v(B)$ we used the values of F_A and $\sigma_v(B)$ of both the 15 Hz / 20 s measurement and the 0.5 Hz / 10 min measurement. During both these measurements the target stone was fixed, so no stone movement could occur that would influence the flow. The time averaged values were determined as described in Chapter 2: first all the instantaneous values of F_A were determined and then the mean value was calculated from these values.

The averaging time had to be long with respect to the time scale of the turbulent motions. Therefore the 0.5 Hz / 10 min measurement seemed an appropriate choice. Unfortunately, the theoretical frequencies of some of the quasi-periodical mechanims associated with BFS flow had the same order of magnitude as the sample frequency of this measurement. If they were more or less in phase, it could be that the statistical quantities derived from this measurement were not a good representation of the average flow. Therefore the 15 Hz / 20 s measurement was included in the analysis as well, even though 20 s was a relatively short time with respect to the time scale of the turbulent motions.

The different sizes for A and B and the accompanying distributions of the two parameters are depicted in Figure I.1.

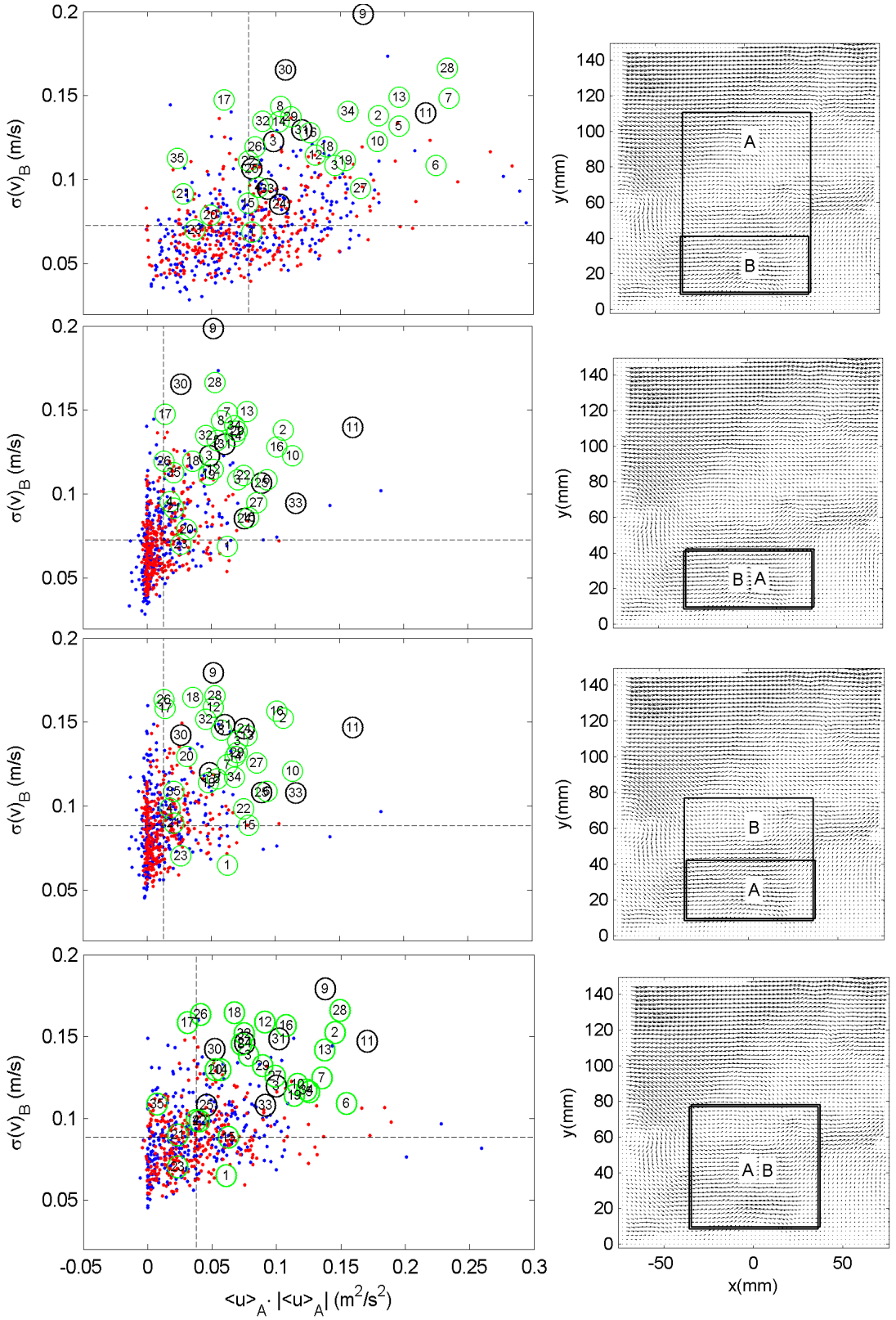

FIGURE I.1 *Right column: dimensions of areas A and B for which F_A respectively $\sigma_v(B)$ were calculated. Left column: accompanying scatter plots of F_A versus $\sigma_v(B)$. Black circles: visually selected events; green circles: rocking events; red dots: 15 Hz / 20 s measurement; blue dots: 0.5 Hz / 10 min measurement. Numbers, to indicate the number of the recorded events, mark the circles. The vertical and horizontal dashed lines represent the average value of F_A respectively $\sigma_v(B)$.*

The black circles are based on the last frame that was recorded before the target stone started to pivot around its axis (continuous upward movement), the green circles are based on the last frame before the frame at which displacement of the target stone was observable.

By the way the dots are concentrated in the second and third image from the top (in a vertical line), it looks like there is a bias of some kind. However, provided that a normally distributed variable has its mean in the vicinity of zero, the probability density function of the squared values of this variable shows a large peak in the vicinity of zero, see Figure 2.2 in Chapter 2. As both the red as well as the blue dots are distributed similary, it seems fair to conclude that neither measurements were dominated by either a flapping or vortex shedding mechanism. Some dots are located far from at least one of the dashed lines. Perhaps the target stone would have moved in these cases if it had not been fixed.

In all scatter plots the events seem to be located at the outer edges of the data cloud. A closer look at the upper most plot, that is based on a large area A, reveals that at least 3 out of the 8 visually selected events are located amidst the dots. Therefore this size for area A was rejected. Yet, this plot does show that a large area A results in a horizontally widespread area in which the data points are located, indicating a large variation in time of the average u-velocity in area A. The lowest of the scatter plots does not really discriminate the visually selected events from the rocking events and therefore the corresponding sizes for A and B were rejected as well. Both the second and the third plot from the top seem to do a fair job in discriminating the dots from the circles. Especially in the second plot from the top the visually selected events seem to be more separated from the rest, particularly in the vertical direction. The areas A and B as depicted in the second plot from the top in the second column were therefore chosen as the areas “responsible” for entrainment.

Appendix J Conditionally averaged swirling strength (experiment B006)

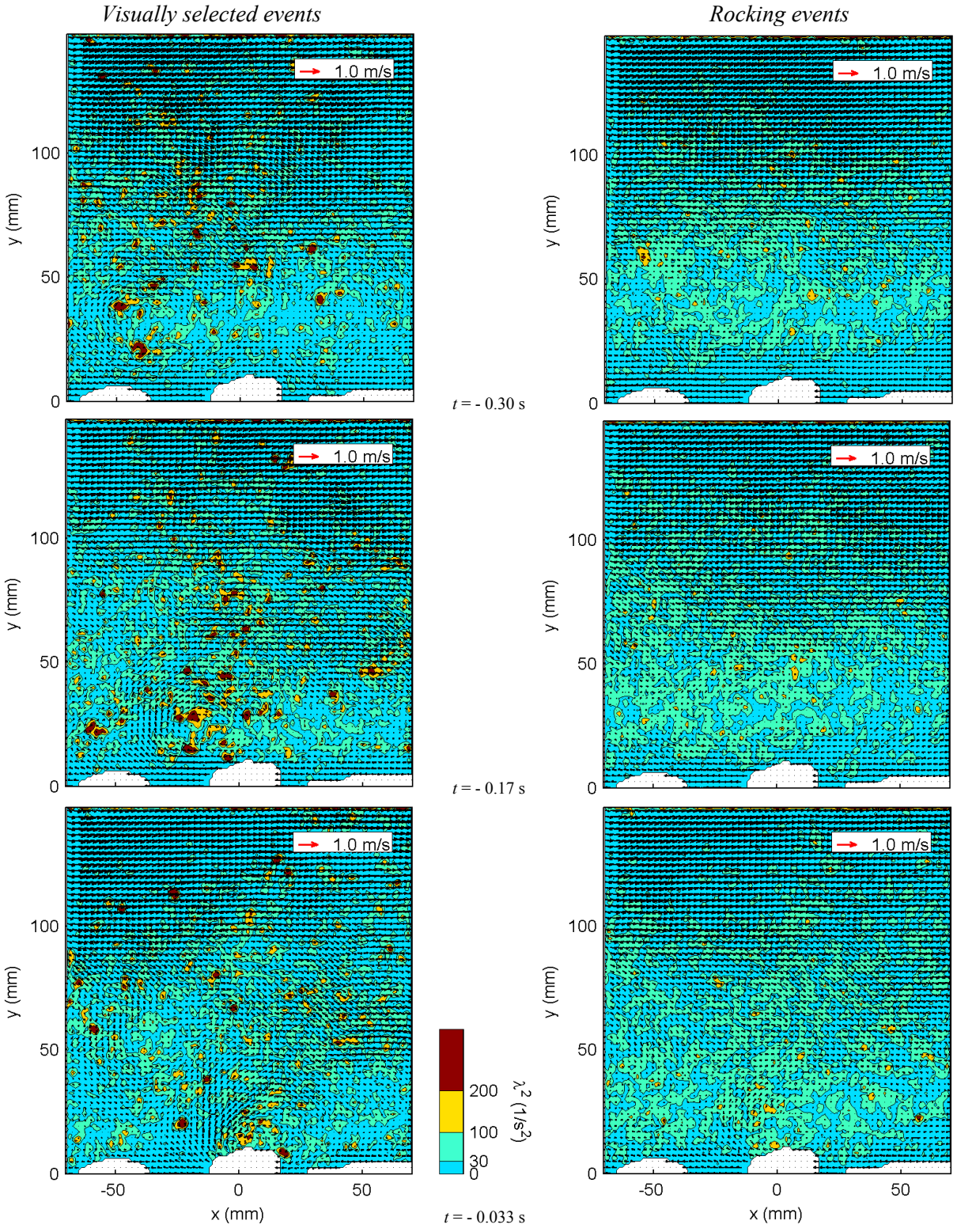

FIGURE J.2 *Sequence of conditionally averaged contour plots of the swirling strength λ^2 combined with vectors. Target stone located at x =0. For clarity only one out of four vectors is shown. Right column: rocking events. Left column: visually selected events.*

Appendix K Conditionally averaged flow of rocking events (experiment B006)

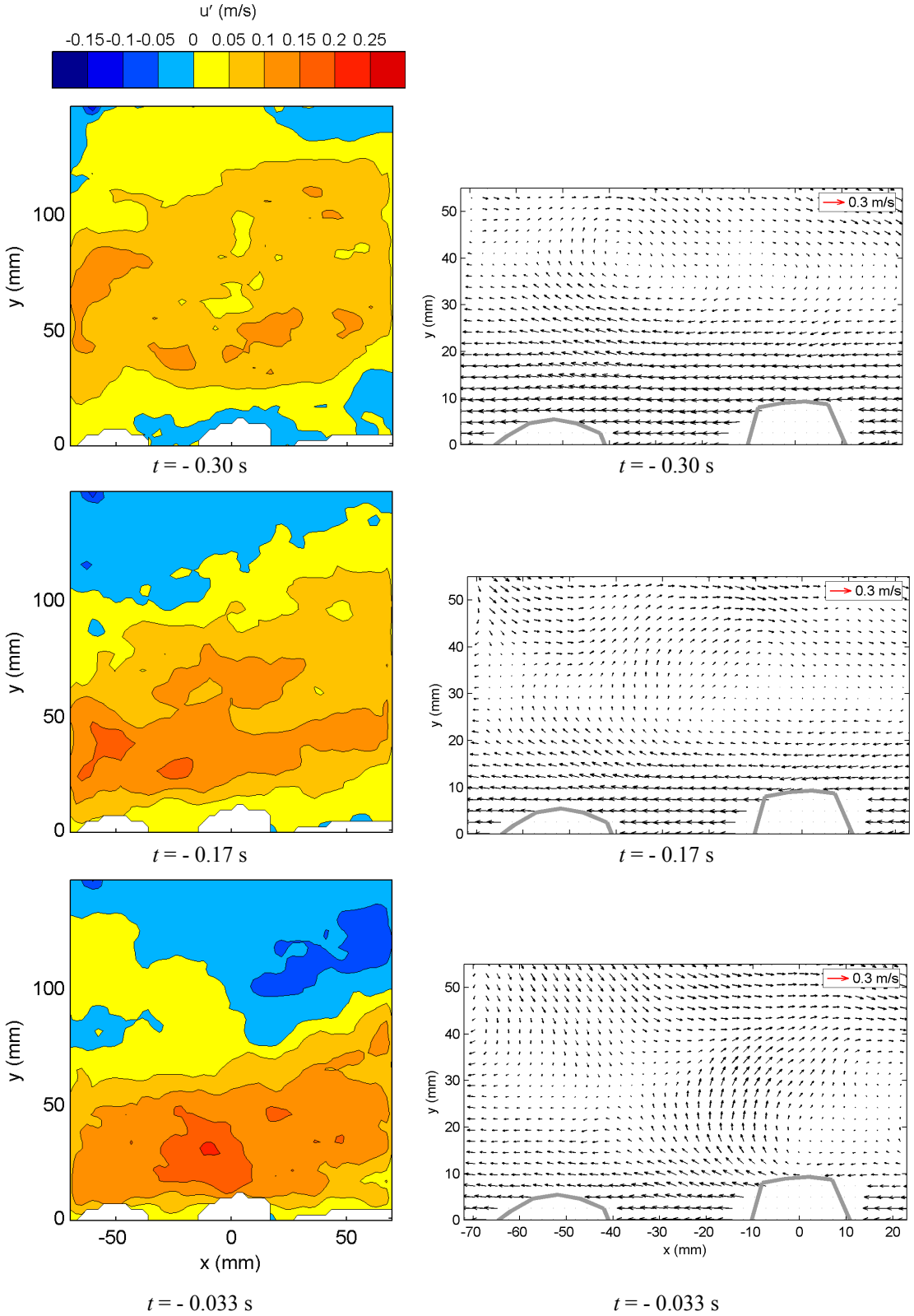

FIGURE K.1 *Sequence of conditionally averaged flow fields of rocking events 5, 3 and 1 frame(s) before the target stone (located at x = 0) started to pivot. Left column: u'-contour plot. Right column: detail of Galilean decomposed ($u = u - 0.3U_0$) vector plots. For clarity only one out of four vectors is shown; a 4 x 4 size filter was used to avoid aliasing.*

Appendix L Instantaneous spliced images of visually selected events (experiment B006)

Event 3

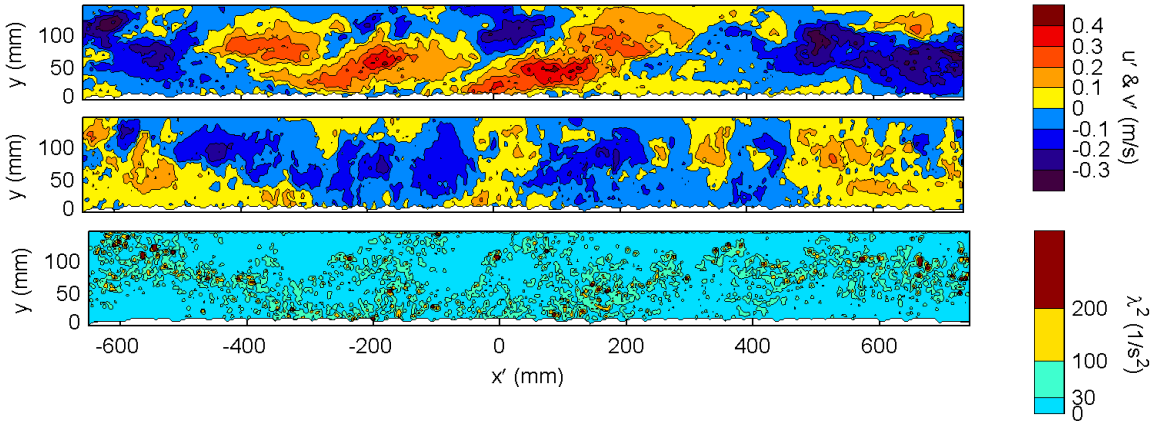

Event 9

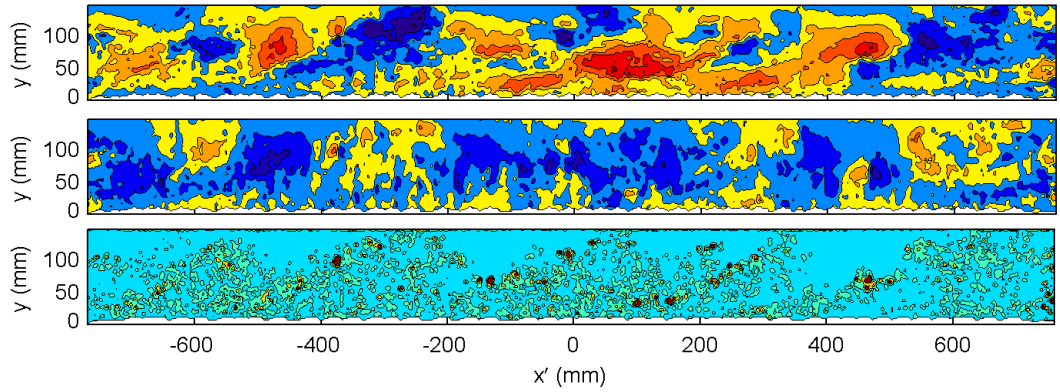

Event 11

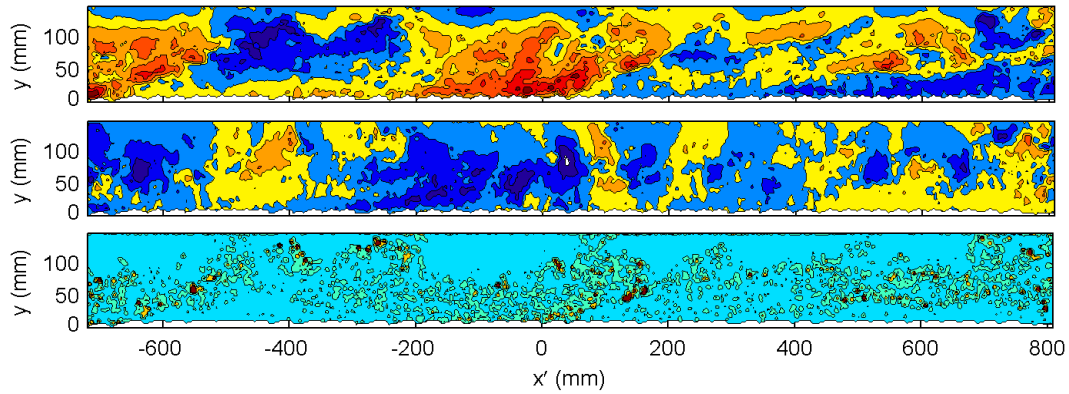

Event 24

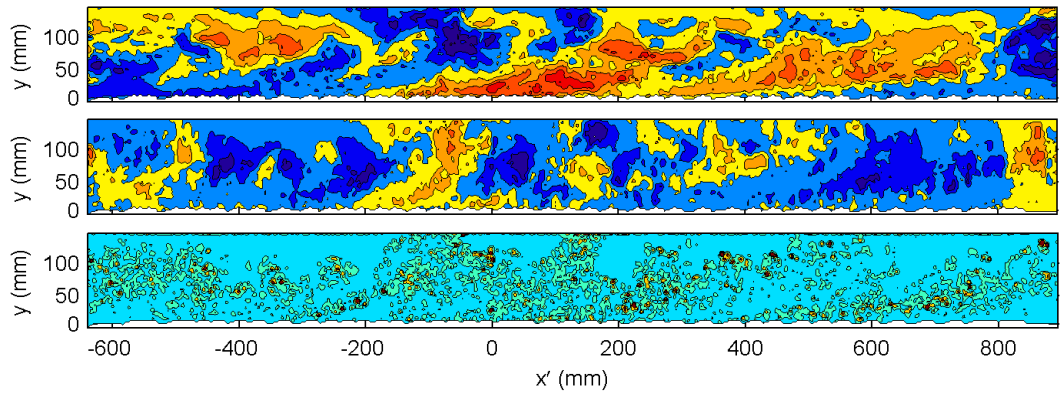

Event 25

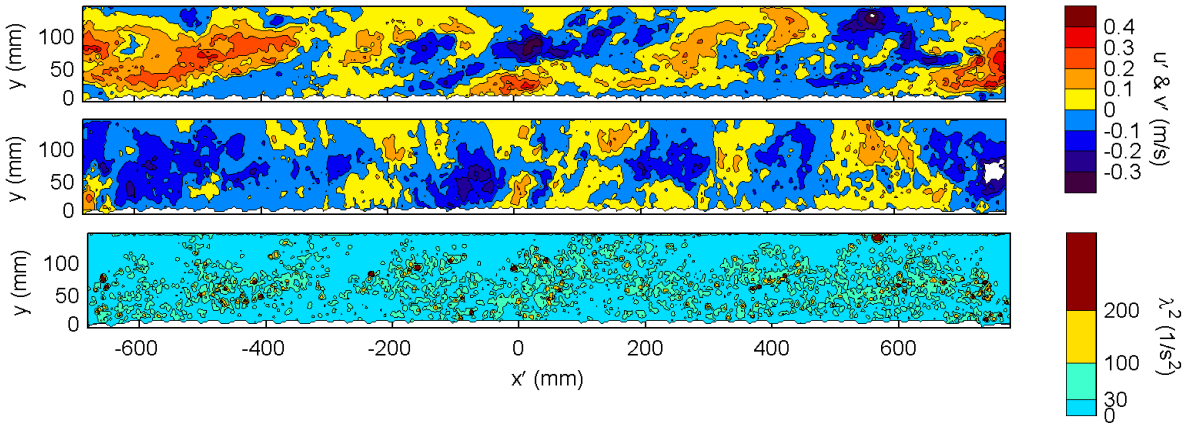

Event 30

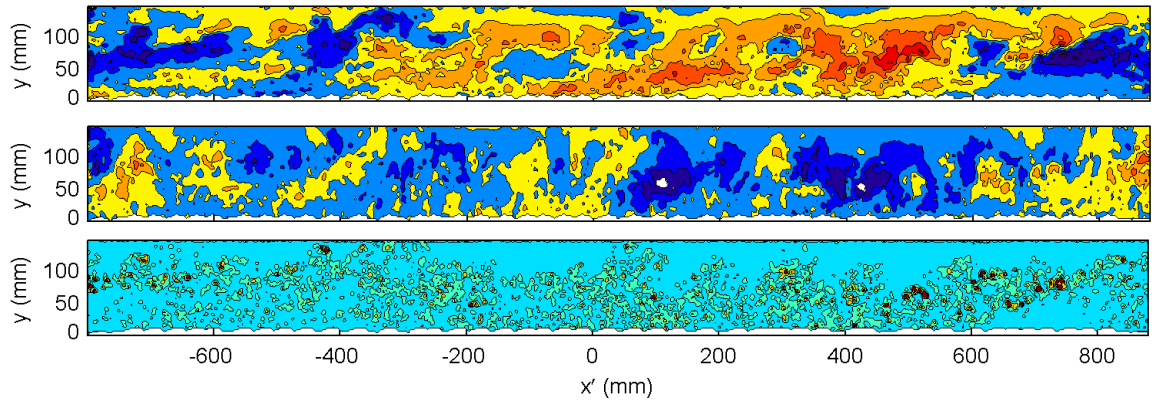

Event 31

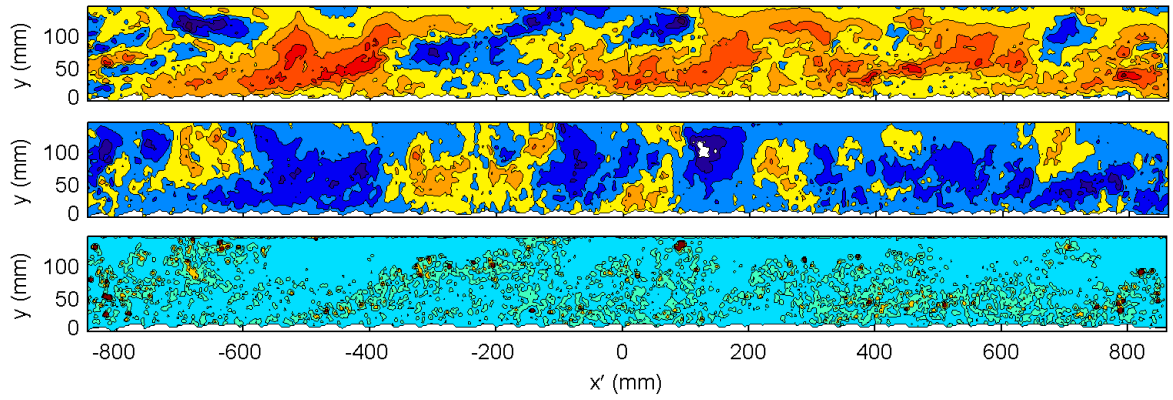

Event 33

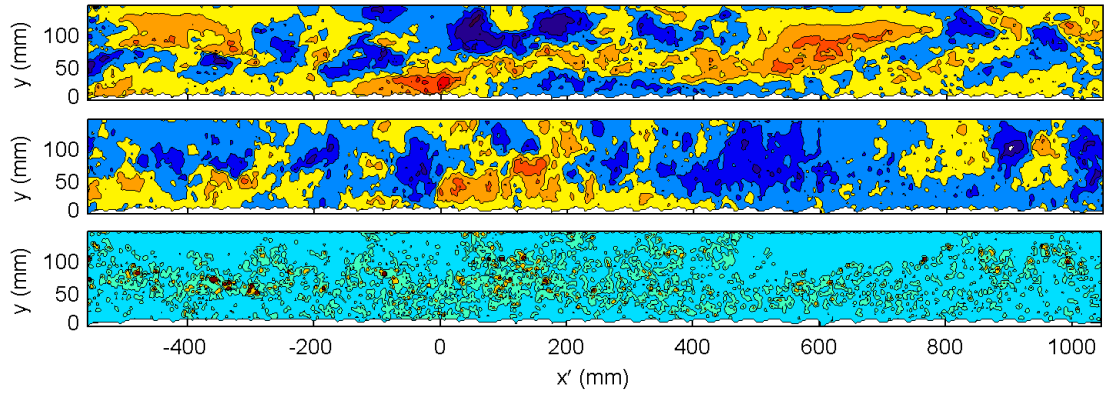

Appendix M Evolution in time of flow around reattachment region (experiment B006)

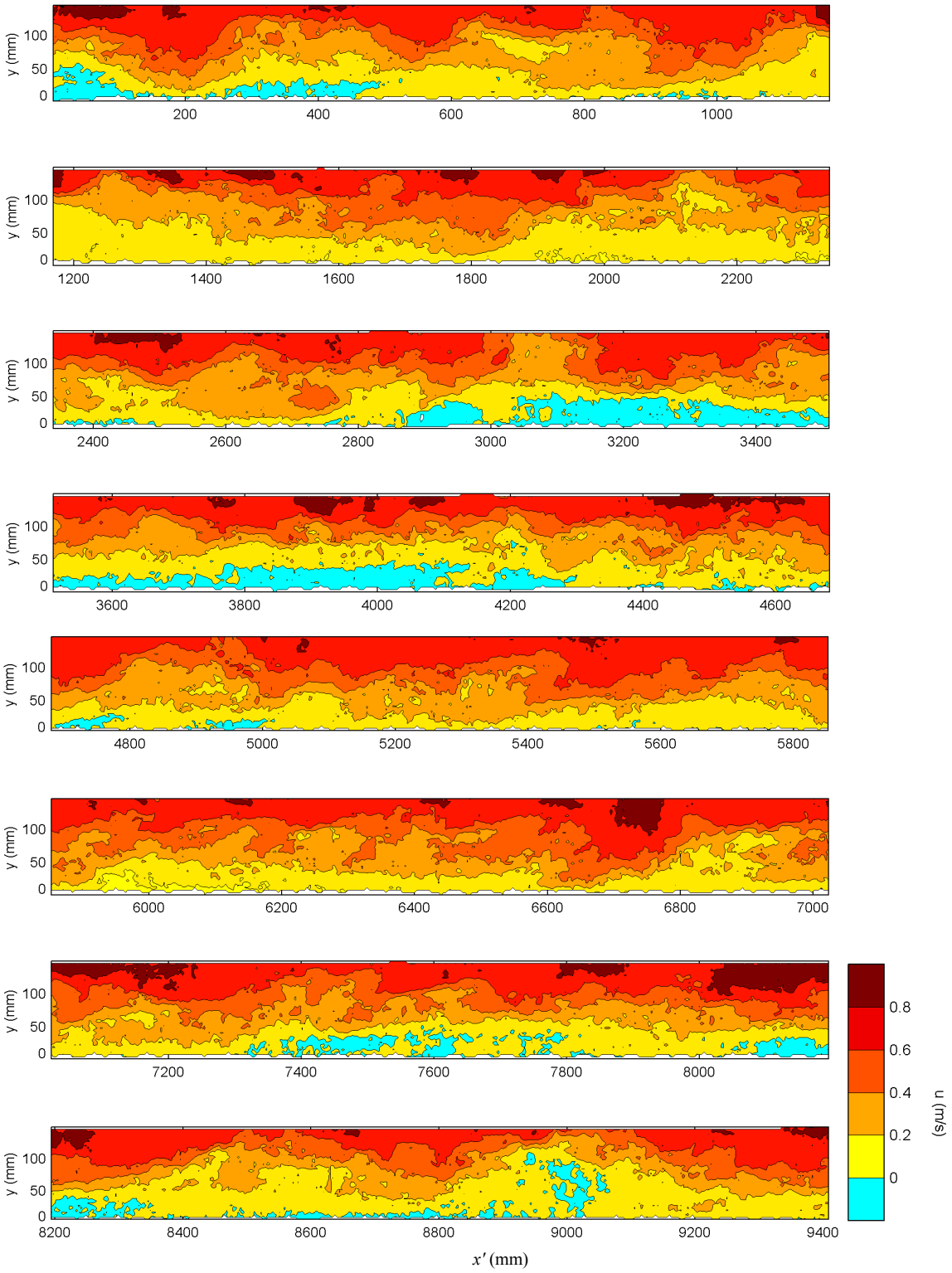

FIGURE M.1 *Spliced image of u-velocity.*

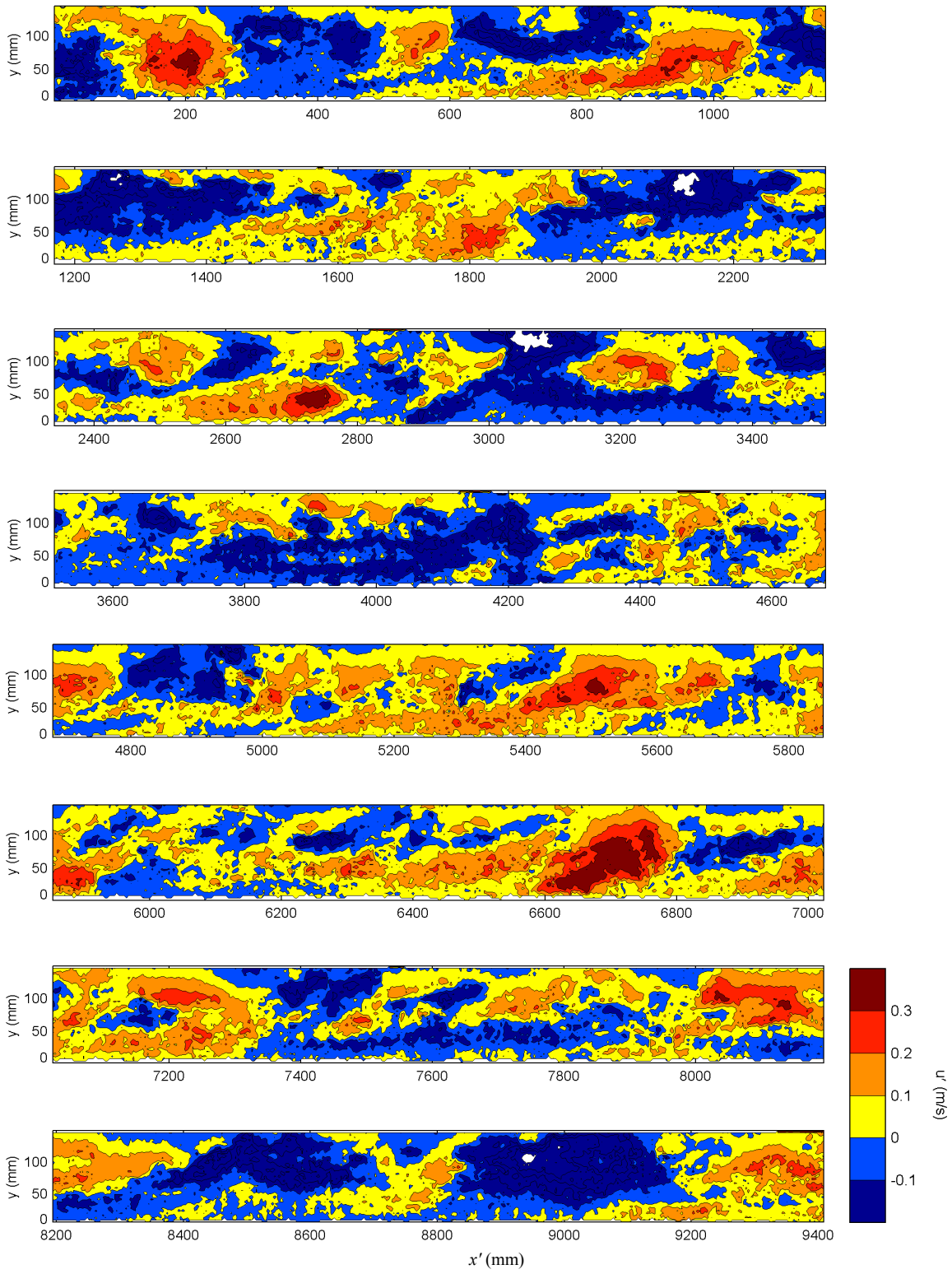

FIGURE M.2 *Spliced image of Reynolds decomposed u-velocity.*

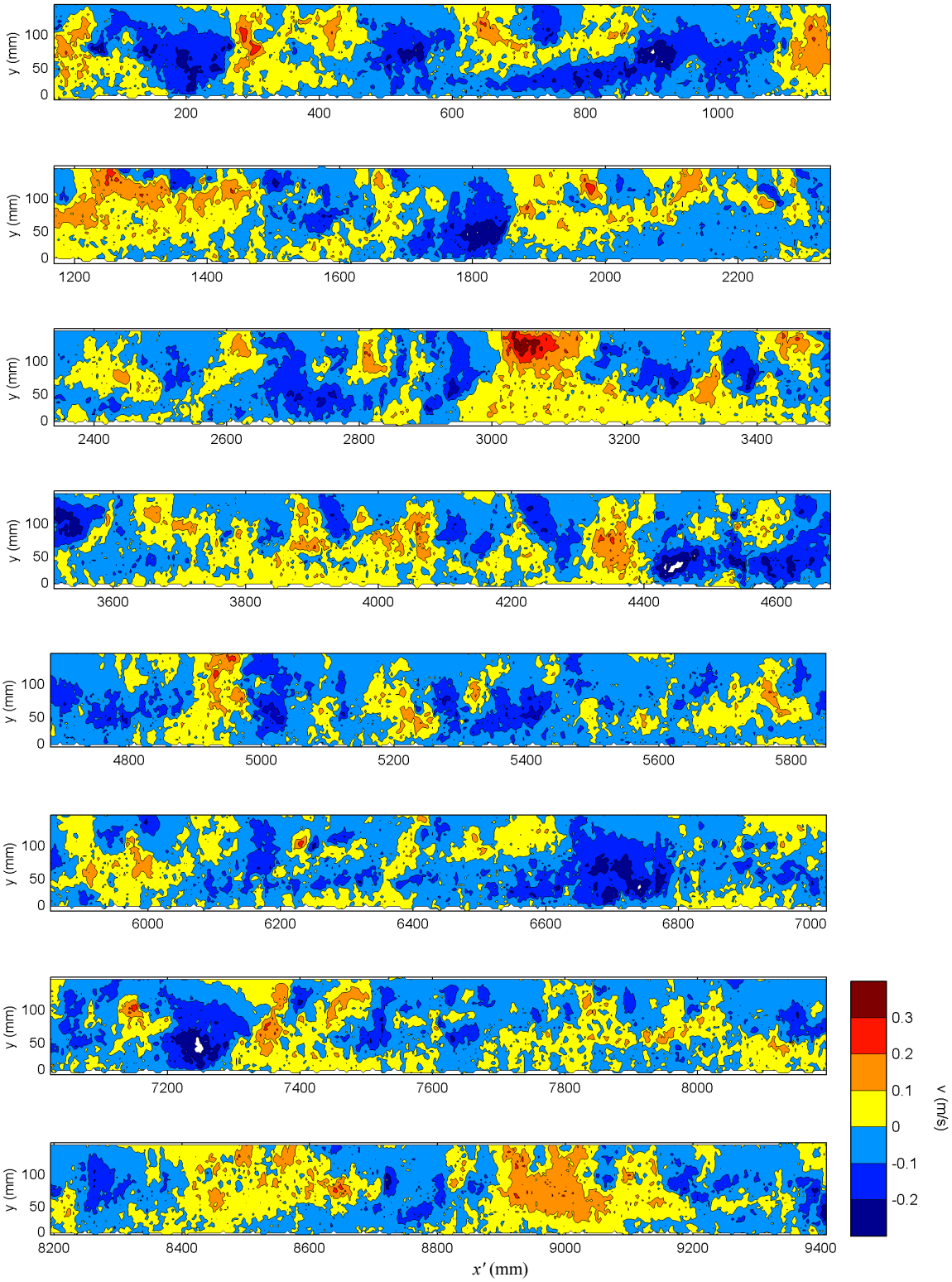

FIGURE M.3 *Spliced image of v-velocity.*